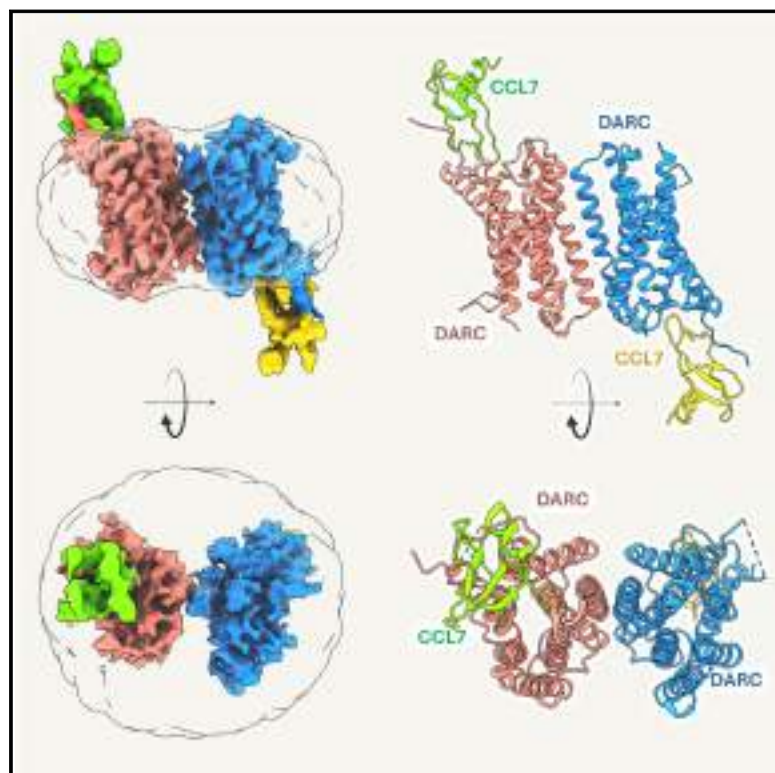


Molecular mechanism of distinct chemokine engagement and functional divergence of the human Duffy antigen receptor

Graphical abstract



Authors

Shirsha Saha, Basavraj Khanppnavar, Jagannath Maharana, ..., Ramanuj Banerjee, Volodymyr M. Korkhov, Arun K. Shukla

Correspondence

ramanujb@iitk.ac.in (R.B.), volodymyr.korkhov@psi.ch (V.M.K.), arshukla@iitk.ac.in (A.K.S.)

In brief

Structural analyses clarify how the Duffy antigen receptor for chemokines (DARC) binds a wider range of ligands and functions differently from prototypical GPCR chemokine receptors.

Highlights

- Duffy antigen receptor for chemokines (DARC) is a promiscuous chemokine receptor
- Cryo-EM structure of DARC reveals a distinct binding mode of chemokine CCL7
- Shortening of TM5/6 compared with GPCRs may drive its unique functional divergence
- Global phosphoproteomics and interactome analysis offer possible functional links

Article

Molecular mechanism of distinct chemokine engagement and functional divergence of the human Duffy antigen receptor

Shirsha Saha,^{1,9} Basavraj Khanppnavar,^{2,3,9} Jagannath Maharana,^{1,9} Heeryung Kim,⁴ Carlo Marion C. Carino,⁵ Carole Daly,⁶ Shane Houston,⁶ Saloni Sharma,¹ Nashrah Zaidi,¹ Annu Dalal,¹ Sudha Mishra,¹ Manisankar Ganguly,¹ Divyanshu Tiwari,¹ Poonam Kumari,⁷ Gagan Deep Jhingan,⁸ Prem N. Yadav,⁷ Bianca Plouffe,⁶ Asuka Inoue,⁵ Ka Young Chung,⁴ Ramanuj Banerjee,^{1,*} Volodymyr M. Korkhov,^{2,3,*} and Arun K. Shukla^{1,10,*}

¹Department of Biological Sciences and Bioengineering, Indian Institute of Technology Kanpur, Kanpur 208016, India

²Laboratory of Biomolecular Research, Paul Scherrer Institute, Villigen, Switzerland

³Institute of Molecular Biology and Biophysics, ETH Zurich, Zurich, Switzerland

⁴School of Pharmacy, Sungkyunkwan University, Suwon 16419, Republic of Korea

⁵Graduate School of Pharmaceutical Sciences, Tohoku University, 6-3, Aoba, Aramaki, Aoba-ku, Sendai, Miyagi 980-8578, Japan

⁶Wellcome-Wolfson Institute for Experimental Medicine, School of Medicine, Dentistry and Biomedical Sciences, Queen's University Belfast, Belfast, UK

⁷Division of Neuroscience and Ageing Biology, CSIR-Central Drug Research Institute, Lucknow, India

⁸Valerian Chem Pvt. Ltd., Vproteomics, New Delhi 110049, India

⁹These authors contributed equally

¹⁰Lead contact

*Correspondence: ramanujb@iitk.ac.in (R.B.), volodymyr.korkhov@psi.ch (V.M.K.), arshukla@iitk.ac.in (A.K.S.)

<https://doi.org/10.1016/j.cell.2024.07.005>

SUMMARY

The Duffy antigen receptor is a seven-transmembrane (7TM) protein expressed primarily at the surface of red blood cells and displays strikingly promiscuous binding to multiple inflammatory and homeostatic chemokines. It serves as the basis of the Duffy blood group system in humans and also acts as the primary attachment site for malarial parasite *Plasmodium vivax* and pore-forming toxins secreted by *Staphylococcus aureus*. Here, we comprehensively profile transducer coupling of this receptor, discover potential non-canonical signaling pathways, and determine the cryoelectron microscopy (cryo-EM) structure in complex with the chemokine CCL7. The structure reveals a distinct binding mode of chemokines, as reflected by relatively superficial binding and a partially formed orthosteric binding pocket. We also observe a dramatic shortening of TM5 and 6 on the intracellular side, which precludes the formation of the docking site for canonical signal transducers, thereby providing a possible explanation for the distinct pharmacological and functional phenotype of this receptor.

INTRODUCTION

The Duffy antigen, originally referred to as Fy glycoprotein, was first identified as a blood antigen expressed on the surface of erythrocytes^{1,2} (Figure 1A), and the polymorphism displayed by this gene was used to classify the Duffy blood group system.² Consequently, it was found to be expressed by additional cell types, such as epithelial cells of lung and kidney,³ endothelial cells of capillaries,⁴ hair cells of cochlea,⁵ airway smooth muscle cells,⁶ and selected regions of brain.^{7–9} Based on a predicted seven-transmembrane (7TM) topology and its ability to recognize multiple chemokines (Figure 1B), it was subsequently referred to as the Duffy antigen receptor for chemokines (DARC) and categorized as a chemokine receptor in the superfamily of G protein-coupled receptors (GPCRs).^{10,11} Strikingly,

however, it does not exhibit productive G protein coupling, as measured using second messenger response with calcium release as a readout, making it an enigmatic 7TM receptor (7TMR).^{9–12}

DARC expressed on the surface of erythrocytes serves as the primary receptor for the malarial parasites *Plasmodium vivax* and *Plasmodium knowlesi*,¹³ and these pathogens latch on to erythrocytes via the interaction of their Duffy binding protein (DBP) with DARC^{14–17} (Figure 1C). Previous studies have demonstrated that DBP-DARC interaction is mediated primarily by the N terminus of DARC, while the transmembrane core appears to be dispensable for the same.^{14–18} Interestingly, a sub-set of population of sub-Saharan descent lack DARC expression on their erythrocytes, and this confers them resistance to *P. vivax* infection.¹⁹ Furthermore, several of the bicomponent pore-forming toxins

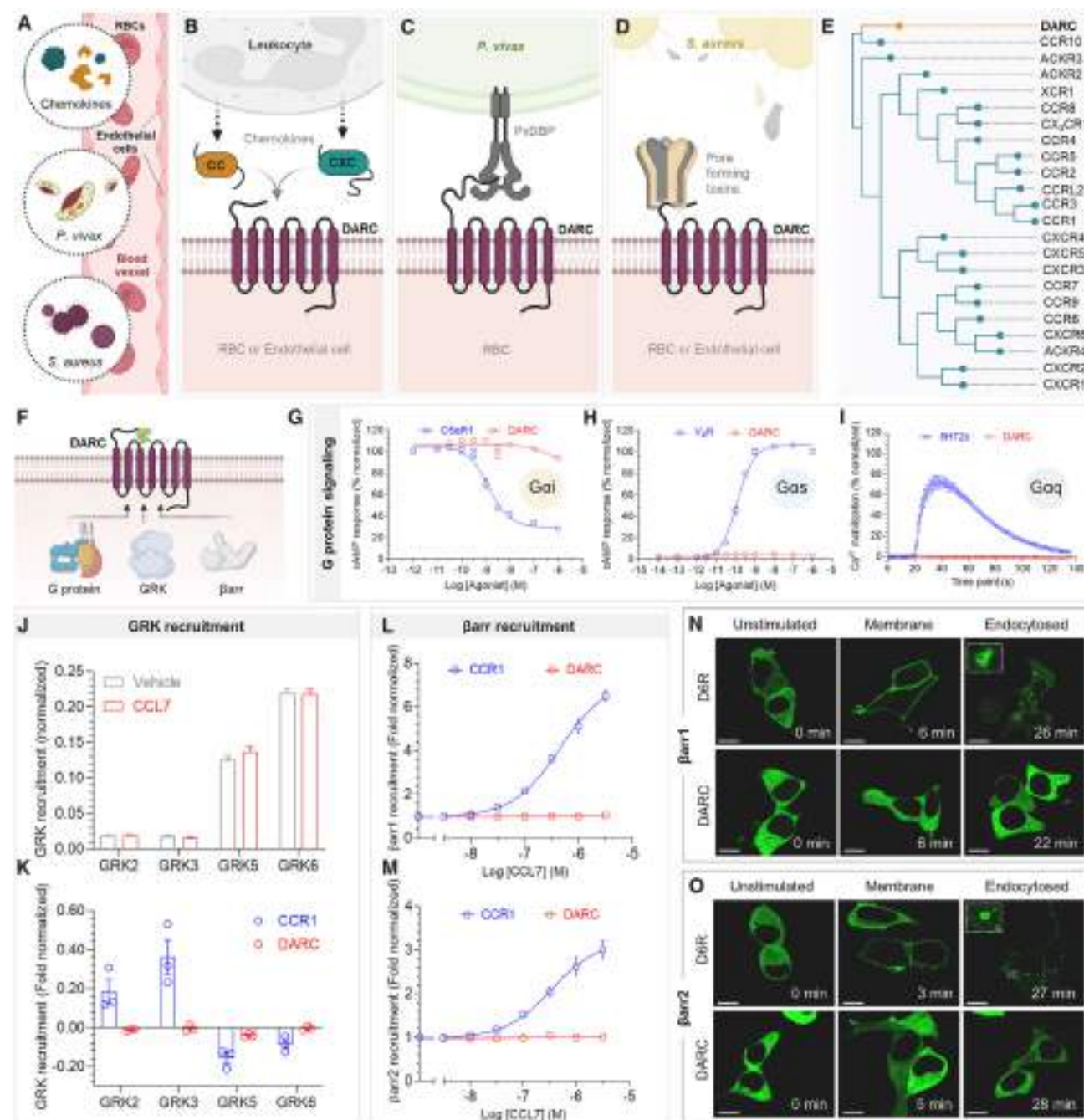


Figure 1. Functional divergence exhibited by the Duffy antigen receptor

(A) DARC provides the docking site for various chemokines and pathogens.

(B) CC and CX chemokines released from leukocytes reportedly bind to DARC.

(C) The malarial parasite *Plasmodium vivax* interacts with and invades red blood cells through the interaction of PvDBP and DARC.

(D) Multiple pore-forming toxins secreted by the pathogen *Staphylococcus aureus* also target DARC receptor for pore formation.

(E) Phylogenetic analysis of all chemokine receptors.

(F) Schematic representation of transducer coupling with DARC.

(G–I) The G protein signaling profiles of DARC with respect to Gi, Gs, and Gq are shown in comparison with C5aR1, V2R, and 5HT2c, respectively. Data (mean ± SEM) represent four (G–I) independent sets. Data have been normalized either with respect to the highest signal observed for each set (treated as 100%) (G) or with respect to the highest signal observed for positive control (treated as 100%) (H).

(J and K) Stimulation of DARC with CCL7 fails to induce GRK recruitment, as measured by BRET assay (J) and NanoBIT assay (K). Data (mean ± SEM) represent 3–6 independent experiments. Change in response has been plotted for both assays.

(legend continued on next page)

(PFTs), such as leukotoxin ED (LukED) and γ -haemolysin AB (HlgAB), secreted by *Staphylococcus aureus* also interact with DARC on erythrocytes, primarily through its N terminus^{20,21} (Figure 1D). This interaction presumably serves as the anchor and nucleation site facilitating the oligomerization of the bicomponent PFTs, leading to subsequent pore formation, cell lysis, and release of hemoglobin. Emerging data now show that PFTs can also lead to cell lysis and tissue damage by targeting DARC expressed on endothelial cells.²² A recent study has suggested that some PFTs may also compete with chemokine binding to DARC and induce structural changes in the receptor upon binding.²³ Moreover, several studies have demonstrated an intriguing link between DARC expression and HIV susceptibility, where the absence of DARC appears to slow down the disease progression, although some studies have also suggested a direct role of DARC in promoting trans-infection of effector cells by HIV-1 virions.^{24–27} These indications make DARC an important therapeutic target from multiple perspectives, including malarial infection, anti-microbial resistance, and HIV infection.

Although chemokine receptors often display ligand promiscuity in terms of recognition and activation by multiple chemokines, DARC represents the most striking example of promiscuous chemokine binding with its ability to recognize both C-C and C-X-C type chemokines, the only 7TMR capable of doing so^{11,28–30} (Figure 1B). It has been proposed that such promiscuous binding to chemokines allows it to scavenge the ligands and establish a chemokine gradient that may have functional implications.³¹ A recent study has also demonstrated that DARC expressed on the surface of developing erythrocytes robustly binds CXCL12, but the same receptor, when present on mature erythrocytes, loses the ability to recognize CXCL12, suggesting a complex regulatory mechanism driving ligand recognition, possibly through post-translational modifications and/or conformational changes.³² In addition, a dimeric form of CXCL12 appears to have stronger binding affinity to DARC compared with the monomeric form.³³ DARC is also characterized as a member of the so-called atypical chemokine receptor sub-group (ACKRs), which lack functional G protein coupling despite exhibiting a conserved 7TM architecture like GPCRs and robust chemokine binding, and is referred to as ACKR1.^{10,34–37} Interestingly, however, while most of the ACKRs such as ACKR2, ACKR3, and ACKR4 exhibit robust β -arrestin (β arr) coupling upon agonist stimulation,^{37,38} the same remains primarily unexplored for DARC. Despite the important contributions of DARC in regulating chemokine homeostasis and pathogenic infections, and a distinct functional manifestation compared with prototypical GPCRs and chemokine receptors, a comprehensive structural and functional characterization of this receptor remains primarily unexplored and represents an important knowledge gap in our current understanding of this receptor.

Against this backdrop, we present a comprehensive profiling of transducer coupling for this receptor using cell-based assays and global phosphoproteomics and interactome analysis to

identify potential non-canonical downstream signaling pathways. We also present the cryoelectron microscopy (cryo-EM) structure of DARC in complex with CCL7, which reveals a distinct mode of chemokine interaction with the receptor compared with prototypical chemokine receptors in terms of effector-site engagement. Importantly, the structure also provides a molecular mechanism resulting from dramatic shortening of TM5 and 6, not observed in any of the previous GPCR structures reported so far, to rationalize the lack of canonical transducer coupling at this receptor while potentially maintaining its ligand-scavenging function. This study elucidates a fundamental mechanism encoding functional divergence in 7TM proteins and provides a framework paving the way for designing better therapeutics.

RESULTS

Functional divergence of the Duffy antigen receptor

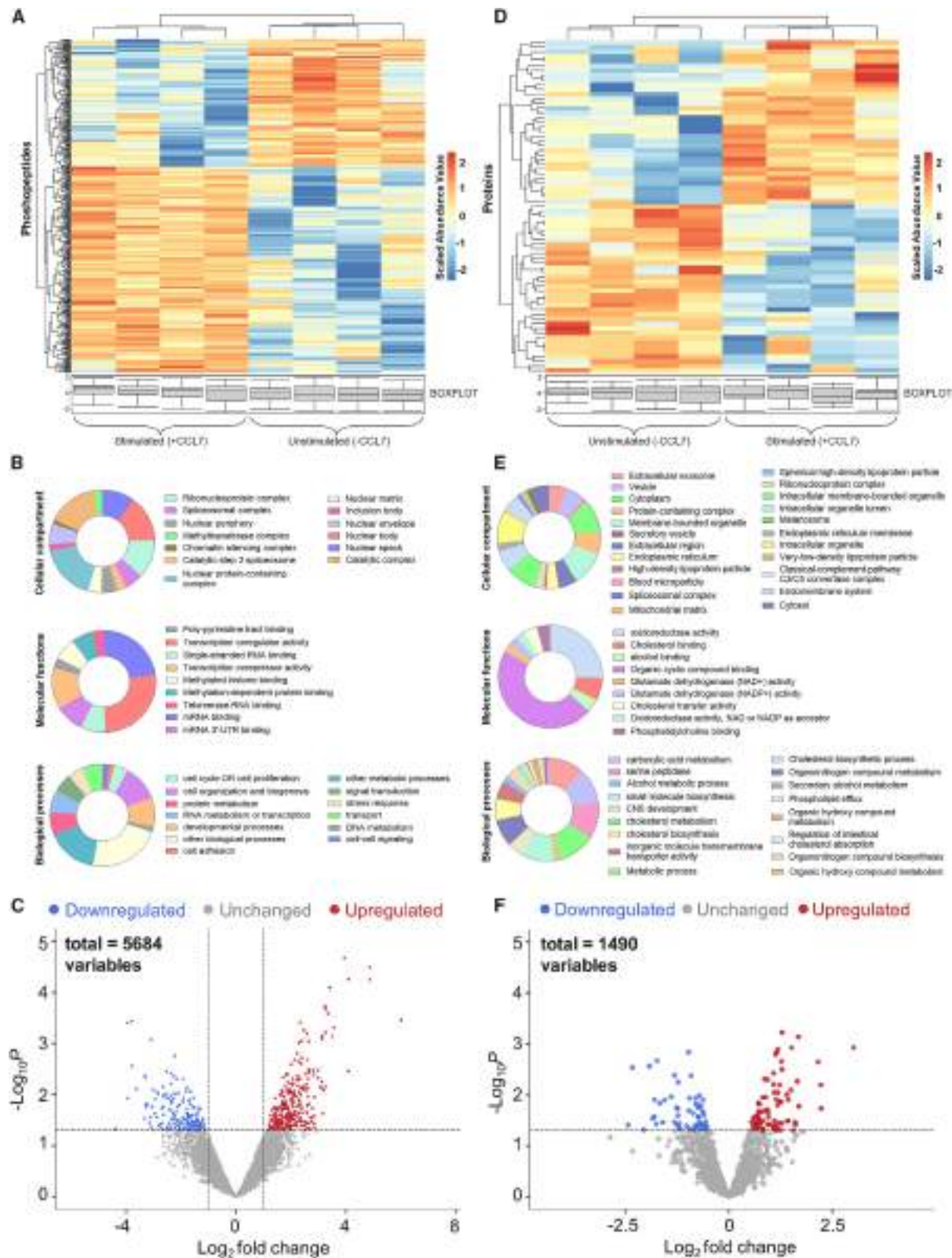
Phylogenetic analysis positions DARC with prototypical chemokine receptor CCR10, with ACKR2 and ACKR3 being the next closest neighbors when compared with chemokine-binding GPCRs (Figure 1E), and GPR182 and GPR82 being the closest neighbors, in addition to ACKR3, when compared with the entire GPCRome (Figure S1). Notably, ACKR2 and ACKR3 are also chemokine receptors; however, they exhibit selective coupling to β arrs without any detectable G protein activation.^{39,40} As mentioned earlier, previous studies on DARC activation and downstream signaling have been limited to the measurement of calcium response as a readout of G protein coupling, and a systematic evaluation of the coupling and activation of canonical GPCR signal transducers, namely the heterotrimeric G proteins, GPCR kinases (GRKs), and β arrs, is still lacking (Figure 1F). Therefore, we first measured second messenger responses downstream of DARC, followed by a comprehensive profiling of all subtypes of G proteins using a NanoBIT-based heterotrimer dissociation assay.⁴¹ We observe that DARC fails to elicit any measurable second messenger response upon stimulation by CCL7 (Figures 1G–1I) and also does not promote the dissociation of any of the G protein subtypes (Figure S2A). In these assays, we used C5aR1, V₂R, and 5HT_{2c} receptors with their corresponding agonists as reference for Gi, Gs, and Gq coupling, respectively, and they exhibited an expected profile.

We next measured CCL7-induced interaction between DARC and all four non-visual GRKs using two different assays based on bioluminescence resonance energy transfer (BRET) and NanoBIT methodologies. In the BRET assay, using *Renilla* luciferase fusion at the carboxyl terminus of DARC and GFP10 fusion at the N terminus of GRKs, we did not observe any detectable interaction of DARC with any of the GRKs upon stimulation with CCL7, and the signal remained similar to the vehicle control (Figures 1J and S2B). The basal BRET signal for GRK5/6 was higher compared with GRK2/3, as expected based on their

(L and M) Recruitment of β arr isoforms (β arr1/2) to DARC and CCR1 are shown, as assessed via NanoBIT assay. Data (mean \pm SEM) represent three independent experiments and have been normalized with respect to the signal observed at basal condition for each set (treated as 1).

(N and O) Confocal assay corroborates the lack of β -arrestin recruitment and trafficking downstream of DARC. A representative image visualizing mYFP- β -arrestin is shown from two independent experiments (scale bars, 10 μ m).

See also Figures S1–S4.



(legend on next page)

membrane localization. Similarly, in the NanoBIT assay, CCL7 stimulation of cells expressing DARC-SmBIT and GRK-LgBIT constructs did not result in any measurable luminescence signal (Figures 1K and S2C). In this experiment, we used a prototypical chemokine receptor, namely CCR1, as a reference, which exhibited interaction with all four GRKs, albeit at different levels, with a comparatively stronger signal for GRK2/3 over GRK5/6 (Figures 1K and S2C). We observed a decrease in luminescence signal for CCR1 in the case of GRK5/6, as expected due to CCL7-induced receptor internalization and thus a decrease in proximity of the receptor and GRKs (Figures 1K and S2C).

Finally, we measured CCL7-induced β arr recruitment to DARC using four different assays, namely NanoBIT, co-immunoprecipitation (coIP), confocal microscopy, and TANGO assay. In the NanoBIT assay using DARC-SmBIT and LgBIT- β arr1/2 constructs, there was no luminescence signal for DARC upon CCL7 stimulation, while CCR1 exhibited robust, dose-dependent β arr1/2 recruitment (Figures 1L and 1M). Similarly, in the confocal microscopy assay using HEK293 cells transfected with DARC and β arr1/2-mYFP, we did not observe any detectable translocation of β arrs upon CCL7 stimulation, while D6R, used as a reference, exhibited CCL7-induced membrane translocation of β arrs at early time points (3–6 min) followed by their localization in endosomal vesicles upon prolonged exposure (22–28 min) (Figures 1N and 1O). This is further corroborated using a coIP assay, where CCL7 stimulation failed to promote any measurable interaction of DARC with β arrs, while for D6R, we observed robust interaction of β arrs (Figures S3A and S3B). As some 7TMRs have a weaker propensity to interact with β arrs, resulting in a transient binding, we generated a series of chimeric constructs of DARC harboring the carboxyl terminus of the vasopressin receptor (V_2R), referred to as DARC- V_2R . The notion behind generating these chimeric constructs is to enhance β arr binding affinity to DARC, as previously reported for several class A GPCRs.^{42,43} Still, however, there was no measurable interaction of β arrs with any of the DARC- V_2R constructs in the coIP assay in response to CCL7 stimulation (Figures S3C–S3F). Finally, we generated a TANGO assay construct for DARC using the reporter gene strategy, which is one of the most sensitive methods to probe β arr binding to 7TMRs.⁴⁴ However, even in this assay, CCL7 stimulation did not elicit any β arr recruitment, while CCR2, used as a reference, displayed a dose-dependent response (Figure S3G). We also measured the surface expression of the receptor in each of these functional assays compared with mock-transfected cells and present these data in Figure S4A.

Considering the ligand promiscuity of DARC, we also measured cyclic AMP (cAMP) response and β arr recruitment following stimulation of the receptor by several C-C and C-X-C chemokines. However, similar to CCL7, we did not observe any detectable response for any of these chemokines, either in terms of cAMP inhibition or β arr recruitment (Figures S4B–S4D). Taken together, this analysis demonstrates the lack of canonical transducer coupling to DARC, unlike prototypical or atypical chemokine receptors, and, therefore, establishes it as a functionally divergent, chemokine-binding 7TMR.

Potential interaction partners and signaling pathways downstream of DARC

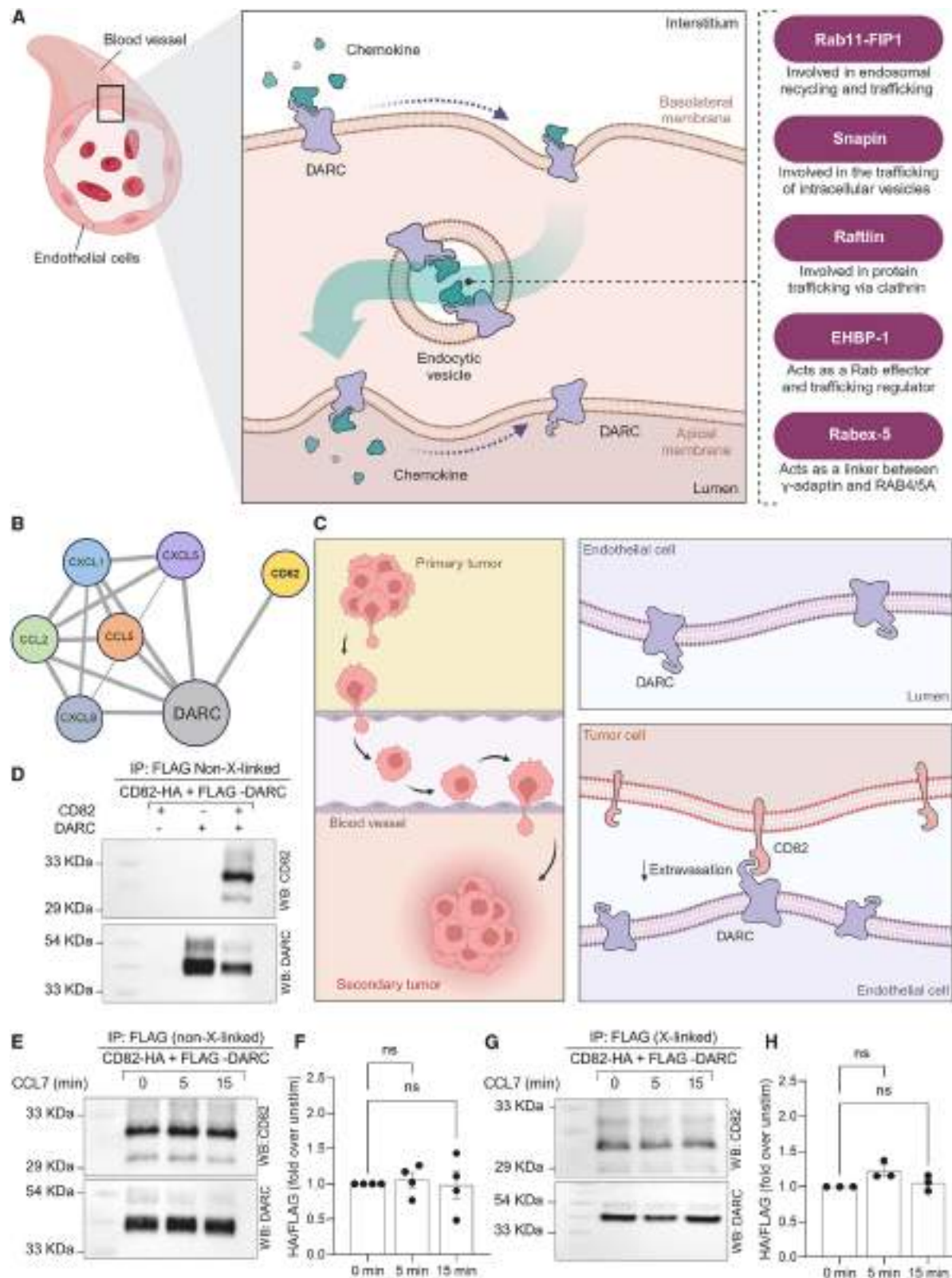
Although canonical downstream signaling is not likely in erythrocytes, considering their anucleated nature, as mentioned earlier, DARC is also expressed in endothelial cells, and, therefore, it is plausible that it signals through non-canonical signaling pathways. In order to test this hypothesis, we carried out an unbiased, global phosphoproteomics screen using a mass spectrometry (MS) approach, using HEK293 cells stably expressing DARC. We reasoned that such an analysis should uncover the spectrum of cellular proteins undergoing phosphorylation and dephosphorylation and, therefore, should provide possible leads into non-canonical signaling downstream of this receptor. We also note that CCL7 binds to four different chemokine receptors, namely CCR1, 2, 3, and 5, other than DARC.⁴⁵ However, none of these CCL7-binding chemokine receptors are expressed endogenously at detectable levels in HEK293 cells, as reported in a previous study.⁴⁶ Therefore, we reasoned that our phosphoproteomics data on HEK293 cells stably expressing DARC should report CCL7-induced, DARC-mediated phosphorylation and dephosphorylation events.

We prepared samples under unstimulated and CCL7-stimulated conditions, generated proteolytic fragments by trypsin digestion, enriched for phosphorylated peptides using TiO_2 beads, and then identified the phosphorylated peptides using liquid chromatography-tandem MS (LC-MS/MS). A schematic of the phosphoproteomics experiment is presented in Figure S5A, and the complete details of the data are presented in Table S1, including the peptides and proteins that are identified, the relative change in their phosphorylation status, and other technical parameters. Interestingly, we identified approximately 8,215 phosphopeptides, corresponding to more than 2,600 different proteins, and a statistical analysis using paired t test between the basal (unstimulated) and CCL7-stimulated conditions, narrowed down the list to approximately 300 different proteins

Figure 2. Proteomics-based insights into potential downstream signaling

- Heatmap showing differentially phosphorylated peptides generated following MS-based phospho-proteomics analysis of HEK293 cells stably expressing DARC in the presence and absence of CCL7 stimulation. Four independent samples prepared in parallel were subjected to analysis.
- Cellular proteins identified to undergo phosphorylation/dephosphorylation following stimulation with CCL7 were classified on the basis of biological processes, molecular functions, and cellular localizations to reveal an extensive network of potential signaling pathways.
- Volcano plot representation of the peptides undergoing upregulation/downregulation in their phosphorylation state following stimulation with CCL7.
- Heatmap showing proteins whose physical interaction with DARC undergoes an alteration upon stimulation with CCL7, identified on the basis of mass-spectrometry-based interactome study. Four independent samples prepared in parallel were subjected to analysis.
- Cellular proteins identified to undergo an alteration in their physical interaction with DARC following stimulation with CCL7 were classified on the basis of biological processes, molecular functions, and cellular localizations to reveal an extensive network of potential signaling pathways.
- Volcano plot representation of the proteins undergoing increased/decreased association with DARC upon stimulation with CCL7.

See also Figures S5 and S6 and Tables S1 and S2.



(legend on next page)

that exhibited a change in their phosphorylation status (Figures 2A–2C). In order to gain further insights into possible signaling mechanisms, we classified the identified proteins based on their localization in cellular context, involvement in different biological processes, and their assigned molecular functions. Interestingly, these proteins fall under various functional categories, including signal transduction, cellular proliferation, and cellular organization, and, therefore, suggest potentially broad implications for the activation of DARC in cellular and functional contexts (Figures 2B and S5B).

One of the key functions attributed to DARC is transcytosis of chemokines in endothelial cells, where it binds to chemokines on the basolateral side and subsequently mediates their transcytosis to the apical side⁴⁷ (Figure 3A). This process contributes not only to generating a chemokine gradient but also, through the chemokines exposed on the lumen, to facilitating the binding of circulating leukocytes, their subsequent extravasation, and trans-endothelial migration.⁴⁸ In agreement with this, our phosphoproteomics analysis has identified several proteins that are typically involved in the process of cellular endocytosis pathways (Figure 3A) and, therefore, further corroborate the functional capabilities of DARC in the context of chemokine transcytosis.

Considering that DARC does not couple to the canonical GPCR partners such as G proteins, GRKs, and β arrestins, we carried out a global interactome analysis upon stimulation of DARC-expressing HEK-293 cells with CCL7. We first performed a colP step under cross-linking conditions to enrich DARC-interacting proteins, followed by their detection using mass-spectrometry (Figure S6A). In these experiments, as a reference, we also used unstimulated cells, which were lysed and immunoprecipitated in parallel to subtract non-specific proteins. We carried out these experiments as four biological replicates and our analysis identified a total of around 1,700 different proteins (Table S2). Statistical analysis using Student's paired t test between the basal (unstimulated) and CCL7-stimulated conditions revealed that 73 proteins undergo a significant alteration, either upregulation or downregulation, in their interaction with DARC (Figures 2D and 2F). Gene-ontology-based enrichment and pathway enrichment revealed that the proteins identified are involved in regulating a multitude of different cellular processes and exhibit varied cellular localization (Figures 2E and S6B). Additionally, comparison of our interactome data with the proteins identified using MS-based global phosphoproteomics revealed 66 common proteins. Network analysis of these common

proteins identifies a range of various cellular processes downstream of DARC and provides a promising direction for future studies to fully explore and establish the functional capabilities of this intriguing chemokine receptor. A complete detail of all the relevant data is provided in Table S2.

In parallel, we also carried out STRING analysis using DARC as the search keyword and identified a tetraspanin CD82 as a potential interaction partner (Figure 3B). CD82 is a four-transmembrane glycoprotein that is implicated in metastasis suppression in multiple cancer types, and it is proposed that possible cross-talk of CD82 with DARC expressed on vascular endothelial cells prevents the extravasation of tumor cells present in circulation^{49–51} (Figure 3C). In addition, interaction of DARC expressed on endothelial cells, with CD82 present on tumor cells that have intravasated into the circulation, has been suggested to trigger senescence in the latter via a p21/Waf1-mediated signaling pathway.⁵¹ Moreover, crosstalk of DARC with CD82 has also been proposed to enhance p21 expression in the long-term hematopoietic stem cells of the bone marrow and help maintain their quiescence.⁵² Therefore, we next validated the interaction of DARC with CD82 in transfected HEK293 cells under basal and CCL7-stimulation conditions. As presented in Figures 3D–3H, we observed a robust interaction of DARC-CD82 that remains primarily unaltered upon agonist stimulation. Although future studies are warranted to explore the functional consequences of DARC-CD82 crosstalk, our data provide a plausible functional link involving DARC.

Overall structure of CCL7-DARC

In order to uncover the molecular mechanism directing this functional divergence of DARC, we set out to determine its structure in complex with a chemokine ligand using cryo-EM. We expressed and purified full-length, wild-type DARC in the presence of a C-C type chemokine, CCL7, and a nanobody (Nb52) targeted against the N terminus of DARC.⁵³ The purified receptor exhibited two distinct populations on size-exclusion chromatography, which presumably represent monomeric and dimeric states of the ligand-receptor complexes (Data S1). Considering the small size of the CCL7-DARC complex, we subjected the dimeric population to cryo-EM and observed an overall monodisperse population, with two-dimensional (2D) class averages showing a non-physiological arrangement of the ligand-receptor complexes (Data S1). Subsequently, we determined the structure of CCL7-DARC at an estimated resolution of 3.65Å, with clearly discernible densities for the receptor and ligand

Figure 3. Identifying potential signaling partners of DARC

(A) A simplified schematic depicting the process of transcytosis of DARC along with the bound chemokine across the venular endothelium, from the basolateral to the apical side. Hits identified from phosphoproteomics analysis that are potential regulators of this pathway have been denoted, along with a brief description of their known functions (Rab11-FIP1, Rab11 family interacting protein 1, Uniprot ID: Q6WKZ4; Snapin Uniprot ID: O95295; Raftlin Uniprot ID: Q14699; EHBP-1, EH-domain-binding protein 1, Uniprot ID: Q8NDI1; Rabex-5 Uniprot ID: Q9UJ41).
(B) STRING analysis reveals CD82 as one of the potential interactors of DARC.
(C) Schematic representation of the physiological role of CD82 and DARC interaction in suppressing metastasis.
(D) DARC interacts with CD82 in the absence of any stimulation, as measured under non-cross-linking conditions. A representative image from three independent experiments is shown here.
(E–H) Stimulation with CCL7 does not alter the interaction between DARC and CD82, as measured under both non-cross-linking (E and F) and cross-linking (G and H) conditions. A representative image from three to four independent experiments, along with densitometry-based quantification of data (mean \pm SEM) normalized with respect to the signal observed under unstimulated condition (treated as 1) is shown here. Two-way ANOVA using Tukey's multiple comparison has been performed (ns denotes not significant).

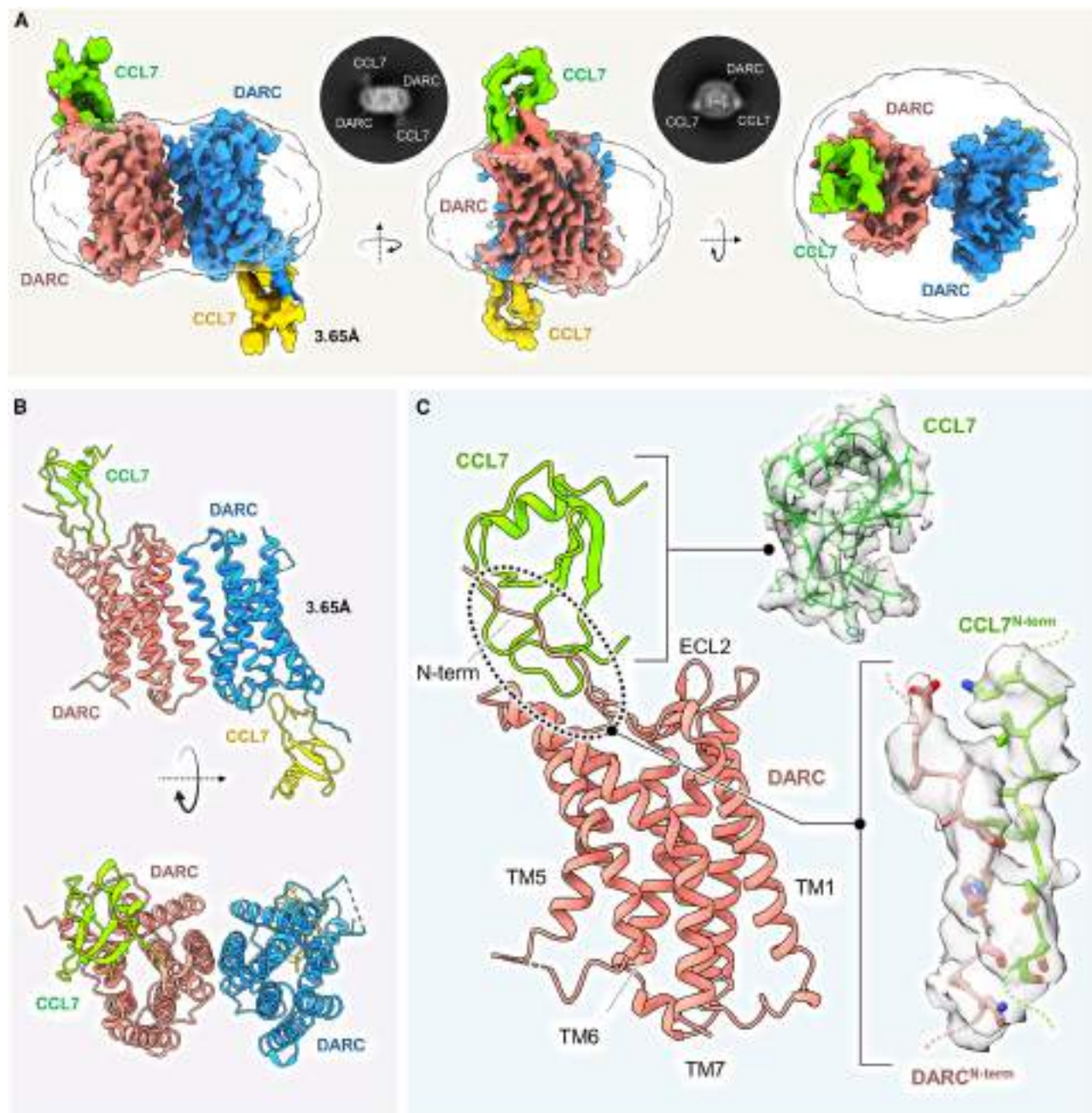


Figure 4. Structure of the Duffy antigen receptor

(A) Cryo-EM structure of the CCL7-bound DARC dimeric complex, at a resolution of 3.65 Å, is shown in surface depiction in three different orientations. Representative 2D class averages with discernible secondary features are shown in the inset.

(B) Atomic coordinates of CCL7-DARC complex shown in ribbon representation in two different views.

(C) A monomeric unit of CCL7-DARC complex is shown as a cartoon representation with cryo-EM density maps of CCL7 and the interface region between CCL7 and DARC in the insets. (Salmon and blue, DARC protomers; green and yellow, CCL7).

See also [Data S1](#) and [Tables S3](#) and [S4](#).

([Figures 4A–4C](#); [Data S1](#); [Table S3](#)). However, we did not obtain any densities for Nb52. Although we refined the structure using C2 symmetry, we also performed a symmetry expansion of the final particle stack, followed by a local refinement in C1 with a mask covering the whole complex. However, the map refine-

ment exhibited a slightly lower resolution with symmetry expansion and did not exhibit a dramatic difference when compared with symmetrically refined reconstruction ([Data S1](#)). The cross-correlation of the structures was 0.915, suggesting that the CCL7-DARC dimer indeed has a 2-fold symmetry.

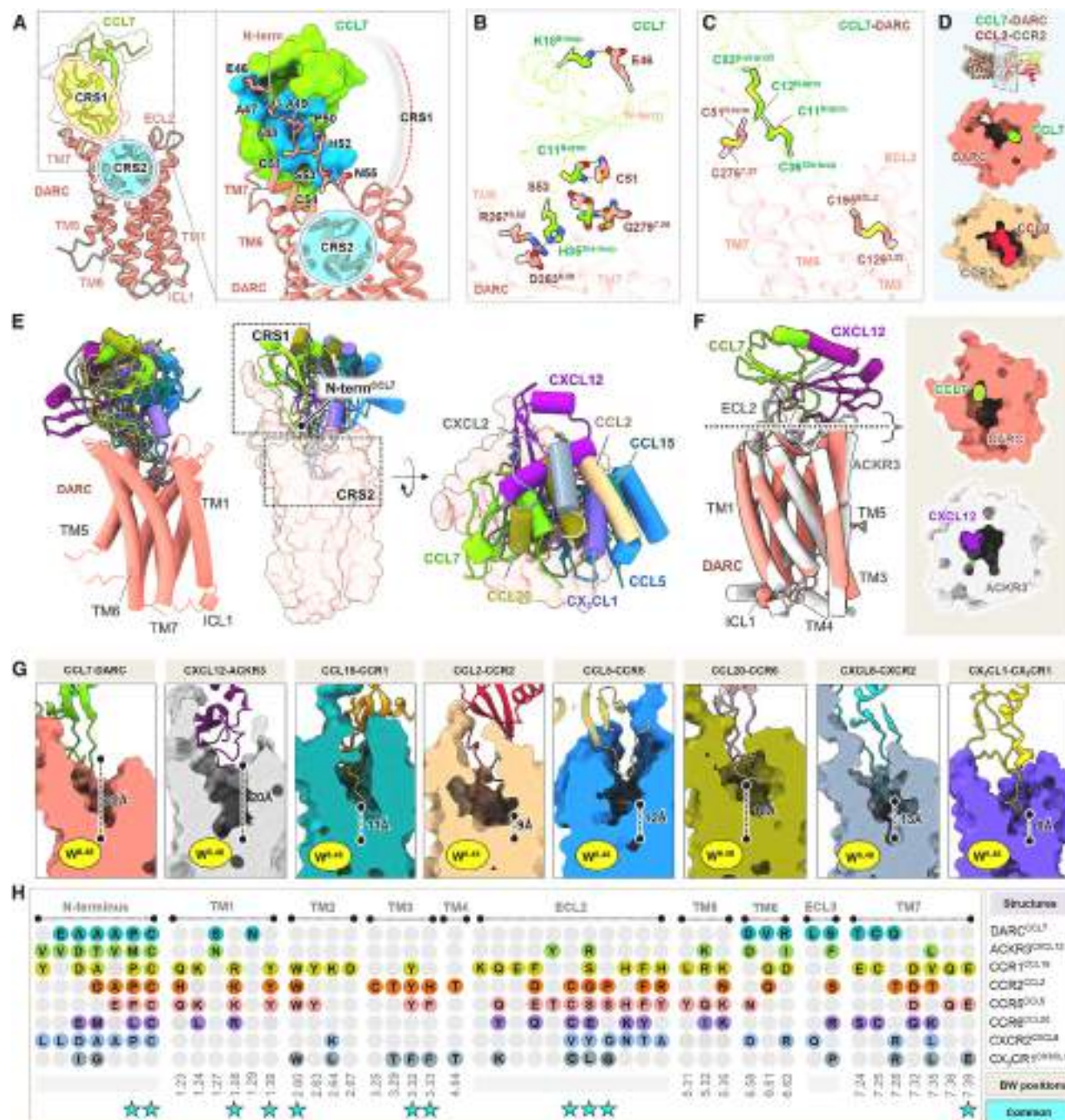


Figure 5. A distinct mode of chemokine recognition by DARC

(A) Overall CCL7 binding mode in DARC. The regions of CRS1 and CRS2 are indicated by dashed circles (left). The key residues of DARC that interacts with CCL7 (blue surface) are shown. The possible CRS2 is empty and indicated by blue dashed circle.

(B) Interactions between the core domain of CCL7 and the N terminus of DARC in CRS1 are illustrated (hydrogen bonds and salt bridges are shown as black dashed lines).

(C) Disulfide linkages in CCL7 and DARC stabilize their overall architecture and fold.

(D) The shallow binding of CCL7 with DARC has been depicted as surface slice representation. The CCL2-CCR2 structure (PDB: 7XA3) has been used as a reference where CCL2 enters deep into the ligand binding pocket.

(E) Overall binding pose of chemokines on DARC (left and right) with CRS1 and CRS2 highlighted as dotted box (middle). Other receptor components have been removed after aligning the chemokine-receptor complex structures with CCL7-DARC.

(F) Structural alignment of CCL7-DARC and CXCL12-ACKR3 (left), the shallow binding mode of ligands on the respective ligands are illustrated as surface slice representation.

(legend continued on next page)

Before proceeding with structural inference, we also carried out additional biochemical analysis to confirm the binding of CCL7 to purified DARC (Data S1). In these experiments, we first purified DARC under apo-condition, followed by incubation with either CCL7 and Nb52 individually or together and subsequently analyzed these complexes by size-exclusion chromatography. We observed that even though apo-DARC tends to dimerize, both CCL7 and Nb52 can stably interact with DARC, and that, upon co-incubation, they also appear to bind concomitantly (Data S1). In order to further corroborate that the extra-micellar density observed in our structure indeed belongs to CCL7, we subjected the apo-DARC and CCL7-DARC complexes (without Nb52) to cryo-EM analysis and confirmed a clear density of CCL7 present in the CCL7-DARC complex but not in the apo-DARC sample (Figures S7A and S7B). In addition, we also performed manual docking of Nb52 and CCL7 individually into the EM map and calculated the model-map correlation coefficients for each of the docking poses. As presented in Data S1, the best correlation coefficient is observed for one of the CCL7 poses, which we subsequently used for structural refinement and interpretation.

A distinct mode of ligand binding in DARC

We observe that CCL7 makes extensive contacts with the N terminus of the receptor, with some contribution from the extracellular side of TM6, TM7, and 3rd extracellular loop (ECL3) (Figures 5A–5C; Table S4). The N-terminal residues from Glu46 to Asn55 of DARC are positioned in a groove formed by CCL7, and this interaction is stabilized by several hydrogen bonds and other non-bonded contacts (Figures 5A and 5B; Table S4). Specifically, the N-terminal residues of DARC from Glu46 to Leu57 form an extended loop, which orients itself onto a docking site on CCL7 formed by the N-terminal loop residues Ser⁸ to Lys¹⁸ and the β -strand3 residues Lys⁴⁹ to Ala⁵³. It is also interesting to note that the disulfide bridge in DARC between Cys51 in the N terminus and Cys276^{7,25} in TM7 is packed against a disulfide bridge formed between Cys¹² and Cys⁵² of CCL7, and this helps the N terminus of DARC align in the CCL7 groove (Figure 5C). Chemokine receptors typically engage chemokines through two binding sites known as chemokine recognition site, 1 and 2 (CRS1 and 2).⁵⁴ However, CCL7 interaction with DARC appears to engage only CRS1, without any significant interaction with CRS2 (Figure 5A). This is evident upon comparing the CCL7-DARC interface with a previously determined CCL2-CCR2 complex⁵⁵ through a cross-sectional area, where the binding pocket corresponding to CRS2 is empty (Figure 5D). This is further apparent upon comparison with other chemokine-chemokine receptor complexes in G protein-bound, active conformation^{55–61} (Figure 5E). Interestingly, the lack of CRS2

binding site observed here is reminiscent of CXCL12 binding pose in ACKR3⁶¹ (Figure 5F). Moreover, the overall binding pocket in CCL7-DARC appears to be constricted compared with CCR2 (Figure S7C). A direct comparison of CCL7 positioning on DARC, with all previously determined structures of chemokine-chemokine receptor complexes^{55–61} in active conformation, further highlights the absence of CRS2 engagement in CCL7-DARC. As indicated in Figure 5G, the N terminus of CCL7 does not extend as deep into the orthosteric binding pocket as observed for other chemokines in complex with their cognate chemokine receptors. CCL7 displays maximal distance from the conserved tryptophan residue in TM6 (Trp^{6,48}), bearing a close resemblance to CXCL12 interaction with ACKR3 (CXCR7) (Figure 5G). In addition to CRS1, the 30s loop of CCL7 also forms a critical interaction interface by engaging the extracellular end of TM6 of the receptor (Figure 5B).

We also compared the ligand-receptor contacts observed in CCL7-DARC with those in other chemokine-chemokine receptor complexes, and this further recapitulates a shallower binding mode of CCL7 to DARC. Importantly, the shallower binding of CCL7 with DARC translates to an absence of interactions between several residues in chemokines and TM1, TM2, TM3, TM4, ECL2, and TM5, observed in prototypical chemokine receptors (Figure 5H). Thus, it is tempting to speculate that a superficial binding mode of chemokines to DARC, as observed here for CCL7, may impart chemokine promiscuity, although it remains to be experimentally explored.

Structural features of CCL7-bound DARC

In order to gain insights into the overall structural features of CCL7-bound DARC, we compared our structure with the previously reported crystal structure of CCR2 in its inactive conformation^{62,63} and cryo-EM structure of the same in its active conformation.⁵⁵ When compared with the inactive structure of CCR2 (PDB: 6GPS), TM5 and TM6 exhibit outward tilt angles of $\sim 35^\circ$ and $\sim 12^\circ$, respectively (as measured from the $C\alpha$ of Val219 for TM5 and Trp254 for TM6), while TM7 shows an inward helical tilt of $\sim 28^\circ$ (as measured from the $C\alpha$ of Thr300) (Figure 6A). However, while TM5 exhibits an outward tilt of $\sim 35^\circ$ when compared with the CCL2-bound structure of CCR2 (PDB: 7XA3), TM6 and TM7 make inward tilt angles of $\sim 17^\circ$ and $\sim 8^\circ$, respectively, in the CCL7-bound structure of DARC (Figure 6A). We also observed an overall similar pattern of TM movements when comparing the CCL7-DARC structure with inactive and active structures of CCR5^{56,64} and CXCR2⁵⁷ (Figures S7D and S7E).

Interestingly, we observed that, when compared with CCR2, the cytoplasmic portion of TM3 in DARC forms a kink at an angle of $>60^\circ$ at position Ala151^{3,47}, while the intracellular loop 2 (ICL2)

(G) Pairs of chemokine-chemokine receptor structures are shown to highlight the position of N termini of chemokines at the orthosteric pocket. Distance between the N terminus and the conserved toggle switch residue (Trp^{6,48}) has been calculated in all structures. The N terminus of CCL7 is the farthest from Trp^{6,48} compared with the other pairs (CXCL12-ACKR3, PDB: 7SK8; CCL15-CCR1, PDB: 7VL9; CCL2-CCR2, PDB: 7XA3; CCL5-CCR5, PDB: 7O7F; CCL20-CCR6, PDB: 6WWZ; CXCL8-CXCR2, PDB: 6LFO; CX₃CL1-CX₃CR1, PDB: 7XBX).

(H) Alignment of the interface residues between chemokines and their respective chemokine receptor structures have been provided. The Ballesteros-Weinstein positions are also mentioned below the TM regions. CCL7 makes the least number of contacts with DARC as compared with the other chemokine-chemokine receptor structures. The conserved interface residues in receptors are denoted as cyan-colored stars. See also Figure S7.

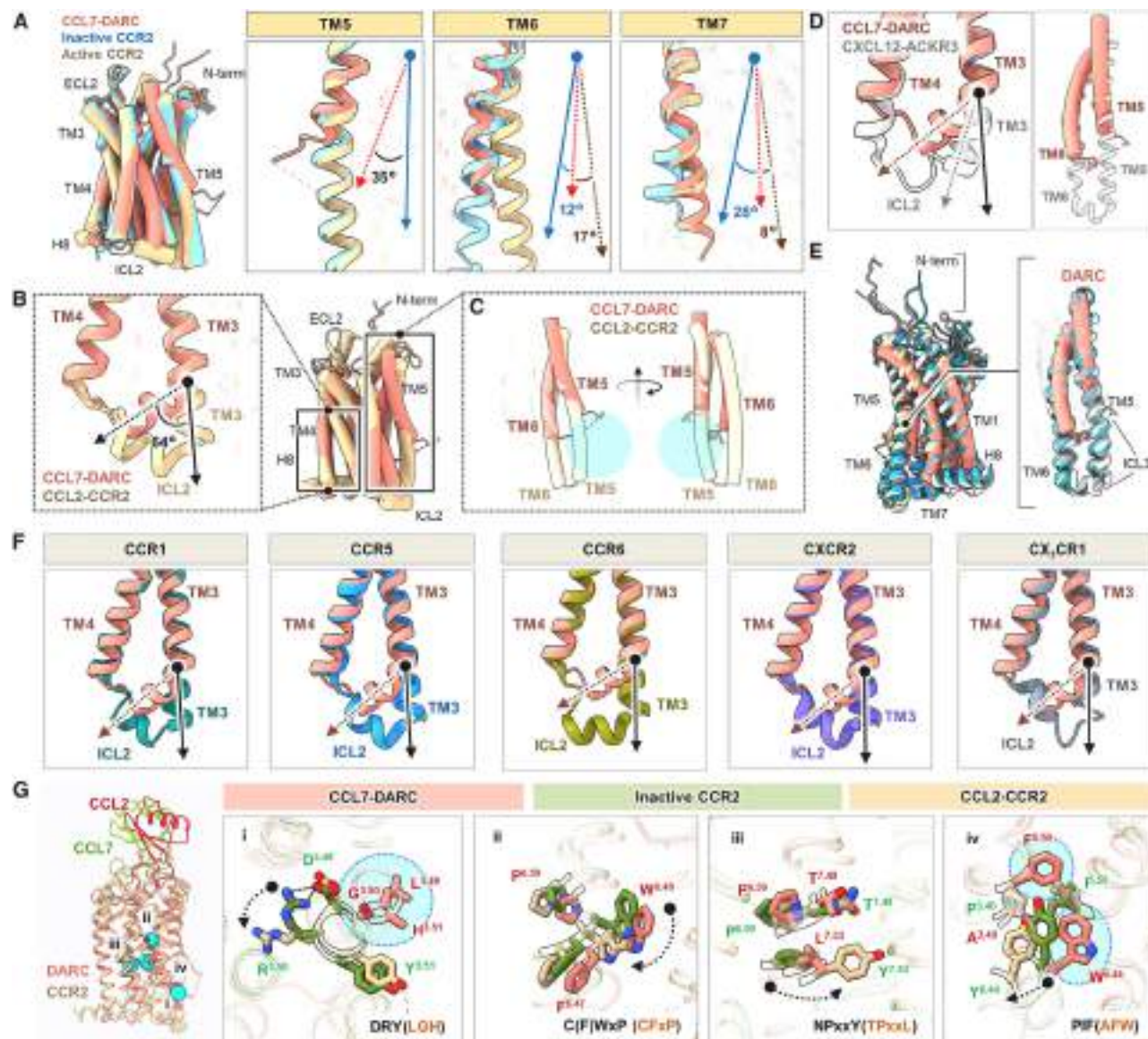


Figure 6. Divergent structural features of the 7TM domain in DARC

(A) Structural alignment of CCL7-DARC with the inactive (PDB: 6GPS) and active (PDB: 7XA3) structures of CCR2 to highlight the changes in TM5, TM6, and TM7 (left). The deviation angles of TM5, TM6, and TM7 in CCL7-DARC, with respect to the inactive and active structure of CCR2, are shown in blue and brown, respectively. (Arrows with blue, red and brown depict the TMs of inactive CCR2, DARC and active CCR2, respectively).

(B) Conformations of ICL2 and TM4 were found to be unique in DARC as compared with the CCL2-CCR2 structure (PDB: 7XA3). The cytoplasmic end of TM3 forms a kink and translates about 64° in comparison with that of CCR2, probably due to a shorter ICL2.

(C) TM5 and TM6 are shorter in length compared with that of CCR2. In addition, TM5 exhibits an outward shift.

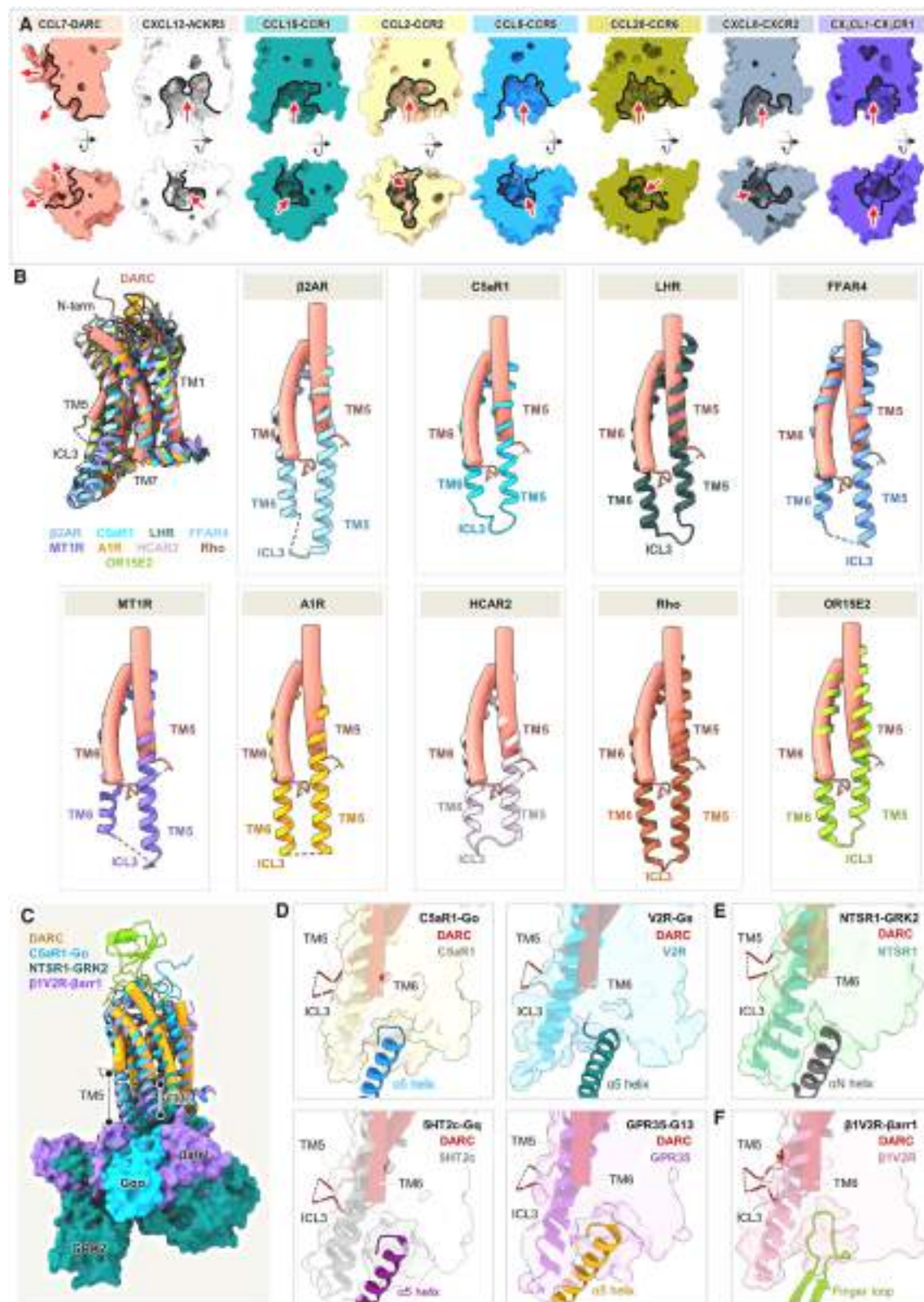
(D) TM3 in CXCL12-ACKR3 (PDB: 7SK8) forms a relatively smaller kink toward the cytoplasmic side when compared with CCL7-DARC (left). DARC harbors relatively shorter TM5 and TM6 as compared with ACKR3 (right).

(E) Superimposition of CCL7-bound DARC with active structures of chemokine-chemokine receptor pairs. Salmon, CCL7-DARC; gray, CXCL12-ACKR3 (PDB: 7SK8); blue, CCL5-CCR5 (PDB: 7O7F); beige, CCL2-CCR2 (PDB: 7XA3); deep gray, CXCL8-CXCR2 (PDB: 6LFO); and teal, CCL15-CCR1 (PDB: 7VL9). DARC has been shown in cylinders and other structures are in ribbon representation.

(F) Conformations of ICL2 and TM4 in active chemokine upon alignment with CCL7-bound DARC (CCL15-CCR1, PDB: 7VL9; CCL5-CCR5, PDB: 7O7F; CCL20-CCR6, PDB: 6WWZ; CXCL8-CXCR2, PDB: 6LFO; CX3CL1-CX3CR1, PDB: 7XBX).

(G) The activation hallmark microswitches conserved in class A receptors are shown in cyan spheres (left). Positions of microswitches are different in the CCL7-bound DARC structure when compared with the classical GPCRs. The inactive (PDB: 6GPS) and active (PDB: 7XA3) structures of CCR2 have been taken as reference.

See also [Figures S7](#) and [S8](#) and [Table S5](#).



(legend on next page)

is relatively shorter (Figure 6B). Strikingly, we also observed a significant shortening of TM5 and 6 in DARC compared with CCR2, although the ICL3 region spanning residues Gly227 to Asp238 is not resolved due to inherent flexibility (Figure 6C). It is worth noting that the kink observed in TM3 of DARC is more pronounced than that observed in CXCR7, while the shortening of TM5 and 6 is not apparent in CXCR7 (Figure 6D). Moreover, the TM3 kink and TM5/6 shortening is not observed in any of the previously determined active state structures of chemokine receptors and, therefore, it appears to be a distinct feature of DARC (Figures 6E and 6F).

Next, we compared the conformational changes in the sequences corresponding to the conserved motifs present in prototypical GPCRs such as the DRY, CWxP, NPxxY, and PIF motif. DARC lacks most of these motifs in its primary sequence and instead harbors altered sequences in the corresponding regions, which display significantly different orientations compared with those observed in CCL2-bound CCR2 (Figure 6G). It is interesting to note that, similar to most chemokine receptors, DARC also contains a conserved P-C motif, constituted by Cys51 along with Pro50 in the N terminus of the receptor. Although the P-C motif in other chemokine receptors is located at the N-terminal loop immediately preceding TM1, and helps to bend the conformation of the N-terminal loop, the P-C motif in DARC adopts a linear conformation and is positioned away from TM1. The region of the N terminus of DARC containing the P-C motif docks into a hydrophobic cavity in CCL7, wherein Pro50^{N-term} engages with Ile⁴² and Cys⁵² of CCL7 while Cys51^{N-term} interacts with Cys¹¹ of CCL7 (Figures S8A–S8C).

In order to measure CCL7-induced structural changes in DARC, we employed hydrogen-deuterium exchange mass spectrometry (HDX-MS) and compared the deuterium exchange for a ligand-free and CCL7-bound receptor. Although we observed limited coverage of the receptor, as is typical with membrane proteins, we observed a significant decrease in deuterium uptake in several regions of the receptor, including ECL1, TM3, ECL2, and the cytoplasmic end of TM5 upon binding of CCL7 (Figure S8D; Table S5). Considering that these regions are not directly involved in ligand binding, it likely reflects allosteric conformational changes in the receptor induced by binding of CCL7. Interestingly, the cytoplasmic ends of TM5 and 6,

which exhibit maximal structural changes in prototypical GPCRs upon activation, do not appear to undergo major conformational changes in DARC, suggesting a distinct activation mechanism that remains to be experimentally determined.

Structural basis of lack of canonical transducer coupling

For prototypical GPCRs, including the chemokine receptors, agonist-induced activation results in a significant outward movement of TM5 and TM6, resulting in the formation of a cleft on the cytoplasmic side of the receptors (Figure 7A). This cytoplasmic cleft serves as the docking interface for the positioning of the $\alpha 5$ helix of G proteins,^{65–70} αN helix of GRKs,^{71,72} and the finger loop of β arrestins,⁷³ leading to stable coupling and subsequent activation. Specifically, this binding cleft on the receptor helps in mediating extensive interaction with the transducers through residues spanning TM3, TM5, TM6, ICL2, and ICL3.⁶⁶ The shortening of TM5 and 6 is not observed in other chemokine receptors and prototypical GPCRs^{68,74–81} (Figure 7B) and, together with the distinct kink in TM3 and short ICL2, precludes the formation of such a binding cavity on the cytoplasmic side of DARC, thereby presumably preventing the interaction with G proteins, GRKs, and β arrestins (Figures 7C–7F). Taken together, these data demonstrate how the 7TM fold in DARC has evolved to encode a chemokine scavenging function in order to mediate chemokine homeostasis without canonical effector coupling and activation.

DISCUSSION

Chemokine receptors typically behave as prototypical GPCRs, with primary coupling to the Gi subtype of G proteins, and exhibit GRK-mediated phosphorylation followed by β arrestin recruitment. Interestingly, however, several chemokine receptors classified as ACKRs, couple exclusively to β arrestins, without any measurable G protein activation; they are also referred to as arrestin-coupled receptors (ACRs). DARC has also been classified as an ACKR, i.e., ACKR1; however, our comprehensive analysis now separates it from the other ACKRs with respect to canonical transducer-coupling profile. So, why does it fail to engage with canonical signal transducers? As mentioned earlier, CCL7 binds to DARC primarily through CRS1, without a significant involvement of CRS2. However, previous studies have proposed that in the

Figure 7. A schematic summary of distinct structural and functional features of DARC

(A) Comparison of CXCL12-ACKR3 (PDB: 7SK8), CCL15-CCR1 (PDB: 7VL9), CCL2-CCR2 (PDB: 7XA3), CCL5-CCR5 (PDB: 7O7F), CCL20-CCR6 (PDB: 6WWZ), CXCL2-CXCR2 (PDB: 6LFO), and CX₃CL1-CX₃CR1 (PDB: 7XBX), with CCL7-DARC structure shown as surface slice representation illustrating the formation of the transducer binding cavity as opposed to CCL7-DARC. Red arrows highlight the formed cytoplasmic cavity.

(B) Relative lengths of TM5 and TM6 have been compared with active state classical GPCRs. A single receptor from each sub-family has been selected for comparison. (β 2AR, PDB: 3SN6; C5aR1, PDB: 8HQC; LHR, PDB: 7FIG; FFAR4, PDB: 8H4I; MT1R, PDB: 7VGZ; A1R, PDB: 6D9H; HCAR2, PDB: 7XK2; Rho, PDB: 6FUF; OR51E2, PDB: 8F76).

(C) Alignment of the CCL7-DARC structure with C5aR1-Gi (PDB: 8IA2), NTSR1-GRK2 (PDB: 8JPB), and β 1V2R- β arr1 (PDB: 6TKO) highlighting the short TM5 and TM6 in DARC compared with other receptors.

(D) Structural superimposition of DARC and various receptors in complex with G proteins. (Top) C5aR1-Gi (PDB: 8IA2) and V2R-Gs (PDB: 7BB6), (bottom) 5HT2c-Gq (PDB: 8DPF) and GPR35-G13 (PDB: 8H8J). DARC (tube helices) and G proteins (ribbon helices) are shown as cartoons and other receptors as transparent surfaces.

(E) Structural alignment of CCL7-DARC structure with NTSR1-GRK2 (PDB: 8JPB). DARC (tube helices) and GRK2 (ribbon helices) are shown as cartoons and NTSR1 as a transparent surface.

(F) Structural alignment of CCL7-DARC structure with β 1V2R- β arr1 (PDB: 6TKO). DARC (tube helices) and β arr1 (ribbon representation) are shown as cartoons and β 1V2R as a transparent surface.

See also Figure S8.

two-site-binding mechanism, CRS2 engagement by chemokines is important for allosterically directing transducer coupling and effector activation.⁵⁴ Therefore, it is tempting to speculate that the absence of CRS2 engagement by chemokines upon binding to DARC, taken together with the dramatic shortening of TM5/6, is the primary driving mechanism underlying the functional divergence displayed by this receptor (Figure S8E). The same remains to be established experimentally in future studies.

Although ACKRs are proposed to primarily serve chemokine scavenging functions,^{34,35} emerging evidence suggests their signaling capabilities in multiple cell types.^{39,82–84} Therefore, it would be important to probe the same for DARC in future studies, especially considering the recent data suggesting its expression in non-erythrocyte cell types and emerging indications of its fundamental role in several immune-physiological processes such as hematopoiesis.⁸⁵ Our global phosphoproteomics and interactome analysis now provides possible hints at downstream signaling for DARC and presents a framework for systematic experimental studies to decipher the non-canonical signaling pathways and corresponding cellular outcomes going forward. It is also important to note that although we used a full-length expression construct of DARC, the proximal N terminus of the receptor is not resolved in the structure, and, therefore, the quest to understand the interaction of Plasmodium vivax Duffy binding protein (PvDBP) and PFTs to DARC remains open. Furthermore, the interaction interface and binding mode of the C-X-C type chemokines to DARC also remain to be visualized directly in order to better understand the ligand promiscuity in terms of the dual C-C and C-X-C chemokine recognition exhibited by DARC, which is typically not observed for other chemokine receptors.

In summary, we present a cryo-EM structure of CCL7-bound DARC that elucidates the plausible molecular mechanism underlying chemokine scavenging and homeostasis, even in the absence of canonical activation and signaling. This study should pave the way for further molecular and structural characterization of the intriguing functional divergence encoded in the 7TM scaffold exemplified by DARC and facilitate the structure-guided design of better therapeutics.

Limitations of the study

Although our phosphoproteomics and interactome analysis provide clear indications of the functional capabilities of DARC, and we experimentally validate DARC-CD82 interaction, we also note that further in-depth studies are required to decipher and construct the precise downstream signaling pathways. We also note that during cryo-EM data processing, the initial angular assignments were not performed with GS-FSC refinement, and subsequent searches were all kept local because regular, non-uniform refinement in cryoSPARC and maximum likelihood refinement in Relion did not yield reasonable reconstructions, likely due to the low signal-to-noise ratio of the particles.

STAR★METHODS

Detailed methods are provided in the online version of this paper and include the following:

- **KEY RESOURCES TABLE**

- **RESOURCE AVAILABILITY**

- Lead contact
- Materials availability
- Data and code availability

- **EXPERIMENTAL MODEL AND SUBJECT DETAILS**

- Human cell lines
- Insect cells

- **METHOD DETAILS**

- General reagents, plasmids, and cell culture
- Second messenger signaling assays
- NanoBIT-based G protein dissociation assay
- Bioluminescence Resonance Energy Transfer (BRET)-based GRK recruitment assay
- NanoBIT-based β -arrestin/GRK recruitment assay
- Confocal microscopy to visualize β -arrestin1/2 trafficking
- Co-immunoprecipitation to detect physical interaction between DARC and β -arrestin1/2
- TANGO Assay to measure β -arrestin2 recruitment
- Receptor surface expression assay
- Phosphoproteomics analysis
- Mass spectrometry based interactome analysis
- STRING analysis and DARC-CD82 interaction
- Purification of DARC
- Purification of CCL7
- Purification of Nb52
- Reconstitution of complexes
- Negative staining electron microscopy
- Cryo-EM data collection and acquisition
- Cryo-EM data processing
- Model building and validation
- Hydrogen-deuterium exchange mass spectrometry

- **QUANTIFICATION AND STATISTICAL ANALYSIS**

SUPPLEMENTAL INFORMATION

Supplemental information can be found online at <https://doi.org/10.1016/j.cell.2024.07.005>.

ACKNOWLEDGMENTS

The research on the Duffy antigen receptor in A.K.S.'s laboratory was supported previously by the Intermediate Fellowship of the DBT Wellcome Trust India Alliance (IA/I/14/1/501285), the Swarnajayanti Fellowship of the Department of Science and Technology (DST/SJF/LSA-03/2017-18), an MHRD-STARs grant (STARs/APR2019/BS/171/FS), and currently by the Department of Biotechnology (BT/PR47867/COT/142/59/2023). The ongoing work in A.K.S.'s laboratory is also supported by the Senior Fellowship of the DBT Wellcome Trust India Alliance (IA/S/20/1/504916), Science and Engineering Research Board (SPR/2020/000408 and IPA/2020/000405), Indian Council of Medical Research (F.NO.52/15/2020/BIO/BMS), Young Scientist Award from Lady Tata Memorial Trust, and IIT Kanpur. A.K.S. is an EMBO Young Investigator and Sonu Agrawal Memorial Chair. S. Saha is funded by Prime Minister's Research Fellowship (PMRF). We thank M. Baruah and S. Mahapatra for help with Nb52 purification and M. Yadav for help with receptor purification. The work in V.M.K.'s laboratory was supported by a Swiss National Science Foundation Sinergia grant (198545). HDX-MS work in K.Y.C.'s laboratory was supported by grants from the National Research Foundation of Korea funded by the Korean Government (NRF-2021R1A2C3003518 and NRF-2019R1A5A2027340). A.I. was funded via KAKENHI JP21H04791 and JP21H05113 from Japan Society for the Promotion of Science (JSPS), JPMJFR215T and JPMJMS2023 from Japan Science and Technology Agency (JST), and JP22ama121038 and JP22zf0127007 from the Japan Agency for Medical Research and Development (AMED). We also thank Kayo Sato, Shigeo Nakano, and Ayumi Inoue in A.I.'s laboratory for their assistance in plasmid preparation and NanoBIT assays related to G protein dissociation and GRK recruitment. The work in B.P.'s laboratory was supported by a

Wellcome Trust Seed Award in Science (215229/Z/19/Z), and C.D. was funded by a PhD studentship from the Department for the Economy (DfE), Queen's University Belfast.

AUTHOR CONTRIBUTIONS

S. Saha expressed and purified ligand-receptor complexes, carried out the GloSensor and farr assays, prepared samples for phosphoproteomics and interactome analysis, with help from S. Sharma and N.Z., and carried out CD82-DARC interaction, with help from S. Sharma, N.Z., A.D., and S.M.; B.K. prepared cryo-EM grids, optimized data collection, and collected and processed cryo-EM under the supervision of V.M.K.; J.M. and R.B. processed cryo-EM data and determined the structure; J.M. prepared the figures with input from R.B. and S. Saha; M.G. and D.T. contributed with figure preparation during revision; C.M.C.C. performed G protein profiling and GRK interaction experiments using NanoBIT assay under the supervision of A.I.; C.D. and S.H. carried out BRET-based assay for GRK recruitment under the supervision of B.P.; H.K. performed the HDX-MS experiment under the supervision of K.Y.C.; P.K. carried out the calcium assay under the supervision of P.N.Y.; G.D.J. supervised the phosphoproteomics and interactome data analysis and presentation; V.M.K. and A.K.S. supervised the overall project and wrote the manuscript with input from all the authors.

DECLARATION OF INTERESTS

The authors declare no competing interests.

Received: September 3, 2023

Revised: April 13, 2024

Accepted: July 3, 2024

Published: July 31, 2024

REFERENCES

- Chaudhuri, A., Polyakova, J., Zbrzezna, V., Williams, K., Gulati, S., and Pogo, A.O. (1993). Cloning of Glycoprotein D Cdna, Which Encodes the Major Subunit of the Duffy Blood-Group System and the Receptor for the Plasmodium-Vivax Malaria Parasite. *Proc. Natl. Acad. Sci. USA* **90**, 10793–10797. <https://doi.org/10.1073/pnas.90.22.10793>.
- Cutbush, M., and Mollison, P.L. (1950). The Duffy blood group system. *Heredity (Edinb)* **4**, 383–389. <https://doi.org/10.1038/hdy.1950.31>.
- Hadley, T.J., Lu, Z.H., Wasniowska, K., Martin, A.W., Peiper, S.C., Hesselgesser, J., and Horuk, R. (1994). Postcapillary venule endothelial cells in kidney express a multispecific chemokine receptor that is structurally and functionally identical to the erythroid isoform, which is the Duffy blood group antigen. *J. Clin. Invest.* **94**, 985–991. <https://doi.org/10.1172/JCI117465>.
- Peiper, S.C., Wang, Z.X., Neote, K., Martin, A.W., Showell, H.J., Conklyn, M.J., Osborne, K., Hadley, T.J., Lu, Z.H., Hesselgesser, J., et al. (1995). The Duffy antigen/receptor for chemokines (DARC) is expressed in endothelial cells of Duffy negative individuals who lack the erythrocyte receptor. *J. Exp. Med.* **181**, 1311–1317. <https://doi.org/10.1084/jem.181.4.1311>.
- Landegger, L.D., Vasiljic, S., Fujita, T., Soares, V.Y., Seist, R., Xu, L., and Stankovic, K.M. (2019). Cytokine Levels in Inner Ear Fluid of Young and Aged Mice as Molecular Biomarkers of Noise-Induced Hearing Loss. *Front. Neurol.* **10**, 977. <https://doi.org/10.3389/fneur.2019.00977>.
- Al-Alwan, L.A., Chang, Y., Rousseau, S., Martin, J.G., Eidelman, D.H., and Hamid, Q. (2014). CXCL1 Inhibits Airway Smooth Muscle Cell Migration through the Decoy Receptor Duffy Antigen Receptor for Chemokines. *J. Immunol.* **193**, 1416–1426. <https://doi.org/10.4049/jimmunol.1302860>.
- Horuk, R., Martin, A., Hesselgesser, J., Hadley, T., Lu, Z.H., Wang, Z.X., and Peiper, S.C. (1996). The Duffy antigen receptor for chemokines: structural analysis and expression in the brain. *J. Leukoc. Biol.* **59**, 29–38. <https://doi.org/10.1002/jlb.59.1.29>.
- Horuk, R., Martin, A.W., Wang, Z., Schweitzer, L., Gerassimides, A., Guo, H., Lu, Z., Hesselgesser, J., Perez, H.D., Kim, J., et al. (1997). Expression of chemokine receptors by subsets of neurons in the central nervous system. *J. Immunol.* **158**, 2882–2890.
- Crawford, K.S., and Volkman, B.F. (2023). Prospects for targeting ACKR1 in cancer and other diseases. *Front. Immunol.* **14**, 1111960. <https://doi.org/10.3389/fimmu.2023.1111960>.
- Bachelier, F., Ben-Baruch, A., Burkhardt, A.M., Combadiere, C., Farber, J.M., Graham, G.J., Horuk, R., Sparre-Ulrich, A.H., Locati, M., Luster, A.D., et al. (2014). International Union of Basic and Clinical Pharmacology. [corrected]. International Union of Basic and Clinical Pharmacology. [corrected]. LXXXIX. Update on the extended family of chemokine receptors and introducing a new nomenclature for atypical chemokine receptors. *Pharmacol. Rev.* **66**, 1–79. <https://doi.org/10.1124/pr.113.007724>.
- Neote, K., Mak, J.Y., Kolakowski, L.F., and Schall, T.J. (1994). Functional and Biochemical Analysis of the Cloned Duffy Antigen - Identity with the Red Blood Cell Chemokine Receptor. *Blood* **84**, 44–52.
- Horuk, R. (2015). The Duffy antigen receptor for chemokines DARC/ACKR1. *Front. Immunol.* **6**, 279. <https://doi.org/10.3389/fimmu.2015.00279>.
- Horuk, R., Chitnis, C.E., Darbonne, W.C., Colby, T.J., Rybicki, A., Hadley, T.J., and Miller, L.H. (1993). A receptor for the malarial parasite Plasmodium vivax: the erythrocyte chemokine receptor. *Science* **261**, 1182–1184. <https://doi.org/10.1126/science.7689250>.
- Singh, S.K., Singh, A.P., Pandey, S., Yazdani, S.S., Chitnis, C.E., and Sharma, A. (2003). Definition of structural elements in Plasmodium vivax and P. knowlesi Duffy-binding domains necessary for erythrocyte invasion. *Biochem. J.* **374**, 193–198. <https://doi.org/10.1042/Bj20030622>.
- Mayor, A., Bir, N., Sawhney, R., Singh, S., Pattnaik, P., Singh, S.K., Sharma, A., and Chitnis, C.E. (2005). Receptor-binding residues lie in central regions of Duffy-binding-like domains involved in red cell invasion and cytoadherence by malaria parasites. *Blood* **105**, 2557–2563. <https://doi.org/10.1182/blood-2004-05-1722>.
- Singh, S.K., Hora, R., Belrhali, H., Chitnis, C.E., and Sharma, A. (2006). Structural basis for Duffy recognition by the malaria parasite Duffy-binding-like domain. *Nature* **439**, 741–744. <https://doi.org/10.1038/nature04443>.
- Batchelor, J.D., Zahm, J.A., and Tolia, N.H. (2011). Dimerization of Plasmodium vivax DBP is induced upon receptor binding and drives recognition of DARC. *Nat. Struct. Mol. Biol.* **18**, 908–914. <https://doi.org/10.1038/nsmb.2088>.
- Moskovitz, R., Pholcharee, T., DonVito, S.M., Guloglu, B., Lowe, E., Mohring, F., Moon, R.W., and Higgins, M.K. (2023). Structural basis for DARC binding in reticulocyte invasion by Plasmodium vivax. *Nat. Commun.* **14**, 3637. <https://doi.org/10.1038/s41467-023-39357-w>.
- Miller, L.H., Mason, S.J., Clyde, D.F., and McGinniss, M.H. (1976). The resistance factor to Plasmodium vivax in blacks. The Duffy-blood-group genotype, FyFy. *N. Engl. J. Med.* **295**, 302–304. <https://doi.org/10.1056/NEJM197608052950602>.
- Spaan, A.N., Reyes-Robles, T., Badiou, C., Cochet, S., Boguslawski, K.M., Yoong, P., Day, C.J., de Haas, C.J.C., van Kessel, K.P.M., Vandenesch, F., et al. (2015). Staphylococcus aureus Targets the Duffy Antigen Receptor for Chemokines (DARC) to Lyse Erythrocytes. *Cell Host Microbe* **18**, 363–370. <https://doi.org/10.1016/j.chom.2015.08.001>.
- Vasquez, M.T., Lubkin, A., Reyes-Robles, T., Day, C.J., Lacey, K.A., Jennings, M.P., and Torres, V.J. (2020). Identification of a domain critical for Staphylococcus aureus LukED receptor targeting and lysis of erythrocytes. *J. Biol. Chem.* **295**, 17241–17250. <https://doi.org/10.1074/jbc.RA120.015757>.

22. Lubkin, A., Lee, W.L., Alonzo, F., 3rd, Wang, C., Aligo, J., Keller, M., Giris, N.M., Reyes-Robles, T., Chan, R., O'Malley, A., et al. (2019). Staphylococcus aureus Leukocidins Target Endothelial DARC to Cause Lethality in Mice. *Cell Host Microbe* 25, 463–470.e9. <https://doi.org/10.1016/j.chom.2019.01.015>.
23. Grison, C.M., Lambey, P., Jeannot, S., Del Nero, E., Fontanel, S., Peysson, F., Heuninck, J., Sounier, R., Durroux, T., Leyrat, C., et al. (2021). Molecular insights into mechanisms of GPCR hijacking by Staphylococcus aureus. *Proc. Natl. Acad. Sci. USA* 118, e2108856118. <https://doi.org/10.1073/pnas.2108856118>.
24. Ramsuran, V., Kulkarni, H., He, W.J., Misana, K., Wright, E.J., Werner, L., Castiblanco, J., Dhanda, R., Le, T., Dolan, M.J., et al. (2011). Duffy-Null-Associated Low Neutrophil Counts Influence HIV-1 Susceptibility in High-Risk South African Black Women. *Clin. Infect. Dis.* 52, 1248–1256. <https://doi.org/10.1093/cid/cir119>.
25. Kulkarni, H., Marconi, V.C., He, W.J., Landrum, M.L., Okulicz, J.F., Delmar, J., Kazandjian, D., Castiblanco, J., Ahuja, S.S., Wright, E.J., et al. (2009). The Duffy-null state is associated with a survival advantage in leukopenic HIV-infected persons of African ancestry. *Blood* 114, 2783–2792. <https://doi.org/10.1182/blood-2009-04-215186>.
26. He, W., Neil, S., Kulkarni, H., Wright, E., Agan, B.K., Marconi, V.C., Dolan, M.J., Weiss, R.A., and Ahuja, S.K. (2008). Duffy antigen receptor for chemokines mediates trans-infection of HIV-1 from red blood cells to target cells and affects HIV-AIDS susceptibility. *Cell Host Microbe* 4, 52–62. <https://doi.org/10.1016/j.chom.2008.06.002>.
27. Lachgar, A., Jaureguiberry, G., Le Buenac, H., Bizzini, B., Zagury, J.F., Rappaport, J., and Zagury, D. (1998). Binding of HIV-1 to RBCs involves the Duffy antigen receptors for chemokines (DARC). *Biomed. Pharmacother.* 52, 436–439. [https://doi.org/10.1016/s0753-3322\(99\)80021-3](https://doi.org/10.1016/s0753-3322(99)80021-3).
28. Neote, K., Darbonne, W., Ogez, J., Horuk, R., and Schall, T.J. (1993). Identification of a Promiscuous Inflammatory Peptide Receptor on the Surface of Red Blood Cells. *J. Biol. Chem.* 268, 12247–12249.
29. Szabo, M.C., Soo, K.S., Zlotnik, A., and Schall, T.J. (1995). Chemokine class differences in binding to the Duffy antigen-erythrocyte chemokine receptor. *J. Biol. Chem.* 270, 25348–25351. <https://doi.org/10.1074/jbc.270.43.25348>.
30. Gardner, L., Patterson, A.M., Ashton, B.A., Stone, M.A., and Middleton, J. (2004). The human Duffy antigen binds selected inflammatory but not homeostatic chemokines. *Biochem. Biophys. Res. Commun.* 321, 306–312. <https://doi.org/10.1016/j.bbrc.2004.06.146>.
31. Kashiwazaki, M., Tanaka, T., Kanda, H., Ebisuno, Y., Izawa, D., Fukuma, N., Akimitsu, N., Sekimizu, K., Monden, M., and Miyasaka, M. (2003). A high endothelial venule-expressing promiscuous chemokine receptor DARC can bind inflammatory, but not lymphoid, chemokines and is dispensable for lymphocyte homing under physiological conditions. *Int. Immunol.* 15, 1219–1227. <https://doi.org/10.1093/intimm/dxg121>.
32. Klei, T.R.L., Agliarolo, F., Mul, F.P.J., Tol, S., Ligthart, P.C., Seignette, I.M., Geissler, J., van den Akker, E., and van Bruggen, R. (2019). Differential interaction between DARC and SDF-1 on erythrocytes and their precursors. *Sci. Rep.* 9, 16245. <https://doi.org/10.1038/s41598-019-52186-6>.
33. Gutjahr, J.C., Crawford, K.S., Jensen, D.R., Naik, P., Peterson, F.C., Samson, G.P.B., Legler, D.F., Duchene, J., Veldkamp, C.T., Rot, A., et al. (2021). The dimeric form of CXCL12 binds to atypical chemokine receptor 1. *Sci. Signal.* 14, eabc9012. <https://doi.org/10.1126/scisignal.abc9012>.
34. Ulvmar, M.H., Hub, E., and Rot, A. (2011). Atypical chemokine receptors. *Exp. Cell Res.* 317, 556–568. <https://doi.org/10.1016/j.yexcr.2011.01.012>.
35. Graham, G.J., Locati, M., Mantovani, A., Rot, A., and Thelen, M. (2012). The biochemistry and biology of the atypical chemokine receptors. *Immunol. Lett.* 145, 30–38. <https://doi.org/10.1016/j.imlet.2012.04.004>.
36. Nibbs, R.J.B., and Graham, G.J. (2013). Immune regulation by atypical chemokine receptors. *Nat. Rev. Immunol.* 13, 815–829. <https://doi.org/10.1038/nri3544>.
37. Cancellieri, C., Vacchini, A., Locati, M., Bonecchi, R., and Borroni, E.M. (2013). Atypical chemokine receptors: from silence to sound. *Biochem. Soc. Trans.* 41, 231–236. <https://doi.org/10.1042/BST20120246>.
38. Matti, C., Salnikow, A., Artinger, M., D'Agostino, G., Kindinger, I., Ugucioni, M., Thelen, M., and Legler, D.F. (2020). ACKR4 Recruits GPR3 Prior to beta-Arrestins but Can Scavenge Chemokines in the Absence of beta-Arrestins. *Front. Immunol.* 11, 720. <https://doi.org/10.3389/fimmu.2020.00720>.
39. Pandey, S., Kumari, P., Baidya, M., Kise, R., Cao, Y., Dwivedi-Agnihotri, H., Banerjee, R., Li, X.X., Cui, C.S., Lee, J.D., et al. (2021). Intrinsic bias at non-canonical, beta-arrestin-coupled seven transmembrane receptors. *Mol. Cell* 81, 4605–4621.e11. <https://doi.org/10.1016/j.molcel.2021.09.007>.
40. Sarma, P., Y.H., Carino, C.M., Deeksha, S., Banerjee, R., Yun, Y., Ji, J., Min, K., Pandey, S., Dwivedi-Agnihotri, H., et al. (2022). Molecular insights into intrinsic transducer-coupling bias in the CXCR4-CXCR7 system. *Nat. Commun.* 14, 4808.
41. Inoue, A., Raimondi, F., Kadji, F.M.N., Singh, G., Kishi, T., Uwamizu, A., Ono, Y., Shinjo, Y., Ishida, S., Arang, N., et al. (2019). Illuminating G-Protein-Coupling Selectivity of GPCRs. *Cell* 177, 1933–1947.e25. <https://doi.org/10.1016/j.cell.2019.04.044>.
42. Oakley, R.H., Laporte, S.A., Holt, J.A., Caron, M.G., and Barak, L.S. (2000). Differential affinities of visual arrestin, beta arrestin1, and beta arrestin2 for G protein-coupled receptors delineate two major classes of receptors. *J. Biol. Chem.* 275, 17201–17210. <https://doi.org/10.1074/jbc.M910348199>.
43. Baidya, M., Kumari, P., Dwivedi-Agnihotri, H., Pandey, S., Sokrat, B., Sposini, S., Chaturvedi, M., Srivastava, A., Roy, D., Hanyaloglu, A.C., et al. (2020). Genetically encoded intrabody sensors report the interaction and trafficking of beta-arrestin 1 upon activation of G-protein-coupled receptors. *J. Biol. Chem.* 295, 10153–10167. <https://doi.org/10.1074/jbc.RA120.013470>.
44. Barnea, G., Strapps, W., Herrada, G., Berman, Y., Ong, J., Kloss, B., Axel, R., and Lee, K.J. (2008). The genetic design of signaling cascades to record receptor activation. *Proc. Natl. Acad. Sci. USA* 105, 64–69. <https://doi.org/10.1073/pnas.0710487105>.
45. Hughes, C.E., and Nibbs, R.J.B. (2018). A guide to chemokines and their receptors. *FEBS J.* 285, 2944–2971. <https://doi.org/10.1111/febs.14466>.
46. Atwood, B.K., Lopez, J., Wager-Miller, J., Mackie, K., and Straker, A. (2011). Expression of G protein-coupled receptors and related proteins in HEK293, AtT20, BV2, and N18 cell lines as revealed by microarray analysis. *BMC Genomics* 12, 14. <https://doi.org/10.1186/1471-2164-12-14>.
47. Pruenster, M., Mudde, L., Bombosi, P., Dimitrova, S., Zsak, M., Middleton, J., Richmond, A., Graham, G.J., Segerer, S., Nibbs, R.J.B., et al. (2009). The Duffy antigen receptor for chemokines transports chemokines and supports their promigratory activity. *Nat. Immunol.* 10, 101–108. <https://doi.org/10.1038/ni.1675>.
48. Girbl, T., Lenn, T., Perez, L., Rolas, L., Barkaway, A., Thiriot, A., Del Fresno, C., Lynam, E., Hub, E., Thelen, M., et al. (2018). Distinct Compartmentalization of the Chemokines CXCL1 and CXCL2 and the Atypical Receptor ACKR1 Determine Discrete Stages of Neutrophil Diapedesis. *Immunity* 49, 1062–1076.e6. <https://doi.org/10.1016/j.immuni.2018.09.018>.
49. Cook, L.M., Hurst, D.R., and Welch, D.R. (2011). Metastasis suppressors and the tumor microenvironment. *Semin. Cancer Biol.* 21, 113–122. <https://doi.org/10.1016/j.semcancer.2010.12.005>.
50. Khanna, P., Chung, C.Y., Neves, R.I., Robertson, G.P., and Dong, C. (2014). CD82/KAI expression prevents IL-8-mediated endothelial gap formation in late-stage melanomas. *Oncogene* 33, 2898–2908. <https://doi.org/10.1038/onc.2013.249>.

51. Bandyopadhyay, S., Zhan, R., Chaudhuri, A., Watabe, M., Pai, S.K., Hirata, S., Hosobe, S., Tsukada, T., Miura, K., Takano, Y., et al. (2006). Interaction of KAI1 on tumor cells with DARC on vascular endothelium leads to metastasis suppression. *Nat. Med.* 12, 933–938. <https://doi.org/10.1038/nm1444>.
52. Hur, J., Choi, J.I., Lee, H., Nham, P., Kim, T.W., Chae, C.W., Yun, J.Y., Kang, J.A., Kang, J., Lee, S.E., et al. (2016). CD82/KAI1 Maintains the Dormancy of Long-Term Hematopoietic Stem Cells through Interaction with DARC-Expressing Macrophages. *Cell Stem Cell* 18, 508–521. <https://doi.org/10.1016/j.stem.2016.01.013>.
53. Smolarek, D., Hattab, C., Hassanzadeh-Ghassabeh, G., Cochet, S., Gutiérrez, C., de Brevern, A.G., Udonsangpetch, R., Picot, J., Grodecka, M., Wasniewska, K., et al. (2010). A recombinant dromedary antibody fragment (VHH or nanobody) directed against human Duffy antigen receptor for chemokines. *Cell. Mol. Life Sci.* 67, 3371–3387. <https://doi.org/10.1007/s00018-010-0387-6>.
54. Sonawani, A., Kharche, S., Dasgupta, D., and SenGupta, D. (2022). Insights into the dynamic interactions at chemokine-receptor interfaces and mechanistic models of chemokine binding. *J. Struct. Biol.* 214, 107877. <https://doi.org/10.1016/j.jsb.2022.107877>.
55. Shao, Z., Tan, Y., Shen, Q., Hou, L., Yao, B., Qin, J., Xu, P., Mao, C., Chen, L.N., Zhang, H., et al. (2022). Molecular insights into ligand recognition and activation of chemokine receptors CCR2 and CCR3. *Cell Discov.* 8, 44. <https://doi.org/10.1038/s41421-022-00403-4>.
56. Isaikina, P., Tsai, C.J., Dietz, N., Pamula, F., Grahl, A., Goldie, K.N., Guixà-González, R., Branco, C., Paolini-Bertrand, M., Calo, N., et al. (2021). Structural basis of the activation of the CC chemokine receptor 5 by a chemokine agonist. *Sci. Adv.* 7, eabg8685. <https://doi.org/10.1126/sciadv.abg8685>.
57. Liu, K., Wu, L., Yuan, S., Wu, M., Xu, Y., Sun, Q., Li, S., Zhao, S., Hua, T., and Liu, Z.J. (2020). Structural basis of CX3C chemokine receptor 2 activation and signalling. *Nature* 585, 135–140. <https://doi.org/10.1038/s41586-020-2492-5>.
58. Lu, M., Zhao, W., Han, S., Lin, X., Xu, T., Tan, Q., Wang, M., Yi, C., Chu, X., Yang, W., et al. (2022). Activation of the human chemokine receptor CX3CR1 regulated by cholesterol. *Sci. Adv.* 8, eabn8048. <https://doi.org/10.1126/sciadv.abn8048>.
59. Shao, Z., Shen, Q., Yao, B., Mao, C., Chen, L.N., Zhang, H., Shen, D.D., Zhang, C., Li, W., Du, X., et al. (2022). Identification and mechanism of G protein-biased ligands for chemokine receptor CCR1. *Nat. Chem. Biol.* 18, 264–271. <https://doi.org/10.1038/s41589-021-00918-z>.
60. Wasilko, D.J., Johnson, Z.L., Ammirati, M., Che, Y., Griffor, M.C., Han, S., and Wu, H. (2020). Structural basis for chemokine receptor CCR6 activation by the endogenous protein ligand CCL20. *Nat. Commun.* 11, 3031. <https://doi.org/10.1038/s41467-020-16820-6>.
61. Yen, Y.C., Schafer, C.T., Gustavsson, M., Eberle, S.A., Dominik, P.K., Deneka, D., Zhang, P., Schall, T.J., Kossiakoff, A.A., Tesmer, J.J.G., et al. (2022). Structures of atypical chemokine receptor 3 reveal the basis for its promiscuity and signaling bias. *Sci. Adv.* 8, eabn8063. <https://doi.org/10.1126/sciadv.abn8063>.
62. Zheng, Y., Qin, L., Zacarias, N.V.O., de Vries, H., Han, G.W., Gustavsson, M., Dabros, M., Zhao, C., Cherney, R.J., Carter, P., et al. (2016). Structure of CC chemokine receptor 2 with orthosteric and allosteric antagonists. *Nature* 540, 458–461. <https://doi.org/10.1038/nature20605>.
63. Apel, A.K., Cheng, R.K.Y., Tautermann, C.S., Brauchle, M., Huang, C.Y., Pautsch, A., Hennig, M., Nar, H., and Schnapp, G. (2019). Crystal Structure of CC Chemokine Receptor 2A in Complex with an Orthosteric Antagonist Provides Insights for the Design of Selective Antagonists. *Structure* 27, 427–438.e5. <https://doi.org/10.1016/j.str.2018.10.027>.
64. Zheng, Y., Han, G.W., Abagyan, R., Wu, B., Stevens, R.C., Cherezov, V., Kufareva, I., and Handel, T.M. (2017). Structure of CC Chemokine Receptor 5 with a Potent Chemokine Antagonist Reveals Mechanisms of Chemokine Recognition and Molecular Mimicry by HIV. *Immunity* 46, 1005–1017.e5. <https://doi.org/10.1016/j.immuni.2017.05.002>.
65. Rosenbaum, D.M., Rasmussen, S.G.F., and Kobilka, B.K. (2009). The structure and function of G-protein-coupled receptors. *Nature* 459, 356–363. <https://doi.org/10.1038/nature08144>.
66. Weis, W.I., and Kobilka, B.K. (2018). The Molecular Basis of G Protein-Coupled Receptor Activation. *Annu. Rev. Biochem.* 87, 897–919. <https://doi.org/10.1146/annurev-biochem-060614-033910>.
67. Bous, J., Orcel, H., Floquet, N., Leyrat, C., Lai-Kee-Him, J., Gaibelet, G., Ancelin, A., Saint-Paul, J., Trapani, S., Louet, M., et al. (2021). Cryo-electron microscopy structure of the antidiuretic hormone arginine-vasopressin V2 receptor signaling complex. *Sci. Adv.* 7, eabg5628. <https://doi.org/10.1126/sciadv.abg5628>.
68. Yadav, M.K., Maharana, J., Yadav, R., Saha, S., Sarma, P., Soni, C., Singh, V., Saha, S., Ganguly, M., Li, X.X., et al. (2023). Molecular basis of anaphylatoxin binding, activation, and signaling bias at complement receptors. *Cell* 186, 4956–4973.e21. <https://doi.org/10.1016/j.cell.2023.09.020>.
69. Duan, J., Liu, Q., Yuan, Q., Ji, Y., Zhu, S., Tan, Y., He, X., Xu, Y., Shi, J., Cheng, X., et al. (2022). Insights into divalent cation regulation and G₁₃-coupling of orphan receptor GPR35. *Cell Discov.* 8, 135. <https://doi.org/10.1038/s41421-022-00499-8>.
70. Gumpfer, R.H., Fay, J.F., and Roth, B.L. (2022). Molecular insights into the regulation of constitutive activity by RNA editing of 5HT_{2C} serotonin receptors. *Cell Rep.* 40, 111211. <https://doi.org/10.1016/j.celrep.2022.111211>.
71. Chen, Q., Plasencia, M., Li, Z., Mukherjee, S., Patra, D., Chen, C.L., Klose, T., Yao, X.Q., Kossiakoff, A.A., Chang, L., et al. (2021). Structures of rhodopsin in complex with G-protein-coupled receptor kinase 1. *Nature* 595, 600–605. <https://doi.org/10.1038/s41586-021-03721-x>.
72. Duan, J., Liu, H., Zhao, F., Yuan, Q., Ji, Y., Cai, X., He, X., Li, X., Li, J., Wu, K., et al. (2023). GPCR activation and GRK2 assembly by a biased intracellular agonist. *Nature* 620, 676–681. <https://doi.org/10.1038/s41586-023-06395-9>.
73. Lee, Y., Warne, T., Nehmé, R., Pandey, S., Dwivedi-Agnihotri, H., Chaturvedi, M., Edwards, P.C., García-Nafria, J., Leslie, A.G.W., Shukla, A.K., et al. (2020). Molecular basis of beta-arrestin coupling to formoterol-bound β_1 -adrenoceptor. *Nature* 583, 862–866. <https://doi.org/10.1038/s41586-020-2419-1>.
74. Billesbølle, C.B., de March, C.A., van der Velden, W.J.C., Ma, N., Tewari, J., Del Torrent, C.L., Li, L., Faust, B., Vaidehi, N., Matsunami, H., et al. (2023). Structural basis of odorant recognition by a human odorant receptor. *Nature* 615, 742–749. <https://doi.org/10.1038/s41586-023-05798-y>.
75. Draper-Joyce, C.J., Khoshouei, M., Thal, D.M., Liang, Y.L., Nguyen, A.T.N., Furness, S.G.B., Venugopal, H., Baltos, J.A., Plitzko, J.M., Danev, R., et al. (2018). Structure of the adenosine-bound human adenosine A₁ receptor-G_i complex. *Nature* 558, 559–563. <https://doi.org/10.1038/s41586-018-0236-6>.
76. Duan, J., Xu, P., Cheng, X., Mao, C., Croll, T., He, X., Shi, J., Luan, X., Yin, W., You, E., et al. (2021). Structures of full-length glycoprotein hormone receptor signalling complexes. *Nature* 598, 688–692. <https://doi.org/10.1038/s41586-021-03924-2>.
77. Rasmussen, S.G.F., DeVree, B.T., Zou, Y., Kruse, A.C., Chung, K.Y., Kobilka, T.S., Thian, F.S., Chae, P.S., Pardon, E., Calinski, D., et al. (2011). Crystal structure of the beta2 adrenergic receptor-Gs protein complex. *Nature* 477, 549–555. <https://doi.org/10.1038/nature10361>.
78. Tsai, C.J., Pamula, F., Nehmé, R., Mühle, J., Weinert, T., Flock, T., Nogly, P., Edwards, P.C., Carpenter, B., Gruhl, T., et al. (2018). Crystal structure of rhodopsin in complex with a mini-G_o sheds light on the principles of G protein selectivity. *Sci. Adv.* 4, eaat7052. <https://doi.org/10.1126/sciadv.aat7052>.
79. Wang, Q., Lu, Q., Guo, Q., Teng, M., Gong, Q., Li, X., Du, Y., Liu, Z., and Tao, Y. (2022). Structural basis of the ligand binding and signaling mechanism of melatonin receptors. *Nat. Commun.* 13, 454. <https://doi.org/10.1038/s41467-022-28111-3>.

80. Yang, Y., Kang, H.J., Gao, R., Wang, J., Han, G.W., DiBerto, J.F., Wu, L., Tong, J., Qu, L., Wu, Y., et al. (2023). Structural insights into the human niacin receptor HCA2-G_i signalling complex. *Nat. Commun.* **14**, 1692. <https://doi.org/10.1038/s41467-023-37177-6>.
81. Yin, H., Inoue, A., Ma, Z., Zhu, X., Xia, R., Xu, Z., Wang, N., Duan, Y., Zhang, A., Guo, C., et al. (2023). Structural basis of omega-3 fatty acid receptor FFAR4 activation and G protein coupling selectivity. *Cell Res.* **33**, 644–647. <https://doi.org/10.1038/s41422-023-00835-x>.
82. Rajagopal, S., Kim, J., Ahn, S., Craig, S., Lam, C.M., Gerard, N.P., Gerard, C., and Lefkowitz, R.J. (2010). Beta-arrestin- but not G protein-mediated signaling by the “decoy” receptor CXCR7. *Proc. Natl. Acad. Sci. USA* **107**, 628–632. <https://doi.org/10.1073/pnas.0912852107>.
83. Pandey, S., Maharana, J., Li, X.X., Woodruff, T.M., and Shukla, A.K. (2020). Emerging Insights into the Structure and Function of Complement C5a Receptors. *Trends Biochem. Sci.* **45**, 693–705. <https://doi.org/10.1016/j.tibs.2020.04.004>.
84. Borroni, E.M., Cancellieri, C., Vacchini, A., Benureau, Y., Lagane, B., Bachelier, F., Arenzana-Seisdedos, F., Mizuno, K., Mantovani, A., Bonocchi, R., et al. (2013). β -Arrestin-Dependent Activation of the Cofilin Pathway Is Required for the Scavenging Activity of the Atypical Chemokine Receptor D6. *Sci. Signal.* **6**, ra30.
85. Duchene, J., Novitzky-Basso, I., Thiriot, A., Casanova-Acebes, M., Bianchini, M., Etheridge, S.L., Hub, E., Nitz, K., Artinger, K., Eller, K., et al. (2017). Atypical chemokine receptor 1 on nucleated erythroid cells regulates hematopoiesis. *Nat. Immunol.* **18**, 753–761. <https://doi.org/10.1038/ni.3763>.
86. Zivanov, J., Nakane, T., Forsberg, B.O., Kimanius, D., Hagen, W.J., Lindahl, E., and Scheres, S.H. (2018). New tools for automated high-resolution cryo-EM structure determination in RELION-3. *eLife* **7**, e42166. <https://doi.org/10.7554/eLife.42166>.
87. Kawakami, K., Yanagawa, M., Hiratsuka, S., Yoshida, M., Ono, Y., Hiroshima, M., Ueda, M., Aoki, J., Sako, Y., and Inoue, A. (2022). Heterotrimeric Gq proteins act as a switch for GRK5/6 selectivity underlying beta-arrestin transducer bias. *Nat. Commun.* **13**, 487. <https://doi.org/10.1038/s41467-022-28056-7>.
88. Goncharuk, M.V., Roy, D., Dubinnyi, M.A., Nadezhdin, K.D., Srivastava, A., Baidya, M., Dwivedi-Agnihotri, H., Arseniev, A.S., and Shukla, A.K. (2020). Purification of native CCL7 and its functional interaction with selected chemokine receptors. *Protein Expr. Purif.* **171**, 105617. <https://doi.org/10.1016/j.pep.2020.105617>.
89. Zivanov, J., Nakane, T., and Scheres, S.H.W. (2020). Estimation of high-order aberrations and anisotropic magnification from cryo-EM data sets in RELION-3.1. *IUCr J* **7**, 253–267. <https://doi.org/10.1107/S2052252520000081>.
90. Zivanov, J., Otón, J., Ke, Z., von Kügelgen, A., Pyle, E., Qu, K., Morado, D., Castaño-Díez, D., Zanetti, G., Bharat, T.A.M., et al. (2022). A Bayesian approach to single-particle electron cryo-tomography in RELION-4.0. *eLife* **11**, e83724. <https://doi.org/10.7554/eLife.83724>.
91. Punjani, A., Rubinstein, J.L., Fleet, D.J., and Brubaker, M.A. (2017). cryoSPARC: algorithms for rapid unsupervised cryo-EM structure determination. *Nat. Methods* **14**, 290–296. <https://doi.org/10.1038/nmeth.4169>.
92. Pettersen, E.F., Goddard, T.D., Huang, C.C., Meng, E.C., Couch, G.S., Croll, T.I., Morris, J.H., and Ferrin, T.E. (2021). UCSF ChimeraX: Structure visualization for researchers, educators, and developers. *Protein Sci.* **30**, 70–82. <https://doi.org/10.1002/pro.3943>.
93. Pettersen, E.F., Goddard, T.D., Huang, C.C., Couch, G.S., Greenblatt, D.M., Meng, E.C., and Ferrin, T.E. (2004). UCSF Chimera—a visualization system for exploratory research and analysis. *J. Comput. Chem.* **25**, 1605–1612. <https://doi.org/10.1002/jcc.20084>.
94. Emsley, P., Lohkamp, B., Scott, W.G., and Cowtan, K. (2010). Features and development of Coot. *Acta Crystallogr. D Biol. Crystallogr.* **66**, 486–501. <https://doi.org/10.1107/S0907444910007493>.
95. Emsley, P., and Cowtan, K. (2004). Coot: model-building tools for molecular graphics. *Acta Crystallogr. D Biol. Crystallogr.* **60**, 2126–2132. <https://doi.org/10.1107/S0907444904019158>.
96. Liebschner, D., Afonine, P.V., Baker, M.L., Bunkóczi, G., Chen, V.B., Croll, T.I., Hintze, B., Hung, L.W., Jain, S., McCoy, A.J., et al. (2019). Macromolecular structure determination using X-rays, neutrons and electrons: recent developments in Phenix. *Acta Crystallogr. D Struct. Biol.* **75**, 861–877. <https://doi.org/10.1107/S2059798319011471>.
97. Adams, P.D., Afonine, P.V., Bunkóczi, G., Chen, V.B., Davis, I.W., Echols, N., Headd, J.J., Hung, L.W., Kapral, G.J., Grosse-Kunstleve, R.W., et al. (2010). PHENIX: a comprehensive Python-based system for macromolecular structure solution. *Acta Crystallogr. D Biol. Crystallogr.* **66**, 213–221. <https://doi.org/10.1107/S0907444909052925>.
98. Krissinel, E., and Henrick, K. (2007). Inference of macromolecular assemblies from crystalline state. *J. Mol. Biol.* **372**, 774–797. <https://doi.org/10.1016/j.jmb.2007.05.022>.
99. Laskowski, R.A., Jabłońska, J., Právda, L., Vařeková, R.S., and Thornton, J.M. (2018). PDBsum: Structural summaries of PDB entries. *Protein Sci.* **27**, 129–134. <https://doi.org/10.1002/pro.3289>.
100. Pandey, S., Li, X.X., Srivastava, A., Baidya, M., Kumari, P., Dwivedi, H., Chaturvedi, M., Ghosh, E., Woodruff, T.M., and Shukla, A.K. (2019). Partial ligand-receptor engagement yields functional bias at the human complement receptor, C5aR1. *J. Biol. Chem.* **294**, 9416–9429. <https://doi.org/10.1074/jbc.RA119.007485>.
101. Baidya, M., Chaturvedi, M., Dwivedi-Agnihotri, H., Ranjan, A., Devost, D., Namkung, Y., Stepniwski, T.M., Pandey, S., Baruah, M., Panigrahi, B., et al. (2022). Allosteric modulation of GPCR-induced beta-arrestin trafficking and signaling by a synthetic intrabody. *Nat. Commun.* **13**, 4634. <https://doi.org/10.1038/s41467-022-32386-x>.
102. Saha, S., Ranjan, A., Godara, M., and Shukla, A.K. (2022). In-cellulo chemical cross-linking to visualize protein-protein interactions. *Methods Cell Biol.* **169**, 295–307. <https://doi.org/10.1016/bs.mcb.2021.12.024>.
103. Dogra, S., Sona, C., Kumar, A., and Yadav, P.N. (2016). Tango assay for ligand-induced GPCR-beta-arrestin2 interaction: Application in drug discovery. *Methods Cell Biol.* **132**, 233–254. <https://doi.org/10.1016/bs.mcb.2015.11.001>.
104. Kroeze, W.K., Sassano, M.F., Huang, X.P., Lansu, K., McCorvy, J.D., Guigère, P.M., Sciaky, N., and Roth, B.L. (2015). PRESTO-Tango as an open-source resource for interrogation of the druggable human GPCRome. *Nat. Struct. Mol. Biol.* **22**, 362–369. <https://doi.org/10.1038/nsmb.3014>.
105. Pandey, S., Roy, D., and Shukla, A.K. (2019). Measuring surface expression and endocytosis of GPCRs using whole-cell ELISA. *Methods Cell Biol.* **149**, 131–140. <https://doi.org/10.1016/bs.mcb.2018.09.014>.
106. Wiśniewski, J.R., Zougman, A., Nagaraj, N., and Mann, M. (2009). Universal sample preparation method for proteome analysis. *Nat. Methods* **6**, 359–362. <https://doi.org/10.1038/nmeth.1322>.
107. Ghosh, E., Dwivedi, H., Baidya, M., Srivastava, A., Kumari, P., Stepniwski, T., Kim, H.R., Lee, M.H., van Gastel, J., Chaturvedi, M., et al. (2019). Conformational Sensors and Domain Swapping Reveal Structural and Functional Differences between beta-Arrestin Isoforms. *Cell Rep.* **28**, 3287–3299.e6. <https://doi.org/10.1016/j.celrep.2019.08.053>.
108. Shirsha Saha, F.K.S., Sharma, S., Ganguly, M., Saha, S., Akasaka, H., Kobayashi, T., Zaidi, N., Mishra, S., Dalal, A., et al. (2024). Molecular basis of ligand promiscuity, structural mimicry, and atypical dimerization in the chemokine receptors. Preprint at bioRxiv. <https://doi.org/10.1101/2024.02.01.578380>.
109. Yadav, M.K., Sarma, P., Maharana, J., Ganguly, M., Mishra, S., Zaidi, N., Dalal, A., Singh, V., Saha, S., Mahajan, G., et al. (2024). Structure-guided engineering of biased-agonism in the human niacin receptor via single amino acid substitution. *Nat. Commun.* **15**, 1939. <https://doi.org/10.1038/s41467-024-46239-2>.

110. Maharana, J., Sano, F.K., Sarma, P., Yadav, M.K., Duan, L., Stepniwski, T.M., Chaturvedi, M., Ranjan, A., Singh, V., Saha, S., et al. (2024). Molecular insights into atypical modes of beta-arrestin interaction with seven transmembrane receptors. *Science* 383, 101–108. <https://doi.org/10.1126/science.adj3347>.
111. Maharana, J., Sarma, P., Yadav, M.K., Saha, S., Singh, V., Saha, S., Chami, M., Banerjee, R., and Shukla, A.K. (2023). Structural snapshots uncover a key phosphorylation motif in GPCRs driving beta-arrestin activation. *Mol. Cell* 83, 2091–2107.e7. <https://doi.org/10.1016/j.molcel.2023.04.025>.
112. Jumper, J., Evans, R., Pritzel, A., Green, T., Figurnov, M., Ronneberger, O., Tunyasuvunakool, K., Bates, R., Židek, A., Potapenko, A., et al. (2021). Highly accurate protein structure prediction with AlphaFold. *Nature* 596, 583–589. <https://doi.org/10.1038/s41586-021-03819-2>.
113. Couñago, R.M., Knapp, K.M., Nakatani, Y., Fleming, S.B., Corbett, M., Wise, L.M., Mercer, A.A., and Krause, K.L. (2015). Structures of Orf Virus Chemokine Binding Protein in Complex with Host Chemokines Reveal Clues to Broad Binding Specificity. *Structure* 23, 1199–1213. <https://doi.org/10.1016/j.str.2015.04.023>.
114. Chen, V.B., Arendall, W.B., 3rd, Headd, J.J., Keedy, D.A., Immormino, R.M., Kapral, G.J., Murray, L.W., Richardson, J.S., and Richardson, D.C. (2010). MolProbity: all-atom structure validation for macromolecular crystallography. *Acta Crystallogr. D Biol. Crystallogr.* 66, 12–21. <https://doi.org/10.1107/S0907444909042073>.

STAR★METHODS

KEY RESOURCES TABLE

REAGENT or RESOURCE	SOURCE	IDENTIFIER
Antibodies		
Monoclonal ANTI-FLAG M2-HRP antibody	Sigma-Aldrich	Cat# A8592; RRID: AB_439702
Polyclonal anti-HA antibody	Santa-Cruz	Cat# sc-805; RRID: AB_631618
Polyclonal anti-Rabbit IgG-HRP antibody	Genscript	Cat# A00098; RRID: AB_1968815
Bacterial and virus strains		
<i>E. coli</i> strain BL21(DE3)	New England Biolabs	Cat# C2527H
<i>E. coli</i> strain Rosetta (DE3)	Sigma-Aldrich	Cat# 70954
Chemicals, peptides, and recombinant proteins		
TRIS	SRL	Cat# 71033
HEPES	SRL	Cat# 63732
NaCl	SRL	Cat# 41721
EDTA	SRL	Cat# 12070
Phenylmethanesulfonyl Fluoride (PMSF)	SRL	Cat# 84375
L-Cysteine Hydrochloride Monohydrate	Sigma Aldrich	Cat# C7880
Iodoacetamide	Sigma Aldrich	Cat# I1149
Imidazole	Sigma Aldrich	Cat# I202-500G
Benzamidine Hydrochloride	SRL	Cat# 93014 (0248255)
Lysozyme	SRL	Cat# 45822
Glycerol	SRL	Cat# 77453
Lauryl Maltose Neopentyl Glycol (L-MNG)	Anatrace	Cat# NG310, CAS no.1257852-96-2
Cholesteryl Hemisuccinate (CHS)	Sigma Aldrich	Cat# C6512
Paraformaldehyde (PFA)	Sigma Aldrich	Cat# P6148, CAS no. 30525-89-4
Poly-D-lysine	Sigma Aldrich	Cat# P0899
TMB (Tetramethylbenzidine)	Thermo Fisher Scientific	Cat# 34028
Janus Green B	Sigma Aldrich	Cat# 201677
PEI (Polyethylenimine)	Polysciences	Cat# 23966
Bovine Serum Albumin, BSA	SRL	Cat# 83803 (0140105)
FLAG peptide	GenScript	N/A
HBSS - Hank's Balanced Salt Solution	Thermo Fisher Scientific	Cat# 14065
GIBCO Fetal Bovine Serum	Thermo Fisher Scientific	Cat# 10270-106
DMEM	Cellclone	Cat# CC3004
Phosphate-buffered saline (PBS)	Sigma Aldrich	Cat# D1283
GIBCO Penicillin-Streptomycin	Thermo Fisher Scientific	Cat# 15140122
ESF921 Insect Cell Culture Medium	Expression Systems	Cat#96-001-01
Coelenterazine	Goldbio	Cat# CZ05
D-Luciferin Sodium Salt	Goldbio	Cat# LUCNA-1G
Coomassie Brilliant Blue	SRL	Cat# 64222
Uranyl formate	Polysciences	Cat# 24762-1
Recombinant human CCL7	Purified	N/A
Recombinant human CCL2	PeproTech	Cat# 300-04
Recombinant human CCL5	PeproTech	Cat# 300-06
Recombinant human CCL13	PeproTech	Cat# 300-24
Recombinant human CXCL5	PeproTech	Cat# 300-22
Recombinant human CXCL8	PeproTech	Cat# 200-08
Recombinant human CXCL12	PeproTech	Cat# 300-28A

(Continued on next page)

Continued

REAGENT or RESOURCE	SOURCE	IDENTIFIER
Formvar/carbon coated 300 mesh copper grids	PELCO (Ted Pella)	Cat# 01753-F
Critical commercial assays		
Site Directed Mutagenesis Kit	NEB	Cat# E0554
NanoBiT assay	Promega	N/A
GloSensor assay	Promega	N/A
NanoBiT assay	Promega	N/A
Deposited data		
CCL7-Nb52-DARC complex	This study	PDB:8JPS, EMD-36488, EMD-37212, EMD-37214
Cryo-EM structure of the CCL2 bound CCR2-Gi complex	Shao et al. ⁵⁵	PDB: 7XA3
Cryo-EM structure of human ACKR3 in complex with CXCL12, a small molecule partial agonist CCX662, an extracellular Fab, and an intracellular Fab	Yen et al. ⁶¹	PDB: 7SK8
Cryo-EM structure of the CCL15(26-92) bound CCR1-Gi complex	Shao et al. ⁵⁹	PDB: 7VL9
Structural basis of the activation of the CC chemokine receptor 5 by a chemokine agonist	Isaikina et al. ⁵⁶	PDB: 7O7F
Cryo-EM structure of the human chemokine receptor CCR6 in complex with CCL20 and a Go protein	Wasilko et al. ⁶⁰	PDB: 6WWZ
Cryo-EM structure of a class A GPCR monomer	Liu et al. ⁵⁷	PDB: 6LFO
Cryo-EM structure of the human chemokine receptor CX3CR1 in complex with CX3CL1 and Gi1	Lu et al. ⁵⁸	PDB: 7XBX
Crystal structure of CCR2A in complex with MK-0812	Apel et al. ⁶³	PDB: 6GPS
Crystal structure of the beta2 adrenergic receptor-Gs protein complex	Rasmussen et al. ⁷⁷	PDB: 3SN6
Structure of a GPCR-G protein in complex with a natural peptide agonist	Yadav et al. ⁶⁸	PDB: 8HQC
Luteinizing hormone/choriogonadotropin receptor(S277I)-chorionic gonadotropin-Gs complex	Duan et al. ⁷⁶	PDB: 7FIG
DHA-bound FFAR4 in complex with Gs	Yin et al. ⁸¹	PDB: 8H4I
MT1-remalteon-Gi complex	Wang et al. ⁷⁹	PDB: 7VGZ
Cryo-EM structure of the human adenosine A1 receptor-Gi2-protein complex bound to its endogenous agonist	Draper-Joyce et al. ⁷⁵	PDB: 6D9H
Cryo-EM Structure of Human Niacin Receptor HCA2-Gi protein complex	Yang et al. ⁸⁰	PDB: 7XK2
Crystal structure of the rhodopsin-mini-Go complex	Tsai et al. ⁷⁸	PDB: 6FUF
Human olfactory receptor OR51E2 bound to propionate in complex with miniGs399	Billesbolle et al. ⁷⁴	PDB: 8F76
Structure of C5a bound human C5aR1 in complex with Go (Composite map)	Yadav et al. ⁶⁸	PDB: 8IA2
Cryo-EM structure of NTSR1-GRK2-Galpha(q) complexes 1	Duan et al. ⁷²	PDB: 8JPB

(Continued on next page)

Continued

REAGENT or RESOURCE	SOURCE	IDENTIFIER
Phosphorylated turkey beta1 adrenoceptor with bound agonist formoterol coupled to arrestin-2 in lipid nanodisc.	Lee et al. ⁷³	PDB: 6TKO
AVP-V2R-Galphas-beta1-gamma2-Nb35 (L state)	Bous et al. ⁶⁷	PDB: 7BB6
Cryo-EM structure of the 5HT2C receptor (INI isoform) bound to lorcaserin	Gumpper et al. ⁷⁰	PDB: 8DPF
Lodoxamide-bound GPR35 in complex with G13	Duan et al. ⁶⁹	PDB: 8H8J
The chemokine binding protein of orf virus complexed with CCL7	Zivanov et al. ⁸⁶	PDB: 4ZKC
Phosphoproteomics data	This study	ProteomeXchange Consortium, Accession code: PXD044876
Interactome data	This study	ProteomeXchange Consortium, Accession code: PXD051602
Gel images, Confocal images and Functional assay data	This study	Mendeley Data https://doi.org/10.17632/gycdr3vk4j.1

Experimental models: Cell lines

Human: HEK293	ATCC	Cat# CRL-3216
HEK293 DARC stable cell line	This study	N/A
<i>Spodoptera frugiperda</i> (Sf9) Cell line	Expression Systems	Cat# 94-001F

Oligonucleotides

DARC cloning in pCAGGS vector_Forward: GGGGTACCGAGGAGATCTGCCACC ATG GGGGAACGATCATC	This study	N/A
DARC cloning in pCAGGS vector_Reverse: TCCCCGGGGGATTGCTTCCAAGGGTGTCCAG	This study	N/A
DARC cloning in TANGO vector_Forward: CGCGGATCCGCCCTCTCTGGGTATGTCCTCCAG	This study	N/A
DARC cloning in TANGO vector_Reverse: CCGGAATTCGGATTGCTTCCAAGGGTGTCCAG	This study	N/A
DARC-V2 truncations Forward primer: CGGGATCCATGGGGAAGACGATCATCGCC	This study	N/A
DARC (1-317)-V2 cloning Reverse primer: CCGGTACCGGGCAAGAGGGTGC GGG	This study	N/A
DARC (1-321)-V2 cloning Reverse primer: CCGGTACCGAGGGGCAGAGAGGGC	This study	N/A
DARC (1-326)-V2 cloning Reverse primer: CCGGTACCAGACCATCCTTCAGGGAG	This study	N/A
DARC (1-331)-V2 cloning Reverse primer: CCGGTACCGGTGTCCAGATGAGAAGACC	This study	N/A

Recombinant DNA

pcDNA3.1_DARC	This study	N/A
pcDNA3.1_D6	Dr. Arun K Shukla, ³⁹ IIT Kanpur	N/A
pcDNA3.1_DARC (1-317)-V2	This study	N/A
pcDNA3.1_DARC (1-321)-V2	This study	N/A
pcDNA3.1_DARC (1-326)-V2	This study	N/A
pcDNA3.1_DARC (1-331)-V2	This study	N/A
TANGO_DARC	This study	N/A
pCAGGS_LgBiT-βarr1	Dr. Asuka Inoue, Tohoku University ⁸⁷	N/A
pCAGGS_LgBiT-βarr2	Dr. Asuka Inoue, Tohoku University ⁸⁷	N/A
pCAGGS_CCR1-SmBiT	This study	N/A
pCAGGS_DARC-cSmBiT	This study	N/A

(Continued on next page)

Continued

REAGENT or RESOURCE	SOURCE	IDENTIFIER
pCMV-AC6_βarr1	Dr. Arun K Shukla, ³⁹ IIT Kanpur	N/A
pCMV-AC6_βarr2	Dr. Arun K Shukla, ³⁹ IIT Kanpur	N/A
pcDNA_βarr1-mYFP	Addgene	Plasmid #36916
pcDNA_βarr2-mYFP	Addgene	Plasmid #36917
pVL1393-FLAG-M4-DARC	GenScript	N/A
pVL1393-FLAG-T4L-DARC	GenScript	N/A
pGEMEX-1-CCL7	Dr. Arun K Shukla, ⁸⁸ IIT Kanpur	N/A

Software and algorithms

Relion3.1.2, Relion3.1.3, Relion 4.0 and Relion 5.0-beta	Zivanov et al. ⁸⁶ Zivanov et al. ⁸⁹ ; Zivanov et al. ⁹⁰	https://www3.mrc-lmb.cam.ac.uk/relion/index.php?title=Main_Page
cryoSPARC	Punjani et al. ⁹¹	https://cryosparc.com/
UCSF Chimera X	Pettersen et al. ⁹²	https://www.rbvi.ucsf.edu/chimerax/
UCSF Chimera	Pettersen et al. ⁹³	https://www.cgl.ucsf.edu/chimera/
COOT	Emsley et al. ⁹⁴ ; Emsley and Cowtan ⁹⁵	https://www2.mrc-lmb.cam.ac.uk/personal/pemsley/coot/
Phenix	Liebschner et al. ⁹⁶ ; Adams et al. ⁹⁷	https://phenix-online.org/
PDBePISA webserver	Krissinel and Henrick ⁹⁸	https://www.ebi.ac.uk/pdbe/pisa/
PDBsum	Laskowski et al. ⁹⁹	http://www.ebi.ac.uk/thornton-srv/databases/pdbsum/
Graphpad Prism 9	GraphPad Software, San Diego, California USA	https://www.graphpad.com/scientific-software/prism/
Zen lite, Zeiss	Zeiss	https://www.zeiss.com/microscopy/int/products/microscope-software/zen-lite.html

Others

100kDa Cutoff Concentrators	Cytiva	Code# 28932319
10kDa Cutoff Concentrators	Cytiva	Code# 28932296

RESOURCE AVAILABILITY

Lead contact

Further information and requests for reagents should be addressed to the lead contact, Dr. Arun K. Shukla (arshukla@iitk.ac.in).

Materials availability

All reagents described in this manuscript are available upon request from the [lead contact](#) with appropriate Materials Transfer Agreement.

Data and code availability

- All three-dimensional cryo-EM density maps, coordinates for the atomic models and local-refined maps generated in this study have been deposited and are publicly available as of the date of publication. Accession numbers (EMDB, PDB IDs and PXD id) are listed in the [key resources table](#). Original gel images, blots and confocal images have been deposited to Mendeley data, and they are publicly available after publication. The DOI is listed in the [key resources table](#).
- This paper does not report any original code.
- Any additional information required to reanalyze the data reported in this paper is available from the [lead contact](#) upon request.

EXPERIMENTAL MODEL AND SUBJECT DETAILS

Human cell lines

HEK-293 cells were purchased from ATCC for all the cellular experiments performed in the study. The cell line was examined frequently under the microscope for proper morphology, but they were not authenticated. They were cultured in DMEM with fetal

bovine serum (FBS) at 37°C in 5% CO₂. In this study, any knockout or knockdown cell lines were not generated, and the details of stably-transfected HEK-293 cells expressing recombinant DARC are included in the [key resources table](#). In addition, previously generated cell lines are referenced in the manuscript.

Insect cells

Sf9 cells were obtained from Expression systems, and they were routinely monitored under the microscope for proper morphology. These cells were maintained in a shaker incubator at 27°C with 135rpm shaking, and sub-cultured in protein-free insect cell medium purchased from Expression Systems.

METHOD DETAILS

General reagents, plasmids, and cell culture

Most of the general reagents were purchased from Sigma Aldrich unless otherwise mentioned. Dulbecco's Modified Eagle's Medium (DMEM), Trypsin-EDTA, Fetal-Bovine Serum (FBS), Phosphate buffer saline (PBS), Hank's balanced salt solution (HBSS), and Penicillin-Streptomycin solution were purchased from Thermo Fisher Scientific. HEK-293T cells (ATCC) were maintained in DMEM (Gibco, Cat. no: 12800-017) supplemented with 10% (v/v) FBS (Gibco, Cat. no: 10270-106) and 100U mL⁻¹ penicillin and 100μg mL⁻¹ streptomycin (Gibco, Cat. no: 15140122) at 37°C under 5% CO₂. Sf9 cells were obtained from Expression Systems and maintained in protein-free cell culture media purchased from Expression Systems (Cat. no: 96-001-01) at 27°C with 135 rpm shaking. The cDNA coding region of DARC was cloned in pcDNA3.1 vector with an N-terminal FLAG tag and in pVL1393 vector with an N-terminal FLAG tag followed by the N-terminal region of M4 receptor (residue no. 2-23). All other receptor pcDNA3.1 constructs were also cloned with an N-terminal FLAG tag. The cDNA coding region of Nb52 was synthesized from Genscript, based on previously described sequence⁵³ with an additional C-terminal 6X-His tag and cloned in pET22b(+) vector. All DNA constructs were verified by sequencing from Macrogen. For HDX-MS, a truncated version of DARC was used (27-322), cloned in pVL1393 vector with an N-terminal FLAG tag, followed by T4 lysozyme (T4L) and 3C protease cleavage site. Recombinant human C5a was purified from *E. coli* as described previously.¹⁰⁰ For the NanoBiT-G protein-dissociation assay and the flow cytometry-based expression analysis, the full-length human CCR1 or DARC was inserted into the pCAGGS expression vector with an N-terminal fusion of the hemagglutinin-derived signal sequence (ssHA), FLAG epitope tag and a flexible linker (MGKTIIALSYIFCLVFADYKDDDDKGGSGGG GSGGSSSGGG; the FLAG epitope tag is underlined), and the corresponding constructs were named as ssHA-FLAG-CCR1 and ssHA-FLAG-DARC, respectively. For the NanoBiT-β-arrestin-recruitment assay and the GRK-recruitment assay, ssHA-FLAG-CCR1 and ssHA-FLAG-DARC were C-terminally fused with the flexible linker and the SmBiT fragment GSGGGGGSGGSSS GGVTGYRLFEEIL; the SmBiT is underlined). The resulting plasmid was named as ssHA-FLAG-CCR1-SmBiT and ssHA-FLAG-DARC-SmBiT, respectively. Constructs of the NanoBiT-G protein sensors, the NanoBiT-β-arrestin sensors and the NanoBiT-GRK sensors were described previously.^{41,87}

Second messenger signaling assays

To measure the effect of ligand stimulation on Gs and Gi-mediated signaling, intracellular cAMP levels were measured using the GloSensor assay, as previously described.³⁹ In brief, HEK-293T cells were transfected with either 3.5μg of FLAG-tagged DARC/V₂R or 2.5μg of FLAG-tagged C5aR1 (encoded in pcDNA vector) and 3.5μg of F22 plasmid (Promega, Cat. no: E2301). 14-16 h following transfection, cells were trypsinized and seeded in 96-well plates at a density of 100,000 cells per well in assay buffer (20mM HEPES pH 7.4, 1X HBSS and 0.5mg mL⁻¹ D-luciferin (GoldBio, Cat. no: LUCNA-1G)) and incubated for 1 h 30 min at 37°C followed by an additional 30 min at room temperature. Basal luminescence was measured for 5 cycles. For measuring Gi-mediated decrease in cytosolic cAMP levels, 5μM forskolin was added to the wells and luminescence was measured for 8 cycles till the reading stabilized. This was followed by addition of ligand at the indicated final concentration. Luminescence was recorded for 30 cycles. Signal obtained was normalized either with respect to reading observed for positive control at the highest concentration of ligand (for measuring Gs-mediated increase in intracellular cAMP levels) or with signal observed at the lowest concentration of ligand for each receptor (for measuring Gi-mediated decrease in intracellular cAMP levels), treated as 100%.

Calcium flux assay was undertaken to measure ligand induced changes in cytosolic Ca²⁺ levels, as previously described.⁴⁰ Briefly, HEK-293T cells were transfected with 4μg of pGP-CMV-GcAMP6s (Ca²⁺ sensor plasmid; Addgene, Cat. no: 40753) and either 4μg of 5HT_{2c} receptor (as positive control) or 4μg of DARC using PEI max in a ratio of 1:4 (DNA:PEI max). Transfected cells were seeded in a black optical bottom plate at a density of 50,000 cells per well in complete medium (supplemented with 10% FBS). 14-16 h post-transfection, media from the wells was replaced with 100μL of Ca²⁺/Mg²⁺ free HBSS buffer (pH 7.2) and the cells were incubated for an additional 10 min at 37°C in Flex Station 3 (Molecular Devices). Ligand induced changes in the relative fluorescence unit (RFU) was measured at an excitation wavelength of 485nm and emission wavelength of 525nm (cut off 515nm) with a setting of 6 reads per well. Basal fluorescence was recorded for 15 sec for each well, followed by addition of 20μL of 6X concentration of ligand using robotic pipetting of FlexStation system. RFU was recorded at an interval of 2 sec for a total duration of 135 sec. The change in RFU (ΔRFU) for each group was calculated by subtracting the average basal response (RFU before ligand addition) from RFU of each well at each time point following ligand addition. ΔRFU was plotted and analyzed using GraphPad Prism 9 software.

NanoBiT-based G protein dissociation assay

Ligand-induced G protein activation was measured using a previously described NanoBiT-based G protein dissociation assay.⁴¹ Briefly, a NanoBiT-G protein consisting of LgBiT-tagged $G\alpha$ subunit and SmBiT-tagged $G\gamma 2$ subunit along with the untagged $G\beta 1$ subunit were co-expressed with the indicated receptor constructs and ligand-induced change in luminescence signal was measured. Typically, HEK-293 cells (Thermo Fisher Scientific) were seeded in a 6-well culture plate and transfected with a plasmid mixture consisting of 100ng LgBiT- $G\alpha$ ($G\alpha s$, $G\alpha i1$, $G\alpha i2$, $G\alpha i3$, $G\alpha o$, $G\alpha q$, $G\alpha 12$ or $G\alpha 13$), 500ng $G\beta 1$, 500ng SmBiT- $G\gamma 2$ (C68S) with 200ng receptor plasmid (ssHA-FLAG-CCR1, ssHA-FLAG-DARC or an empty plasmid). To enhance NanoBiT-G protein expression for Gs , Gq and $G12/13$, 100ng of RIC8B plasmid (isoform 2; for Gs) or RIC8A (isoform 2; for Gq , $G12$, and $G13$) were co-transfected. After 24 h of transfection, the cells were harvested with EDTA-containing PBS, centrifuged, and suspended in 2mL of Hank's Balanced Salt Solution (HBSS) containing 0.01% bovine serum albumin (BSA fatty acid-free grade, SERVA) and 5mM 4-(2-hydroxyethyl)-1-piperazineethanesulfonic acid (HEPES) at pH 7.4 (assay buffer). Afterwards, the cells were dispensed in a white 96-well plate (80 μ L per well), incubated with 20 μ L of 50 μ M coelenterazine (Carbosynth, Cat. no: EC175526), and 2 h later, baseline luminescence was measured (SpectraMax L, Molecular Devices). Subsequently, 20 μ L of 6X CCL7, serially diluted in the assay buffer, was manually added and the plate was immediately read for the second measurement in kinetic mode. Luminescence counts recorded from 5 to 10 min post-agonist addition were averaged, corrected with the baseline signal, normalized with respect to vehicle control and plotted using the GraphPad Prism 9 software.

Bioluminescence Resonance Energy Transfer (BRET)-based GRK recruitment assay

HEK-293 clonal cell line (HEK-293SL cells), referred to as HEK-293 cells, were a gift from Stephane Laporte (McGill University Montreal, Quebec, Canada). These cells were cultured in Dulbecco's Modified Eagle's Medium (DMEM) high glucose (Gibco) supplemented with 10% fetal bovine serum and 100units mL⁻¹ penicillin-streptomycin (Gibco), maintained at 37°C and 5% CO₂ and passaged every 3-4 days using trypsin-EDTA 0.05% (Gibco) to detach the cells. DNA to be transfected was combined with salmon sperm DNA (Invitrogen) to obtain a total of 1.6 μ g DNA per condition. Increasing amounts of GFP10-GRK (0 to 800ng) was transfected along with 100ng of $G\beta 1$, 100ng of $G\gamma 2$ and 50ng of DARC-RlucII. Linear polyethyleneimine 25K (PEI; Polysciences) was combined with DNA (4.8 μ g PEI per 1.6 μ g of DNA), vortexed and incubated for 20 min before adding 1.2mL of cell suspension containing 360,000 cells for each condition. Cells containing the DNA were seeded (100 μ L per well) in white 96-well plates (Greiner) and incubated for 48 h before assay. The day of the assay, cells were washed with DPBS (Gibco) and assayed in Tyrode's buffer (137mM NaCl, 0.9mM KCl, 1mM MgCl₂, 11.9mM NaHCO₃, 3.6mM NaH₂PO₄, 25mM HEPES, 5.5mM glucose, 1mM CaCl₂ (pH 7.4)) at 37°C. The expression of GFP10 was monitored in each well using a FLUOstar Omega microplate reader (BMG Labtech) by exciting at 400nm and reading the fluorescence at 520nm. CCL7 100nM final or vehicle were added and cells were incubated at 37°C for 30 min. 5 min before reading, 2.5 μ M of the Renilla luciferase substrate (coelenterazine 400a; NanoLight Technology) was added. BRET measurements were performed using the FLUOstar Omega microplate reader with an acceptor filter (515 \pm 30nm) and donor filter (410 \pm 80nm). BRET was calculated by dividing GFP10 emission by RlucII emission.

NanoBiT-based β -arrestin/GRK recruitment assay

Ligand-induced recruitment of β -arrestin or GRK was performed as described previously with minor modifications.⁸⁷ Transfection was performed according to the same procedure as described in the "NanoBiT-based G protein dissociation assay" section except for a plasmid mixture consisting of 500ng ssHA-FLAG-GPCR-SmBiT and 100ng LgBiT- β -arrestin (β -arrestin assay) or 500ng ssHA-FLAG-GPCR-SmBiT and 500ng GRK-LgBiT (GRK assay). The transfected cells were dispensed into a 96-well plate, and ligand-induced luminescent changes were measured following the same procedures as described for the NanoBiT-based G protein-dissociation coupling assay.

Confocal microscopy to visualize β -arrestin1/2 trafficking

To visualize β -arrestin recruitment to the cell membrane and subsequent endocytosis, confocal microscopy was performed as described earlier.¹⁰¹ HEK-293 cells transfected with 3.5 μ g of FLAG-tagged receptor and 3.5 μ g of YFP-tagged β -arrestin1/2 were seeded in confocal dishes (pre-coated with 0.01% poly-D-Lysine) at a density of 1 million cells dish⁻¹, 24 h post-transfection. Cells were allowed to adhere to the confocal dishes, and 24 h post-seeding, cells were serum-starved for 6 h. Confocal imaging of all samples was done using Zeiss LSM 710 NLO confocal microscope wherein samples were housed on a motorized XY stage with a CO₂ enclosure and a temperature-controlled platform equipped with 32x array GaAsP descanned detector (Zeiss). A multi-line argon laser source was used for the green channel (mYFP). All microscopic settings including pinhole opening and laser intensity were kept in the same range for a parallel set of experiments. Cells were stimulated with 100nM CCL7 for indicated time duration. Images were scanned in line scan mode and acquired images were processed post imaging in ZEN lite (ZEN-blue/ZEN-black) software suite from ZEISS.

Co-immunoprecipitation to detect physical interaction between DARC and β -arrestin1/2

Co-immunoprecipitation (coIP) was performed to measure the physical coupling between DARC and β -arrestin1/2, as described earlier.¹⁰² In brief, HEK-293T cells transfected with 3.5 μ g of FLAG-tagged receptor and either 1.7 μ g of β -arrestin1 or 3.5 μ g of β -arrestin2 were harvested 48 h post-transfection. Prior to harvesting, cells were serum starved for 6 h and stimulated with 100nM

of CCL7. The pellets were dounced in buffer containing 20mM HEPES pH 7.4, 150mM NaCl, 1X PhosSTOP (Sigma, Cat. no: 4906845001) and 1X cComplete protease inhibitor cocktail (Sigma, Cat. no: 4693116001), and incubated with 1.5mM freshly prepared DSP (Sigma, Cat. no: D3669) for 45 min at room temperature under tumbling conditions. This was followed by solubilization, wherein the suspension was incubated with 0.1% L-MNG for 1 h at room temperature under tumbling conditions. Cell debris was removed by centrifugation, and the supernatant was incubated with pre-equilibrated anti-FLAG M1 beads for 1 h 30 min, in the presence of 2mM CaCl₂, at room temperature. Beads were washed five times alternatively with low salt buffer (20mM HEPES pH 7.4, 150mM NaCl, 2mM CaCl₂, 0.01% L-MNG) and high salt buffer (20mM HEPES pH 7.4, 350mM NaCl, 2mM CaCl₂, 0.01% L-MNG). Elution was collected by incubating the beads with elution buffer (20mM HEPES pH 7.4, 150mM NaCl, 2mM EDTA, 0.01% L-MNG, 250μg/μL FLAG) for 30 min. Eluted samples were run on a SDS-PAGE followed by western blotting. The blots were blocked with 1% BSA for 1 h at room temperature, followed by incubation with rabbit anti-βarr antibody (1:2500; CST, Cat. no: 4674) overnight at 4°C. The next day, the blots were washed thrice with 1X TBST (10 min each wash) and then incubated with anti-rabbit secondary antibody (1:10,000; Genscript, Cat. no: A00098) for 1 h at room temperature. The blots were once again washed three times with 1X TBST (10 min each wash) and developed with Promega ECL solution on a chemidoc (BioRad). The blots were then stripped and re-probed for receptor using anti-FLAG M₂HRP (1:5000, Sigma, Cat. no: A8592). Bands were quantified using ImageLab software and normalized with respect to signal obtained at highest time point for positive control (treated as 100%). To assess whether addition of V₂-tail can promote recruitment of β-arrestin, several chimeric constructs were generated wherein the V₂-tail was added after truncating the C-terminal end of DARC to different extents. For all of these chimeric N-terminal FLAG-tagged receptor constructs, 3.5μg of DNA was transfected.

TANGO Assay to measure β-arrestin2 recruitment

To measure β-arrestin2 recruitment following ligand stimulation, TANGO assay was undertaken.^{103,104} Briefly, HTLA cells were transfected with 7μg of FLAG-tagged receptor. 24 h post-transfection, cells were trypsinized and seeded in 96-well plates at a density of 100,000 cells per well in complete media and allowed to adhere. Next day, complete media was replaced with incomplete DMEM supplemented with respective ligand at indicated dose. After 8 h, incomplete media was removed from the wells and drug buffer (20mM HEPES pH 7.4, 1X HBSS, 0.5mg/mL D-luciferin) was added. Emitted luminescence was recorded immediately. Signal was normalized with respect to reading observed for positive control at the highest concentration dose, treated as 100%.

Receptor surface expression assay

To assess cell surface expression of the corresponding receptors, whole cell surface ELISA was performed, as previously described.¹⁰⁵ Briefly, transfected cells were seeded at a density of 0.1 million cells per well 24 h post-transfection in 24-well plates (pre-coated with 0.01% poly-D-Lysine) and incubated for 24 h at 37°C in a CO₂ incubator. Once cells were well adhered, the media was removed by aspiration and the cells were washed once with 1X TBS. This was followed by treatment with 300μL 4% PFA for 20 min to fix the cells. Excess PFA was removed by washing the cells thrice with 400μL of 1X TBS. The wells were blocked by incubating with 200μL 1% BSA for 1 h 30 min. 200μL of anti-FLAG M₂HRP antibody (Sigma, Cat no. A8592) at a dilution of 1:10,000 was added to the wells and incubated for an additional 1 h 30 min. To develop the signal, 200μL of TMB (Thermo Scientific, Cat. no: 34028) was added to the wells and incubated till the development of adequate color. Reaction was quenched by transferring 100μL of solution to a 96-well plate containing 100μL of 1M H₂SO₄ and absorbance was measured at 450nm. To estimate the amount of cells fixed in each well, excess TMB was first removed by washing once with 400μL of 1X TBS and the cells were incubated for 20 min in 0.2% Janus green B (Sigma, Cat. no. 201677). After removing excess stain by repeated washing with MQ water, signal was developed by adding 800μL of 0.1N HCl to each well and read at 595nm. Signal was normalized by dividing the reading obtained at 450nm with the reading obtained at 595nm. Receptor surface expression was fold normalized with respect to vehicle (empty pcDNA vector) transfected cells.

For the NanoBiT-based G protein dissociation assay, surface expression of the receptors was measured using flow-cytometry based assay following a previously described protocol.³⁹ HEK-293 cells were transfected with plasmids for ssHA-FLAG-CCR1 or ssHA-FLAG-DARC along with the NanoBiT-Gi1 sensor, as described in the “[NanoBiT-based G protein-dissociation assay](#)” section. The cells were harvested with 0.5mM EDTA-containing PBS and transferred to a 96-well V-bottom plate. The cells were then fluorescently labelled using anti-FLAG monoclonal antibody (Clone 1E6, FujiFilm Wako Pure Chemicals; 10μg mL⁻¹ diluted in 2% goat serum and 2mM EDTA-containing PBS) followed by incubation with Alexa Fluor 488-conjugated goat anti-mouse IgG secondary antibody (Thermo Fisher Scientific; 10μg mL⁻¹). Subsequently, the cells were washed with PBS, resuspended in 2mM EDTA-containing PBS, filtered through a 40μm filter and the fluorescent intensity of single cells was quantified using a flow cytometer. Fluorescent signal from Alexa Fluor 488 was recorded and analyzed using the FlowJo software. Mean fluorescence intensity from about 20,000 cells per sample were used for analysis. Typically, we obtained a CCR1 MFI value of 2,000 (arbitrary unit) and a mock MFI value of 20. For each experiment, we normalized an MFI value of DARC by that of CCR1 performed in parallel and denoted relative expression levels.

Phosphoproteomics analysis

Cell lysate preparation

For mass spectrometry based phosphoproteomics analysis, HEK-293 cells stably expressing DARC were used. Cells were grown at a confluency level of 70–80% and serum starved for a minimum of 6 h prior to stimulation. This was followed by stimulation for 10 min with 100nM CCL7. Thereafter media was aspirated, and the cells were washed with 1X Tris-buffered saline (TBS). For each set, cells corresponding to twelve 10cm plates were harvested by scraping, pooled together in a 15mL falcon, and pelleted by centrifugation at 4°C. The pellets were washed once with 1X TBS to remove any trace media and transferred to 1.5mL Eppendorf tubes. Four independent sets of stimulated and unstimulated cell pellets were prepared. The pellets were then treated with 3 times volume of boiling SDS lysis buffer (5% SDS, 50mM Tris pH 8.5) and lysed by incubating on a heat bath at 95°C for 5 min. The lysate was then sonicated to facilitate the breakdown of nuclear material and reduction of viscosity of the solution. This was followed by centrifugation at 15,000 rpm for 20 min at room temperature. The supernatant was carefully transferred to fresh tubes leaving behind any insoluble debris. Protein concentration estimation was performed by BCA analysis using the same lysis buffer as blank solution and cross-checked by measuring A_{280} using a NanoDrop (Thermo Fischer Scientific). Sample corresponding to 15mg of each biological replicate was sent to V-Proteomics for mass spectrometric analysis.

Preparation of sample and phosphopeptide enrichment

For preparing sample, 1mg of the Cell-lysate was first subjected to reduction by treating with 5mM TCEP and this was followed by alkylation with 50mM iodoacetamide. Thereafter the sample was digested with trypsin at a ratio of 1:50 for trypsin: lysate for 16 h at 37°C using FASP method.¹⁰⁶ The peptide mixture was then dried using a speed vac (Eppendorf: Concentrator plus - Centrifuge Concentrator). The dried peptide pellet was dissolved in Phthalic acid buffer (0.1% phthalic acid, 2.5% TFA, 20% water, 80% acetonitrile) followed by addition of TiO_2 beads (Titansphere 5mm, GL sciences) and mixed for 2 h on a rotator. The beads were washed twice with phthalic acid buffer followed by washing with 80% acetonitrile, 0.1% TFA and finally 0.1% TFA. Bound phosphopeptides were eluted with 0.3M NH_4OH and the pH was adjusted to around 2 with 50% TFA. Finally, the enriched phosphopeptides were dried using a speed vac and further clarification was performed using C18 mini columns.

Mass spectrometric analysis of peptide mixtures

The phosphopeptide enriched dried pellet was resuspended in Buffer A (2% acetonitrile, 0.1% formic acid). All mass spectrometric experiments were performed using an Easy-nLC-1000 system (Thermo Fisher Scientific) coupled to an Orbitrap Exploris 240 mass spectrometer (Thermo Fisher Scientific) equipped with nanoelectrospray ion source. 1 μg of the enriched phosphopeptide mixture was loaded with buffer A (2% acetonitrile, 0.1% formic acid) and resolved on Easy-spray column (2 micron resin, 50cm length) and separated with a 0–40% gradient of buffer B (80% acetonitrile, 0.1% formic acid) at a flow rate of 300nL min^{-1} and injected for MS analysis. LC gradients were run for 110 min. MS spectra were acquired in the Orbitrap Exploris 240 under the following conditions: Maximum ion injection time = 60 ms, AGC target = 300%, RF Lens = 70% at a resolution of 60,000 for a mass range of 375–1500. The peptides were dissociated using higher energy collisional dissociation (HCD) for MS/MS at a collision energy 28%. MS/MS spectra were acquired under the following conditions: Maximum ion injection time = 60 ms, AGC target = 100% at a resolution of 15,000. MS/MS data was acquired using a data-dependent top 20 method dynamically choosing the most abundant precursor ions from the survey scan, with dynamic exclusion set at 30 sec. Lock mass option was enabled for polydimethylcyclisiloxane (PCM) ions (m/z = 445.120025) for internal recalibration during the run.

Mass spectrometric data processing and statistical analysis

All eight RAW files (4 sets of unstimulated and 4 sets of stimulated) were analyzed using Proteome Discoverer v2.5 against the Uniprot Human reference proteome database (UPID: UP000005640, 20360 Protein entries). For Sequest HT and MS Amanda 2.0 search, the precursor and fragment mass tolerance were set at 10 ppm and 0.02 Da respectively. The protease used to generate peptides i.e., enzyme specificity was set for trypsin/P (cleavage at the C terminus of “K/R”: unless followed by “P”) along with maximum missed cleavage value of two. Carbamidomethylation on Cysteine was considered as static modification, while oxidation of Methionine, acetylation at N-terminus, and phosphorylation at Tyrosine, Threonine and Serine were considered as dynamic modifications for database search. Both protein false discovery rate and peptide spectrum match were set to 0.01 FDR and determined using percolator node. Relative protein quantification of the proteins was performed using Minora feature detector node of Proteome Discoverer v2.5 under default settings considering only high PSM (peptide spectrum matches) confidence.

Based on Uniprot accession number Pfam, KEGG pathways and GO annotations were assigned for the list of identified proteins. Also, for high sensitivity-phospho site localization to be detected for individual site, ptmRS node was considered. Among all the proteins detected phosphoproteins were filtered out and all the respective phosphopeptide were further analyzed based on their relative abundance values. The data matrix was imported in perseus software (version 1.6.0.7) and data was further filtered for those phosphopeptides which were present in at least 4 samples among the total 8 samples (4 sets of stimulated and 4 sets of unstimulated samples). The LFQ abundance values of these filtered peptides were log transformed and imputation was applied using default settings (width 0.3, downshift 1.8) where missing values were replaced by random numbers that are drawn from a normal distribution. Student's t test was applied between stimulated and unstimulated group samples using a p-value significance threshold level of 0.05 and the test results were represented as volcano plot. Z-score normalization was applied using median abundance values and student's t-test significant values were used for hierarchical clustering of rows and/or columns (Distance: Euclidean, Linkage: average, Preprocess: k-means, No clusters:300, Max iterations-10) in order to generate heat map.

Mass spectrometry based interactome analysis

Sample preparation

To identify proteins whose physical interaction with DARC is altered upon stimulation with CCL7, we undertook mass spectrometry based interactome analysis. For preparing samples, we performed cross-linking co-immunoprecipitation as described above with slight modifications. Briefly, HEK-293 cells stably expressing DARC were cultured to ~80% confluency in 10cm plates and serum starved for 6 h prior to harvesting. Thereafter, cells were stimulated with 100nM CCL7 for 10 min, media was aspirated, and the cells were washed once with 1X Tris-buffered saline (TBS) and harvested by scraping. Four independent biological replicates were prepared for both stimulated and unstimulated conditions. For each set, cells corresponding to ten 10cm plates were pooled together, pelleted, and washed one more time with 1X TBS. Each pellet was then resuspended in 800 μ L lysis buffer (20mM HEPES pH 7.4, 150mM NaCl, and 1X cOmplete protease inhibitor (Roche, Cat. no: 04693116001)) and homogenized by douncing. 1mM DSP, dissolved fresh in DMSO, was added to the lysate and protein cross-linking was allowed to proceed for 40 min at room temperature under tumbling conditions. Cross-linking was quenched by adding 10mM Tris pH 8.0. This was followed by the addition of 1% L-MNG and the lysate was tumbled for 1 h at room temperature to allow solubilization of the cells. The solubilized lysate was then centrifuged at 10,000 rpm for 10 min at room temperature and the supernatant was collected in separate tubes. BCA estimation was performed to quantify the supernatant and 10mg lysate was taken as input for co-immunoprecipitation for all the sets. 60 μ L pre-equilibrated M1-FLAG beads slurry (1:1 bead: buffer) was added to the lysate in presence of 2mM CaCl₂ and bead binding was allowed to proceed for another 1 h 30 min at room temperature under tumbling conditions. Non-specifically bound proteins was removed by washing the beads five times with 20mM HEPES pH 7.4, 150mM NaCl and 0.01% L-MNG. Bound protein was then eluted with FLAG elution buffer (20mM HEPES pH 7.4, 150mM NaCl, 2mM EDTA, 250 μ g/ml FLAG peptide and 0.01% L-MNG). Eluted proteins were flash frozen in presence of 10% glycerol and shipped to V-proteomics for mass spectrometric analysis.

The elution was then reduced by treating with 5mM TCEP and subsequently alkylated with 50mM iodoacetamide. Thereafter, the samples were digested with trypsin at a ratio of 1:50 for trypsin: lysate for 16 h at 37°C using FASP method. The peptide mixture was then dried using a speed vac (Eppendorf: Concentrator plus - Centrifuge Concentrator).

Mass spectrometric analysis of peptide mixtures

The phosphopeptide enriched dried pellet was resuspended in Buffer A (2% acetonitrile, 0.1% formic acid). All mass spectrometric experiments were performed using an Easy-nLC-1000 system (Thermo Fisher Scientific) coupled to an Orbitrap Exploris 240 mass spectrometer (Thermo Fisher Scientific) equipped with nanoelectrospray ion source. 1 μ g of the enriched phosphopeptide mixture was loaded with buffer A (2% acetonitrile, 0.1% formic acid) and resolved on Easy-spray column (2 micron resin, 50cm length) and separated with a 0–40% gradient of buffer B (80% acetonitrile, 0.1% formic acid) at a flow rate of 500nL min⁻¹ and injected for MS analysis. LC gradients were run for 110 min. MS spectra were acquired in the Orbitrap Exploris 240 under the following conditions: Maximum ion injection time = 60 ms, AGC target = 300%, RF Lens = 70% at a resolution of 60,000 for a mass range of 375–1500. The peptides were dissociated using higher energy collisional dissociation (HCD) for MS/MS at a collision energy 28%. MS/MS spectra were acquired under the following conditions: Maximum ion injection time = 60 ms, AGC target = 100% at a resolution of 15,000. MS/MS data was acquired using a data-dependent top 20 method dynamically choosing the most abundant precursor ions from the survey scan, with dynamic exclusion set at 30 sec. Lock mass option was enabled for polydimethylcyclodioxane (PCM) ions (m/z = 445.120025) for internal recalibration during the run.

Mass spectrometric data processing and statistical analysis

All eight RAW files (4 sets of unstimulated and 4 sets of stimulated) were analyzed using Proteome Discoverer v2.5 against the Uniprot Human reference proteome database (UPID: UP000005640, 20360 Protein entries). For Sequest HT and MS Amanda 2.0 search, the precursor and fragment mass tolerance were set at 10 ppm and 0.02 Da respectively. The protease used to generate peptides i.e., enzyme specificity was set for trypsin/P (cleavage at the C terminus of “K/R: unless followed by “P”) along with maximum missed cleavage value of two. Carbamidomethylation on Cysteine was considered as static modification, while oxidation of Methionine, acetylation at N-terminus, and phosphorylation at Tyrosine, Threonine and Serine were considered as dynamic modifications for database search. Both protein false discovery rate and peptide spectrum match were set to 0.01 FDR and determined using percolator node. Relative protein quantification of the proteins was performed using Minora feature detector node of Proteome Discoverer v2.5 under default settings considering only high PSM (peptide spectrum matches) confidence.

The complete data matrix of all the identified proteins was imported in perseus software (version 1.6.0.7) and data was further filtered for those proteins which were present in at least 3 samples from a total 4 samples in each condition. The LFQ abundance values were log transformed and imputation was applied using default settings (width 0.3, downshift 1.8) where missing values were replaced by random numbers that are drawn from a normal distribution. Student's t test was applied between stimulated and unstimulated group samples using a p-value significance threshold level of 0.05 and the test results were represented as volcano plot. Z-score normalization was applied using median abundance values and student's t-test significant values were used for hierarchical clustering of rows and/or columns (Distance: Euclidean, Linkage: average, Preprocess: k-means, No clusters:300, Max iterations-10) in order to generate heat map.

STRING analysis and DARC-CD82 interaction

STRING analysis of DARC identified CD82 as a potential interacting partner. In order to validate the physical interaction between DARC and CD82, we performed co-immunoprecipitation experiment. For measuring basal state interaction between the two

proteins, HEK-293T cells were transfected either with a mixture of 3.5 μ g DARC (bearing an N-terminal FLAG tag) and 3.5 μ g CD82 (bearing a C-terminal HA tag) or 3.5 μ g DARC (bearing an N-terminal FLAG tag) and 3.5 μ g pcDNA or 3.5 μ g CD82 (bearing a C-terminal HA tag) and 3.5 μ g pcDNA. For measuring the effect of CCL7 stimulation on their interaction, cells were co-transfected with 3.5 μ g DARC (bearing an N-terminal FLAG tag) and 3.5 μ g CD82 (bearing a C-terminal HA tag). 48 h post transfection, cells were serum starved for 6 h, stimulated with 100nM CCL7 for the indicated time durations and harvested by scraping. Pellets were resuspended in 100 μ L lysis buffer (20mM HEPES pH 7.4, 150mM NaCl, 1mM PMSF, 2mM benzamidine) and homogenized by douncing. For preparing crosslinked samples, 2mM freshly dissolved DSP was added to each dounced pellet and crosslinking was allowed to proceed for 40 min at room temperature under tumbling conditions. The reaction was then quenched by adding 10mM Tris-Cl pH 8.0. The preceding step was omitted when preparing non-crosslinked samples. This was followed by the addition of 1% L-MNG and solubilization was allowed to proceed for 1 h at room temperature under tumbling condition. Cell debris was removed by centrifugation, and the supernatant was incubated with pre-equilibrated anti-FLAG M1 beads for 1 h 30 min, in the presence of 2mM CaCl₂, at room temperature. Beads were washed five times alternatively with low salt buffer (20mM HEPES pH 7.4, 150mM NaCl, 2mM CaCl₂, 0.01% L-MNG) and high salt buffer (20mM HEPES pH 7.4, 350mM NaCl, 2mM CaCl₂, 0.01% L-MNG). Elution was collected by incubating the beads with elution buffer (20mM HEPES pH 7.4, 150mM NaCl, 2mM EDTA, 0.01% L-MNG, 250 μ g/ μ L FLAG) for 30 min. Eluted samples were run on SDS-PAGE followed by western blotting. The blots were blocked with 1% BSA for 1 h at room temperature, followed by incubation with rabbit anti-HA antibody (1:2500; SantaCruz, Cat. no: sc-805) overnight at 4°C. The next day, the blots were washed thrice with 1X TBST (10 min each wash) and then incubated with anti-rabbit secondary antibody (1:10,000; Genscript, Cat. no: A00098) for 1 h at room temperature. The blots were once again washed three times with 1X TBST (10 min each wash) and developed with Promega ECL solution on a chemidoc (BioRad). The blots were then stripped and re-probed for receptor using anti-FLAG M₂HRP (1:5000, Sigma, Cat/ no: A8592). Bands were quantified using ImageJ software for the experiment wherein the effect of CCL7 stimulation was measured, and normalized with respect to signal obtained at unstimulated condition (treated as 1).

Purification of DARC

Full-length recombinant DARC was purified from *Spodoptera frugiperda* (Sf9) insect cells as previously described for other GPCRs.^{39,107–110} Briefly, Sf9 cells infected with DARC expressing baculovirus were harvested 72 h post-infection. Cells were first homogenized in hypotonic buffer (20mM HEPES pH 7.4, 20mM KCl, 10mM MgCl₂, 1mM PMSF, 2mM benzamidine) followed by hypertonic buffer (20mM HEPES pH 7.4, 20mM KCl, 10mM MgCl₂, 1M NaCl, 1mM PMSF, 2mM benzamidine). Cells were then lysed by solubilization in lysis buffer (20mM HEPES pH 7.4, 450mM NaCl, 1mM PMSF, 2mM benzamidine, 0.1% cholesteryl hemisuccinate, 2mM iodoacetamide and 1% L-MNG) for 2 h at 4°C. The lysate was then diluted in buffer containing 20mM HEPES pH 7.4, 2mM CaCl₂, 1mM PMSF, and 2mM benzamidine and cleared by centrifuging at 20,000 rpm for 30 min. The supernatant was collected, filtered and loaded onto pre-equilibrated M1-FLAG column. Following loading, the column was washed alternatively with low salt buffer (20mM HEPES pH 7.4, 150mM NaCl, 2mM CaCl₂, 0.01% cholesteryl hemisuccinate, 0.01% L-MNG) and high salt buffer (20mM HEPES pH 7.4, 350mM NaCl, 2mM CaCl₂, 0.01% L-MNG). Protein was eluted using 250 μ g mL⁻¹ FLAG and 2mM EDTA. For purifying CCL7 bound DARC, 100nM CCL7 was kept in all buffers throughout the purification process, whereas no ligand was kept in any buffer when purifying apo-DARC. Free cysteines on the receptor surface were blocked with iodoacetamide, and excess iodoacetamide was quenched using free L-cysteine. Purified receptor-ligand complex was stored in -80°C till further use.

For HDX-MS, DARC was purified in the absence of CCL7. Following receptor blocking with iodoacetamide, the sample was passed through PD-10 desalting columns to remove excess FLAG, iodoacetamide and L-cysteine from the solution. The receptor was then incubated with 3C-protease (to cleave the N-terminal FLAG and T4L tag) and PNGase (to remove glycosylation). The sample was then concentrated and injected into size-exclusion chromatography (SEC) to isolate pure cleaved receptor. For CCL7-DARC complex, cleaved DARC was incubated with 1.5 molar excess of CCL7 prior to SEC. Samples were stored with 10% glycerol in -80°C till further use.

Purification of CCL7

Recombinant human CCL7 was purified from *E. coli* as described previously with slight modifications.⁸⁸ Briefly, *E. coli* cells transformed with cDNA region of CCL7 (containing an N-terminal 6X-His tag followed by enterokinase cleavage site) cloned in pGEMEX vector were cultured at 27°C till O.D.₆₀₀ of 1.5 and induced with 1mM IPTG. This was followed by an additional culturing of 48 h at 20°C. Cell pellet thus obtained was resuspended in lysis buffer (20mM HEPES pH 7.4, 1M NaCl, 10mM imidazole, 5% glycerol, 0.3% Triton-X-100 and 1mM PMSF) and lysed by sonication for 20 min. The lysate was centrifuged at 18,000 rpm for 30 min to remove cellular debris and the supernatant was filtered and loaded onto pre-equilibrated Ni-NTA beads. After loading, the beads were washed with wash buffer (20mM HEPES pH 7.4, 1M NaCl and 40mM imidazole) and bound protein was eluted using elution buffer (20mM HEPES pH 7.4, 1M NaCl and 500mM imidazole). The eluted protein was dialyzed overnight at 4°C against dialysis buffer (50mM Tris pH 8.0 and 50mM NaCl) to remove imidazole and to bring the protein in a buffer compatible with enterokinase activity. This was followed by enterokinase treatment and subsequent cation-exchange chromatography to separate the cleaved protein from un-cleaved protein. Fractions corresponding to the protein of interest were pooled, dialyzed overnight at 4°C against 20mM HEPES pH 7.4 and 150mM NaCl, and stored with 10% glycerol in -80°C till further use.

Purification of Nb52

Nb52 was purified from *E. coli* Rosetta strain. Briefly, cells were cultured in 2XYT media at 37°C and induced with 100 μM IPTG at an O.D.₆₀₀ of 0.6, followed by culturing for an additional 18 h at 18°C. Cells were resuspended in lysis buffer (20mM HEPES pH 8.0, 150mM NaCl, 1mM PMSF, 2mM benzamidine and 1mg mL⁻¹ lysozyme) and lysed by sonication for 20 min. The lysate was centrifuged at 18,000 rpm to clear the cellular debris, and the resulting supernatant was filtered and loaded onto pre-equilibrated Ni-NTA beads. Following loading, the beads were washed with wash buffer (20mM HEPES pH 8.0, 150mM NaCl and 30mM imidazole) and bound protein was eluted with elution buffer (20mM HEPES pH 8.0, 150mM NaCl and 500mM imidazole). The eluted protein was subjected to size-exclusion chromatography. Fractions corresponding to the protein of interest were pooled and stored with 10% glycerol in -80°C till further use.

Reconstitution of complexes

Purified CCL7-DARC was incubated with 3 times molar excess of Nb52 prior to grid freezing for large dataset collection. The sample was then concentrated and subjected to size exclusion chromatography using Superose 6 Increase 10/300 GL SEC column (Cytiva; Cat. no: 29-0915-96). Peak fractions corresponding to the complex were collected, concentrated, and used for subsequent grid preparation.

For measuring the interaction of DARC with either CCL7 alone or Nb52 alone or a combination of CCL7 and Nb52, apo purified DARC was incubated with 1.5 times molar excess of either CCL7 or Nb52 or both for 1 h at room temperature. Apo-DARC was also incubated at room temperature for 1 h to ensure homogeneity across sample preparation. Thereafter, the samples were analyzed by size exclusion chromatography using Superdex 200 Increase 10/300 GL SEC column (Cytiva; Cat. no: 28-9909-44). Fractions corresponding to the dimeric population were analyzed by SDS-PAGE.

For small cryo-EM dataset collection, samples of apo-DARC and CCL7-DARC complex were prepared in a manner akin to the CCL7-Nb52-DARC complex, with minor adjustments. To form the CCL7-DARC complex, concentrated DARC (6 mg mL⁻¹) and CCL7 (9.47 mg mL⁻¹) were mixed in a 1:5 molar ratio and allowed to incubate on ice for 10-15 min before the freezing process.

Negative staining electron microscopy

Conventional uranyl formate negative staining was performed for judging sample homogeneity prior to grid freezing for cryo-EM following the protocol described earlier.¹¹¹ Briefly, 3.5 μL of the sample was dispensed onto a freshly glow discharged formvar/carbon coated grid (*Ted Pella*), incubated for 1 min and blotted off using a Whatman No. 1 filter paper. The grid with the adhered sample was touched onto a first drop of freshly prepared 0.75% uranyl formate stain, and immediately blotted off using a filter paper. The grid was then touched onto a second drop of uranyl formate and moved in a rotating fashion for 30 sec to increase the efficiency of staining. The excess stain was blotted-off and air dried prior to imaging and data collection. Imaging and data collection were performed with a FEI Tecnai G2 12 Twin TEM (LaB6) equipped with a Gatan 4k x 4k CCD camera at 30,000x magnification and operating at 120kV. The collected micrographs were imported into Relion 3.1.2^{86,89,90} for subsequent processing. Approximately 10,000 particles were automatically picked using gaussian blob picker, extracted with a box-size of 280px and subjected to reference free 2D classification to obtain the 2D class averages.

Cryo-EM data collection and acquisition

3.5 μL of the protein sample at a concentration of 3-4mg mL⁻¹ was applied onto a Quantifoil 1.2/1.3 grid (300 mesh) glow discharged for 25 sec using a PELCO easiGlow (*Ted Pella*) cleansing system. The grid was blotted for 3 sec using Whatman no. 1 filter papers and flash frozen in liquid ethane (-181°C) with a Vitrobot MarkIV (Thermo Fisher Scientific) maintained at 4°C and 100% humidity. Data collection was performed on a 300kV Titan Krios (Thermo Fisher Scientific) equipped with a Gatan K3 direct electron detector in super-resolution mode. Movie stacks consisting of 40 frames were collected automatically using EPU at a nominal magnification of 130,000x and a pixel size of 0.65 Å over a defocus range of 1-2 μm with a total dose of 58e-/Å², 80e-/Å² and 72e-/Å² for the first, second and third datasets, respectively.

For small dataset collection, 3.5 μL of either the apo-DARC or CCL7-DARC, with a concentration ranging from 4-5 mg mL⁻¹, was deposited onto a Quantifoil 1.2/1.3 grid (300 mesh). Excess liquid was then gently blotted using Whatman no. 1 filter papers for 3 sec. Subsequently, the prepared samples were rapidly frozen in liquid ethane using a Vitrobot Mark IV (Thermo Fisher Scientific) held at 4°C and maintained at 100% humidity. A total of 2500 dose-fractionated movies were collected for apo-DARC, whereas 12500 dose-fractionated movies were collected for CCL7-DARC. These movies were obtained using a 300kV Titan Krios (Thermo Fisher Scientific) equipped with a Gatan K3 direct electron detector in super-resolution mode, and data acquisition was managed through EPU software. Movie stacks comprising 40 frames were collected, employing 130,000x magnification, a defocus range of 1-2 μm, a pixel size of 0.65 Å, and a total dose of 53e-/Å².

Cryo-EM data processing

33,193 dose-fractionated movies were collected over two independent sessions. First, all these movies were assigned to distinct optics groups according to the EPU beam shift values using a script provided by Dr. Pavel Afanasyev (ETH Zurich; <https://github.com/afanasyevp/afis>). Subsequently, the movies were subjected to beam-induced motion correction in Relion 3.1.3 and Relion 4.0. All processing steps hereafter were performed with cryoSPARC v4.0.⁹¹ The motion corrected micrographs were imported

into cryoSPARC v4.0 and CTF parameters were estimated with Patch CTF (Multi) followed by automated particle picking with the blob-picker sub-program yielding 25,479,169 particles. These auto-picked particles were extracted with a box size of 416px (fourier cropped to 64px) and subjected to several rounds of reference free 2D classification. 2D class averages with clear secondary features representing all possible orientations were selected, re-extracted with a box size of 416px (fourier cropped to 288px) and subjected to ab-initio reconstruction, yielding 5 classes. The non-default parameters used for the ab-initio reconstruction job are: Initial resolution (Å): 9, Maximum resolution (Å): 7, Initial minibatch size: 700, Final minibatch size: 1200.

Particles corresponding to the best class were subjected to local refinement with a mask on the dimeric complex, yielding a reconstruction with 4.3Å global resolution. Imposing C2 symmetry during subsequent local refinements with mask on the dimeric complex led to an improvement in resolution to 3.9Å and helped to resolve the side chains. The non default parameters used for local refinements are: Use pose/shift gaussian prior during alignment: ON, Standard deviation (deg) of prior over rotation: 3, Standard deviation (Å) of prior over shifts: 2, Rotation search extent (deg): 9, Shift search extent (Å): 6, Symmetry: C2, Force re-do GS split: ON (Default is OFF). In order to boost the resolution further, particles corresponding to the micrographs with contrast transfer function (CTF) fit better than 3.5Å were selected. Subsequent local refinement with these 308,174 particles led to a map with global resolution of 3.65Å at 0.143 FSC cut-off. In order to improve the density corresponding to CCL7, local refinement was performed with a mask covering CCL7. The locally refined map of CCL7 was combined to obtain a composite map for subsequent model building and analysis. Symmetry expansion followed by local refinement of the final particle stack with a mask on the whole complex yielded a reconstruction with no noticeable differences from the symmetrically-refined reconstruction (Data S1), suggesting that the dimer is highly symmetric. The detailed processing pipeline has been included as Data S1. We have used the unmodified half maps to calculate the local resolution using the blocres sub-program in cryoSPARC and subsequently, mapped it to the composite map. It should be noted that the initial angular assignments were not performed with GS-FSC refinement and subsequent searches were all kept local.

The small dataset movies were subjected to beam-induced motion correction using RELION's own implementation of the UCSF MotionCor2 within Relion 5.0-beta. All processing steps hereafter were performed with cryoSPARC. The motion corrected micrographs were imported into cryoSPARC v4.4.1 and CTF parameters were estimated with Patch CTF (Multi). The micrographs with CTF resolution worse than 5Å and defocus range higher 3μm were discarded. Subsequently, an automated particle picking (blob-picker) program was utilized to pick 1,575,154 particles for DARC alone and 7,002,566 particles for the CCL7-DARC complex. These auto-picked particles were extracted with a box size of 400px. After multiple rounds of 2D classifications, 118,179 particles from apo-DARC and 313,561 CCL7-DARC, were subjected to ab-initio reconstruction with three classes. The best ab-initio class of 57,188 particles, showing features consistent for DARC dimer, was then subjected to non-uniform refinement yielding map with resolution of 9.28Å. In case of CCL7-DARC, the ab-initio class of 121,491 particles underwent another round of 2D classification, ultimately utilizing around 106,591 particles for the final non-uniform refinement, resulting in a map with a resolution of 6.11Å.

Model building and validation

The starting coordinates for DARC was derived from an AlphaFold model (AF-Q4VBN9-F1-model_v4)¹¹² while the coordinates of CCL7 was obtained from a previously solved crystal structure of chemokine binding protein of orf virus complexed with CCL7 (PDB: 4ZKC).¹¹³ These initial models were used to dock into the EM map of DARC-CCL7 complex with Chimera^{92,93} to generate the starting dimeric coordinates. The dimeric model so obtained was subjected to flexible fitting with the “all-atom refine” sub-module in COOT,^{95,94} followed by iterative rounds of manual readjustments of the side chains in COOT and refinement of the rebuilt model against the EM map with phenix.real_space_refine.^{96,97} The final refined model had 93.15% of the residues in most favored region and 6.85% in the allowed region of the Ramachandran plot and were validated with Molprobit.¹¹⁴

Data collection, processing and model refinement statistics are provided as Table S3. Figures included in the manuscript have been prepared with Chimera or ChimeraX software. Buried surface and interface surface area were calculated using PDBePISA⁹⁸ webserver while protein-protein interactions were identified using PDBsum.⁹⁹

Hydrogen-deuterium exchange mass spectrometry

CCL7, DARC and CCL7-DARC complex were prepared at 71μM. 4.5μL of the protein samples were mixed with 25.5μL of D₂O buffer (20mM HEPES pD 7.4, 150mM NaCl) and incubated for 10, 100, 1000, and 10,000 sec at room temperature. The deuterated samples were quenched by adding 30μL of ice-cold quench buffer (0.1M NaH₂PO₄ pH 2.01, 20mM TCEP and 10% glycerol) and snap-frozen on dry ice and stored at -80°C. Non-deuterated samples were prepared by mixing 4.5μL of protein samples with 25.5μL of their respective H₂O buffers, followed by the same quenching and freezing steps, as described above. The quenched samples were digested and isolated using the HDX-UPLC-ESI-MS system (Waters, Milford, MA, USA). The quenched samples were thawed and immediately passed through an immobilized pepsin column (2.1x30mm) (Life Technologies, Carlsbad, CA, USA) at a flow rate of 50μL min⁻¹ in 0.05% formic acid in H₂O at 12°C. The peptic peptides were collected on a C18 VanGuard trap column (1.7μmx30mm) (Waters) for desalting with 0.05% formic acid in H₂O and then separated by an Acuity UPLC C18 column (1.7μm, 1.0x100mm) (Waters) at a flow rate of 40μL min⁻¹ with an acetonitrile gradient starting from 8% B and increasing to 85% B over 8.5 min. The mobile phase A was 0.1% formic acid in H₂O, and the mobile phase B was 0.1% formic acid in acetonitrile. Buffers were adjusted to pH 2.5 and the system was maintained at 0.5°C (except pepsin digestion which was at 12°C) to minimize back-exchange of deuterium. Mass spectral analyses were performed by Xevo G2 quadrupole-time of flight (Q-TOF) equipped with a standard ESI source in MSE mode (Waters) with positive ion mode. The capillary, cone, and extraction cone voltages were set to 3kV, 40V, and 4V, respectively. Source

and desolvation temperatures were set to 120°C and 350°C, respectively. Trap and transfer collision energies were set to 6V, and trap gas flow rate was set to 0.3 mL min⁻¹. Sodium iodide (2 μg μL⁻¹) was utilized to calibrate the mass spectrometer and Glu1-Fibrinopeptide B (200 fg μL⁻¹) in MeOH:water (50:50 (v/v) + 1% acetic acid) was utilized for lock-mass correction. The ions at mass-to-charge ratio (*m/z*) 785.8427 were monitored at scan time 0.1 sec with a mass window of ±0.5 Da. The reference internal calibrant was introduced at a flow rate of 20 μL min⁻¹ and all spectra were automatically corrected using lock-mass. Two independent interleaved acquisition functions were created: the first function, typically set at 4 eV, collected low energy or unfragmented data whereas the second function collected high energy or fragmented data typically obtained by using a collision ramp from 30–55 eV. Argon gas was used for collision induced dissociation (CID). Mass spectra were acquired in the range of *m/z* 100–2000 for 10 min. ProteinLynx Global Server 2.4 (Waters) was utilized to identify peptic peptides from the non-deuterated samples with variable methionine oxidation modification and a peptide score of 6. DynamX 3.0 (Waters) was used to determine the level of deuterium uptake for each peptide by measuring the centroid of isotopic distribution. Detailed HDX-MS data information is provided in [Table S5](#).

QUANTIFICATION AND STATISTICAL ANALYSIS

All the experiments described here were carried out in at least three biological replicates, and the data are plotted and analyzed using GraphPad Prism v9. The details of data normalization and precise number of replicates are described in the corresponding figure legends. The heatmaps and volcano plots for the phosphoproteomics and interactome analysis were plotted using R v3.7.

Supplemental figures

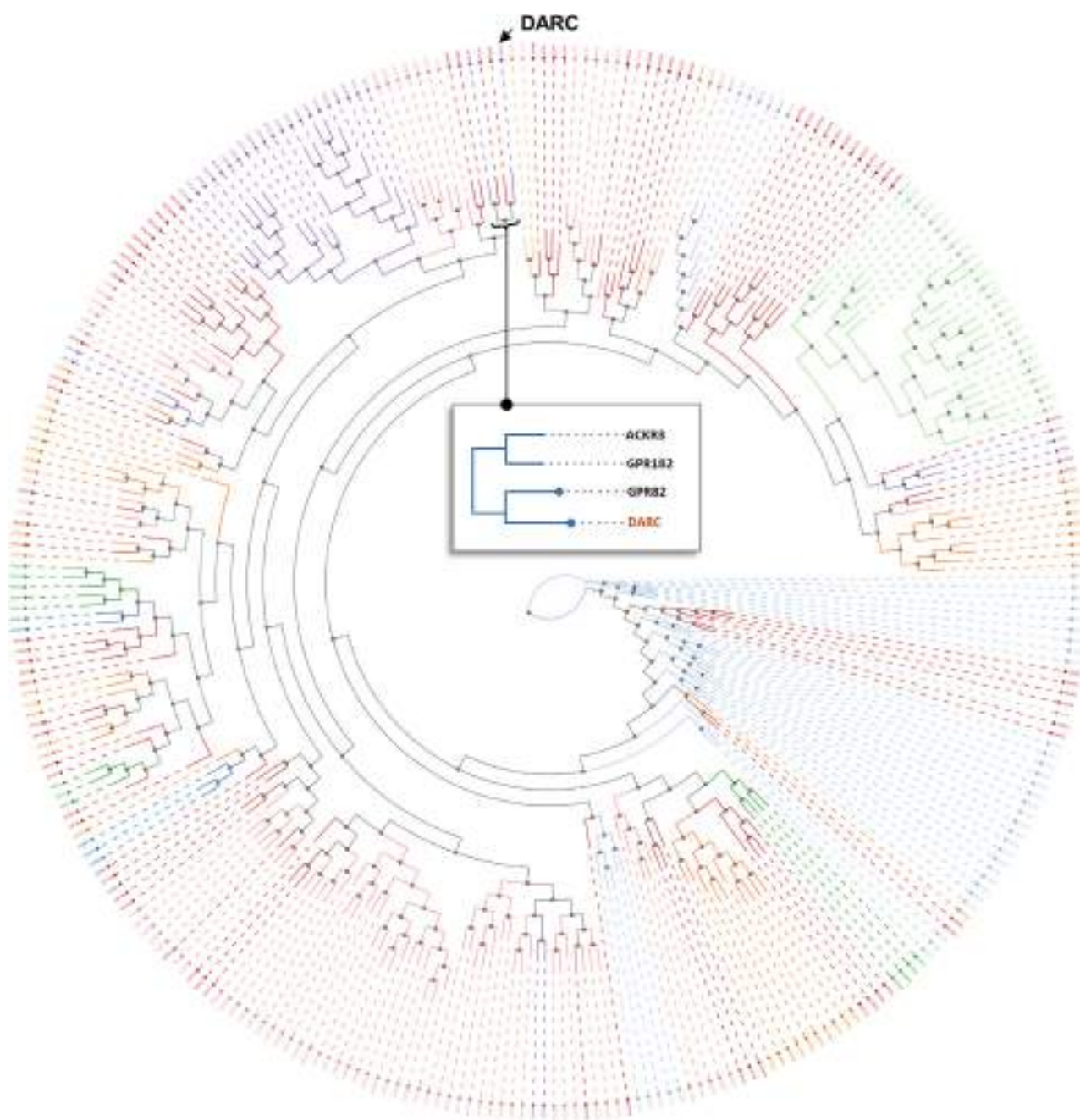


Figure S1. Phylogenetic analysis of GPCRs highlighting the position of DARC, related to Figure 1
The phylogenetic plot presented here was obtained from www.gpcrdb.org.

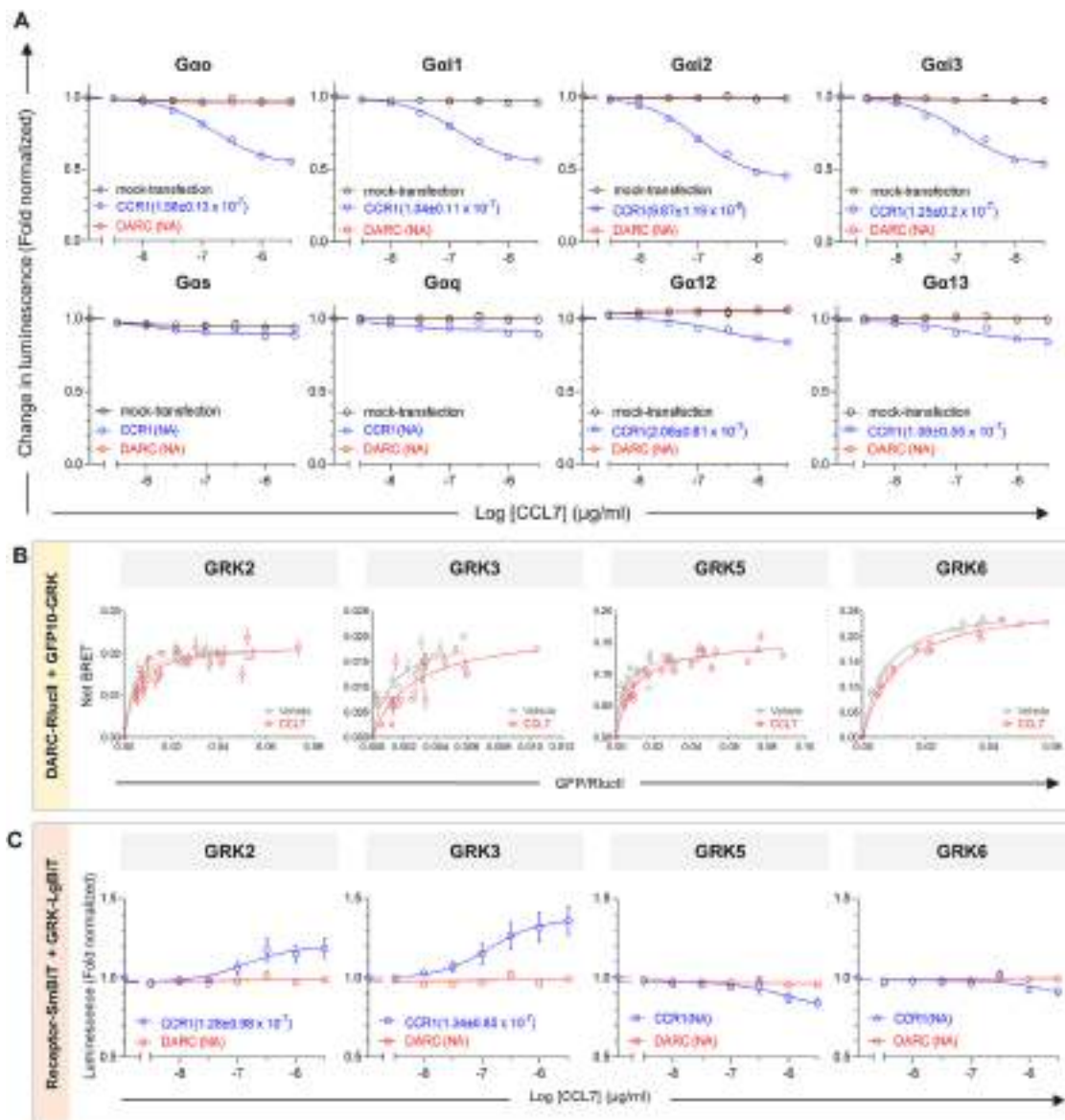


Figure S2. Lack of G protein activation and GRK recruitment downstream of DARC, related to Figure 1

(A) Stimulation with CCL7 does not induce G protein heterotrimer dissociation. Data (mean \pm SEM) represent three independent experiments, normalized with respect to baseline signal (i.e., vehicle treatment) for each set.

(B and C) CCL7 treatment fails to induce GRK recruitment to DARC, as measured by BRET assay (B) and NanoBIT assay (C). Data (mean \pm SEM) represent four to six independent experiments (B). Data (mean \pm SEM) represent three independent experiments, normalized with respect to baseline signal (i.e., vehicle treatment) for each set, treated as 1 (C).

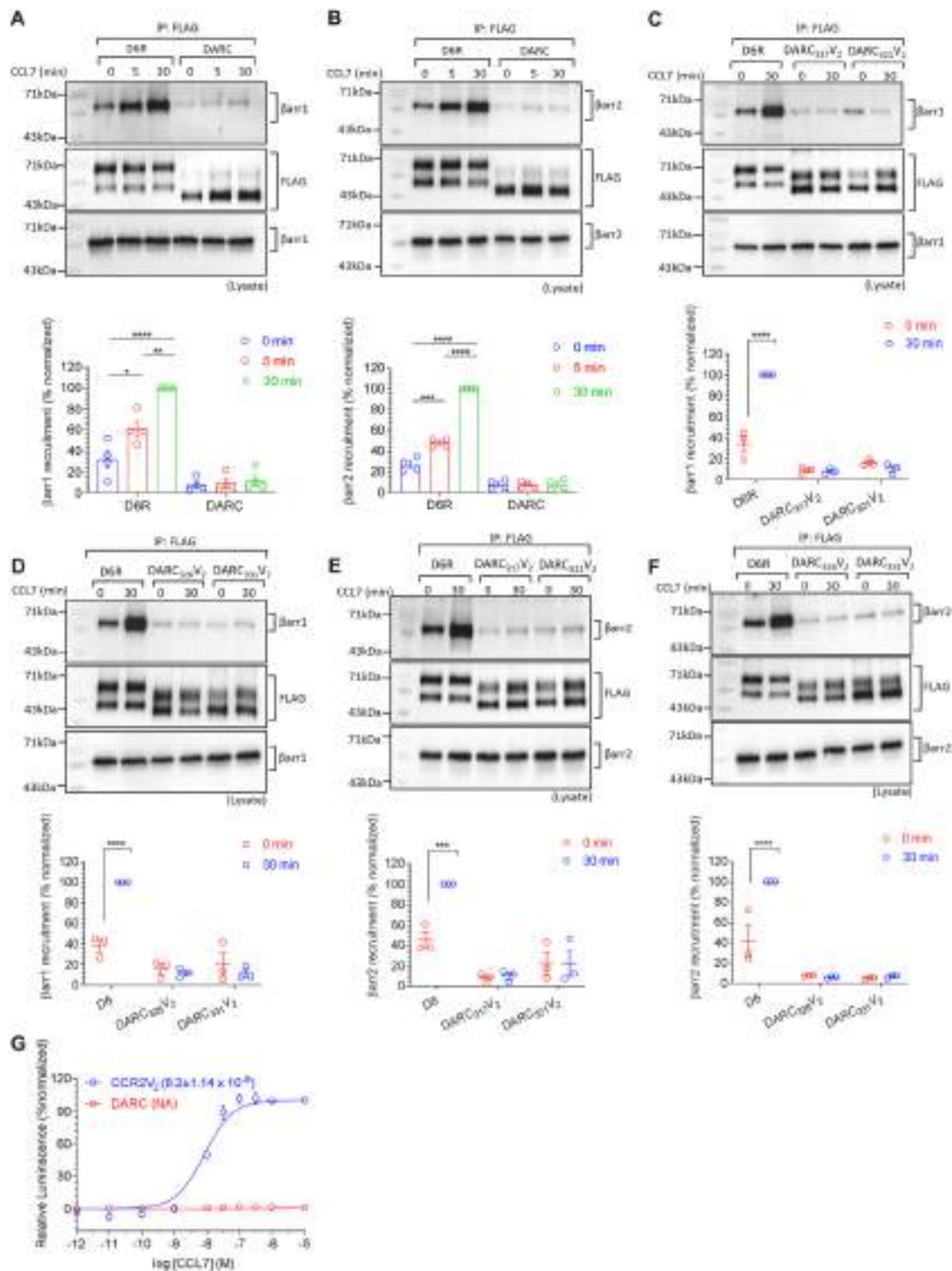


Figure S3. Lack of β-arrestin recruitment to DARC, related to Figure 1

(A and B) DARC fails to elicit β-arrestin recruitment in response to CCL7, as measured by co-immunoprecipitation. A representative image from four independent experiments and densitometry-based quantification of data (mean ± SEM), normalized with respect to the signal observed at 30 min after ligand stimulation of D6R (treated as 100%) is shown here. Data are analyzed using two-way ANOVA (Sidak's multiple comparison; * $p < 0.05$, ** $p < 0.01$, *** $p < 0.001$, **** $p < 0.0001$).

(legend continued on next page)

(C–F) Addition of V₂-tail at different positions fails to induce β -arrestin recruitment. A representative image from four independent experiments and densitometry-based quantification of data (mean \pm SEM), normalized with respect to the signal observed at 30 min after ligand stimulation of D6R (treated as 100%) is shown here. Data are analyzed using two-way ANOVA (Sidak's multiple comparison; *** p < 0.001, **** p < 0.0001).

(G) TANGO assay confirms the lack of β -arrestin coupling to DARC. Data (mean \pm SEM) represent four independent experiments, normalized with respect to the highest signal observed for CCR2V₂ (treated as 100%).

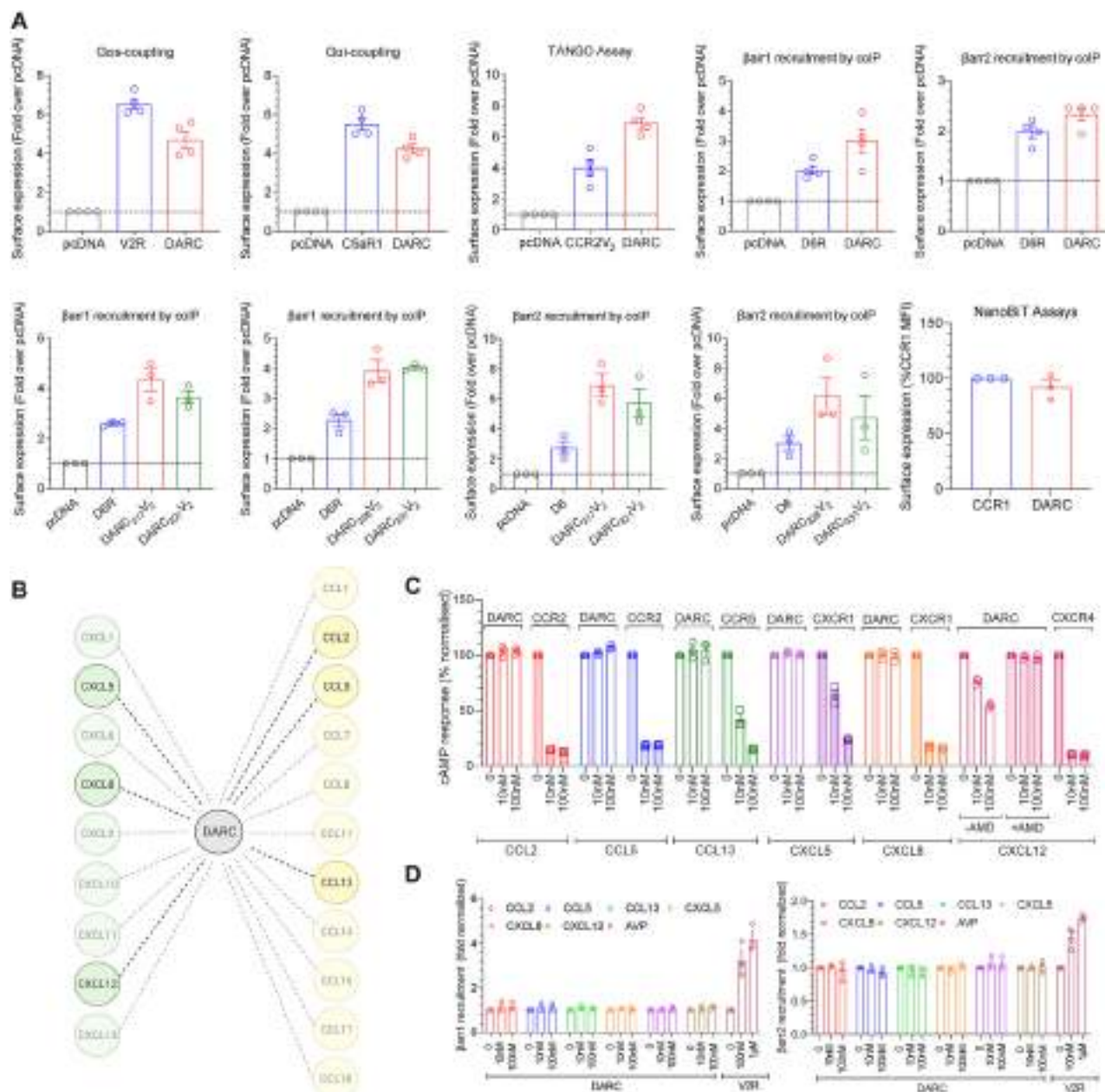


Figure S4. Lack of G protein signaling and β -arrestin recruitment downstream of DARC in response to multiple chemokines and surface expression of receptors in various assays, related to Figure 1

(A) Surface expression of all receptors for various assays.

(B) Schematic representation of the different chemokines that bind DARC (chemokines used in subsequent assays are highlighted).

(C) No decrease in cytosolic cAMP is observed upon stimulating DARC with multiple CC and CXC chemokines. Data (mean \pm SEM) represent three independent experiments, normalized with respect to the baseline signal observed for each set (treated as 100%). For CXCL12, the observed response is due to endogenous CXCR4, which is then blocked by pre-treatment with CXCR4 antagonist AMD3100.

(D) Multiple CC and CXC chemokines tested fail to induce β -arrestin recruitment to DARC, as measured by NanoBIT assay. Data (mean \pm SEM) represent three independent experiments, normalized with respect to the baseline signal observed for each set (treated as 1).

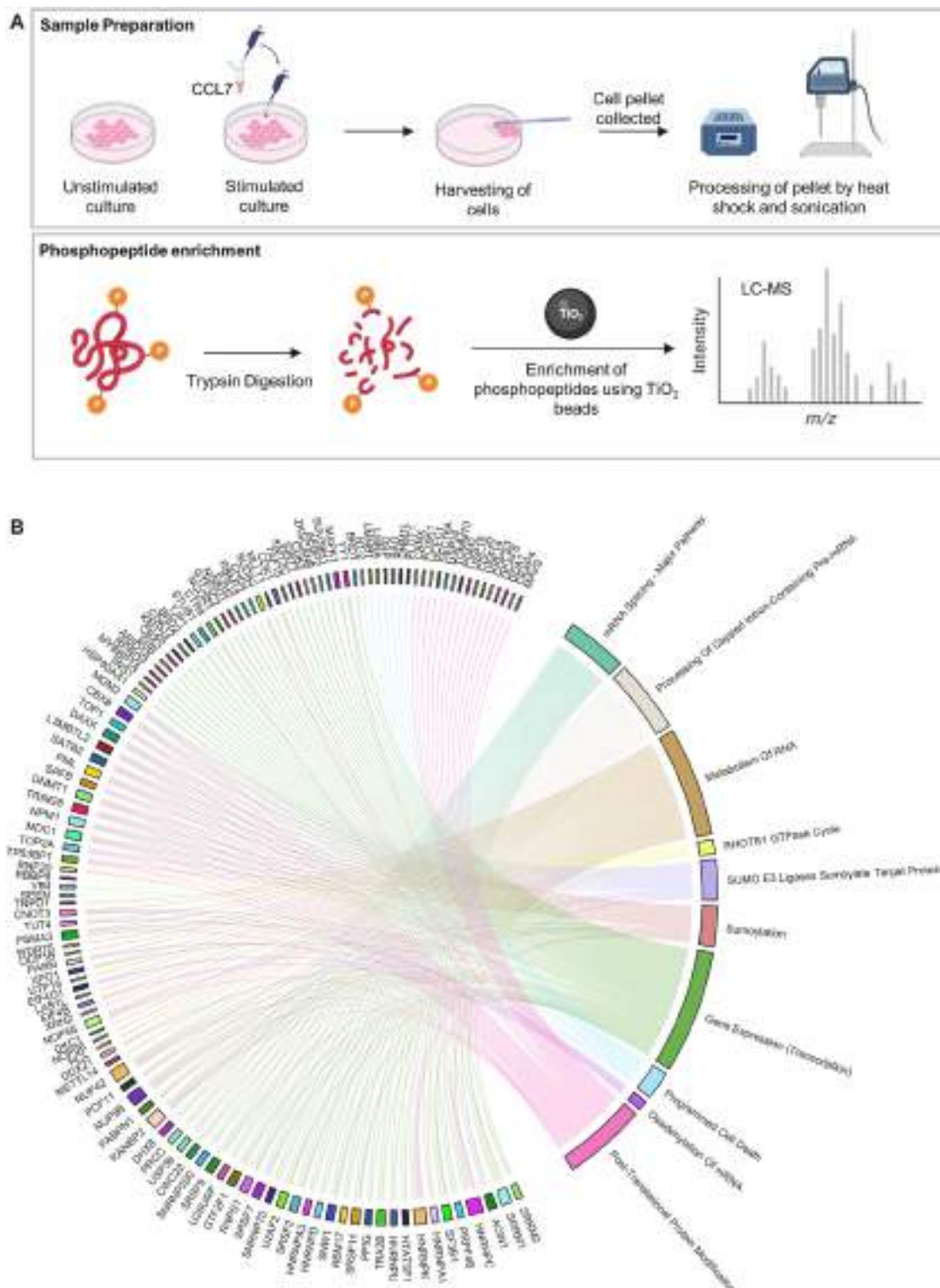
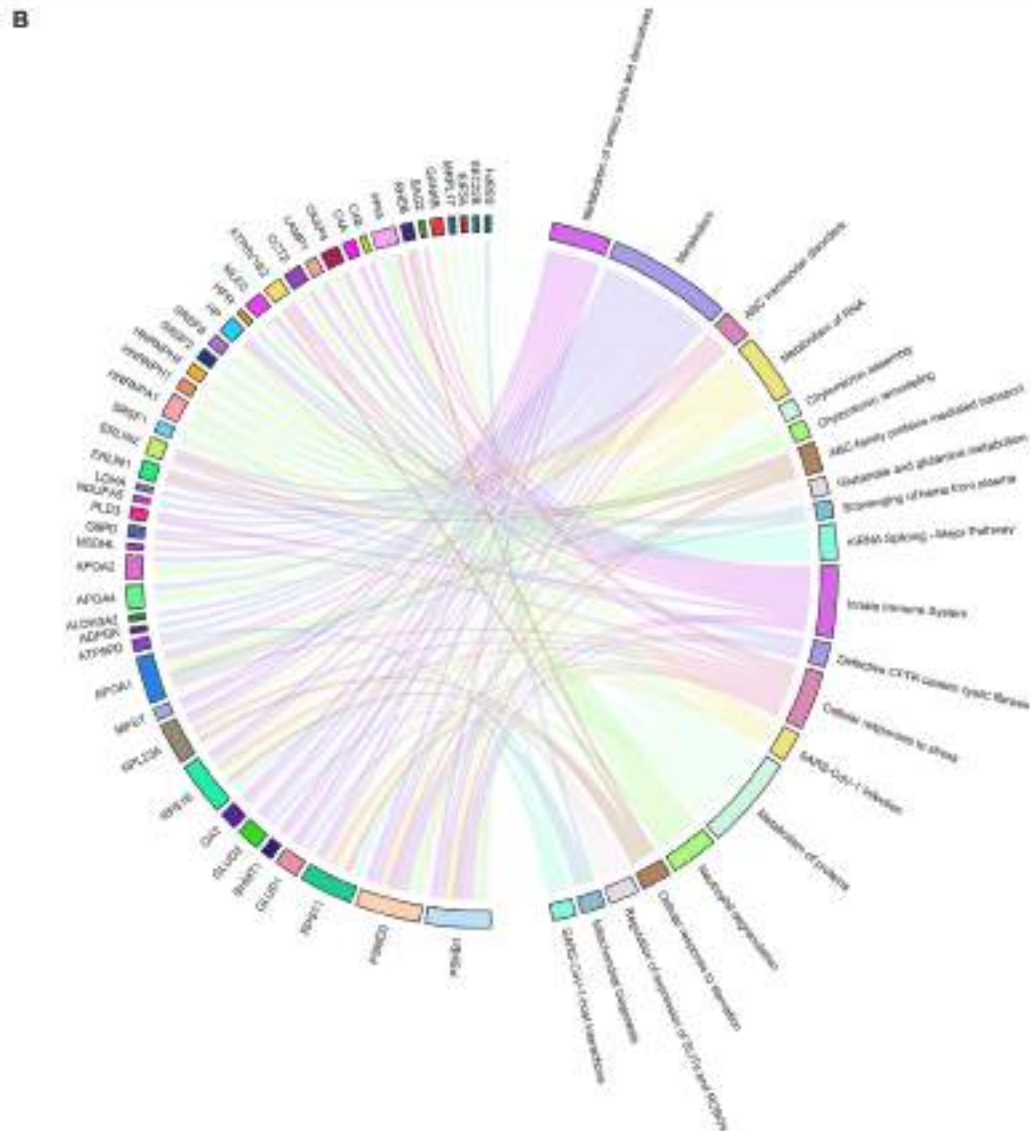
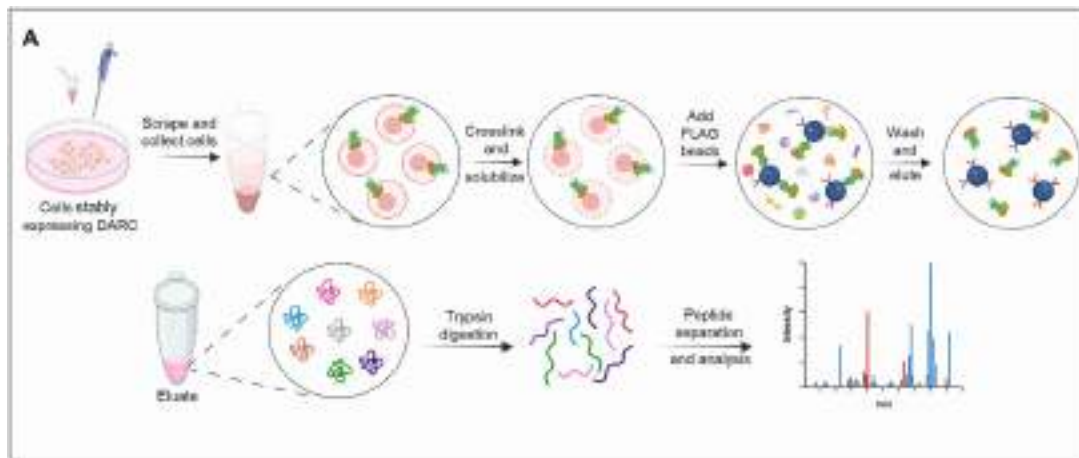


Figure S5. Mass-spectrometry-based phosphoproteomics analysis, related to Figure 2

(A) Schematic outline of sample preparation for phosphoproteomics assay.

(B) Significantly enriched pathways identified in phosphoproteomics (top-10) are represented by a Circos plot. Pathways that are significantly enriched are indicated on the right side of the Circos, whereas the significantly differentially expressed proteins (DEPs) regulating these pathways are indicated on the left side of the Circos plot. The unidirectional edges of the Circos plot show un-weighted association of the significant DEP (each having a unique color marker) with their respective pathway(s).

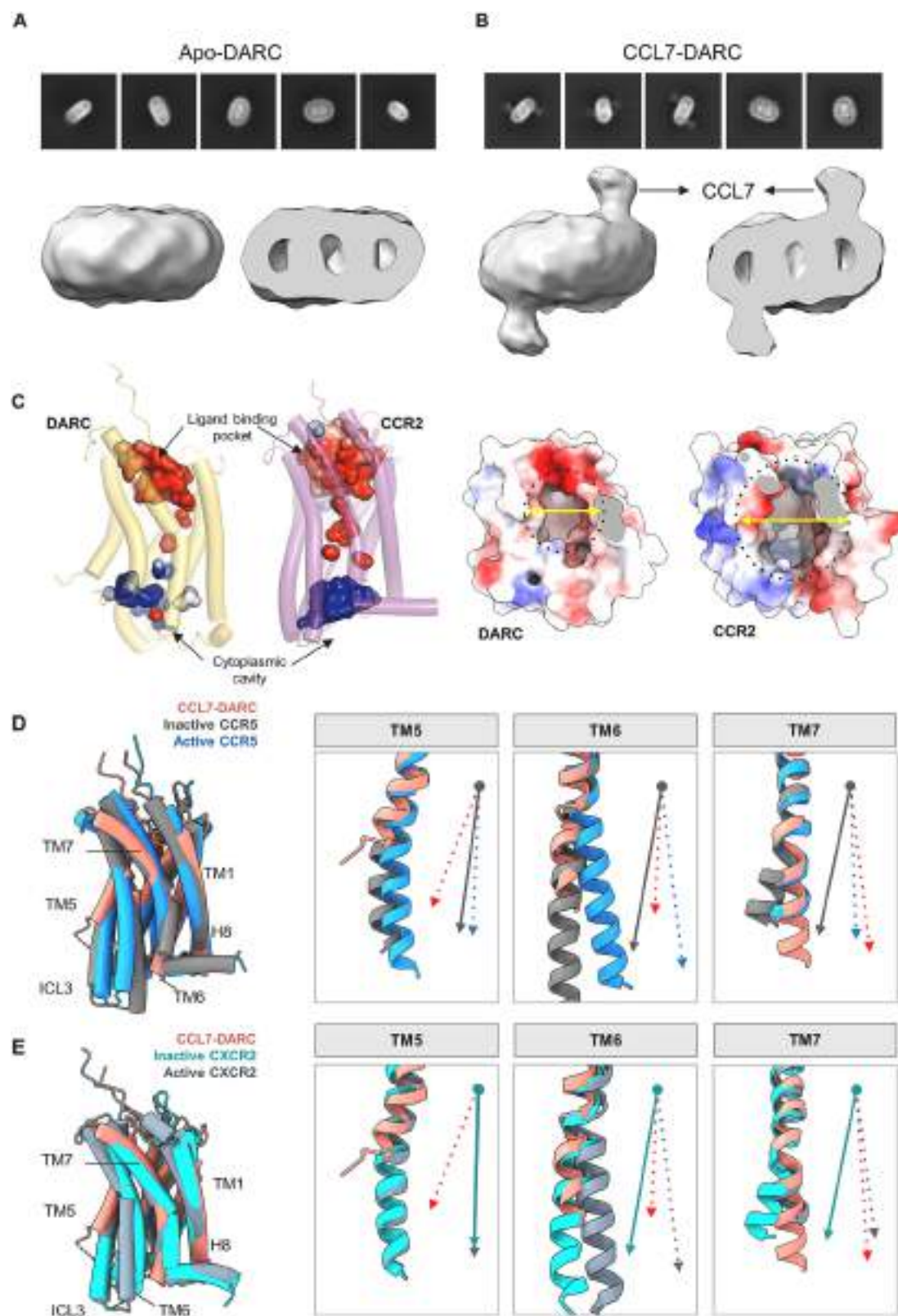


(legend on next page)

Figure S6. Mass-spectrometry-based interactome analysis, related to [Figure 2](#)

(A) Schematic outline of sample preparation for interactome assay.

(B) Significantly enriched pathways identified in interactome assay (all) are represented by a Circos plot. Pathways that are significantly enriched are indicated on the right side of the Circos, whereas the significantly differentially expressed proteins (DEPs) regulating these pathways are indicated on the left side of the Circos plot. The unidirectional edges of the Circos plot shows un-weighted association of the significant DEP (each having a unique color marker) with their respective pathway(s).



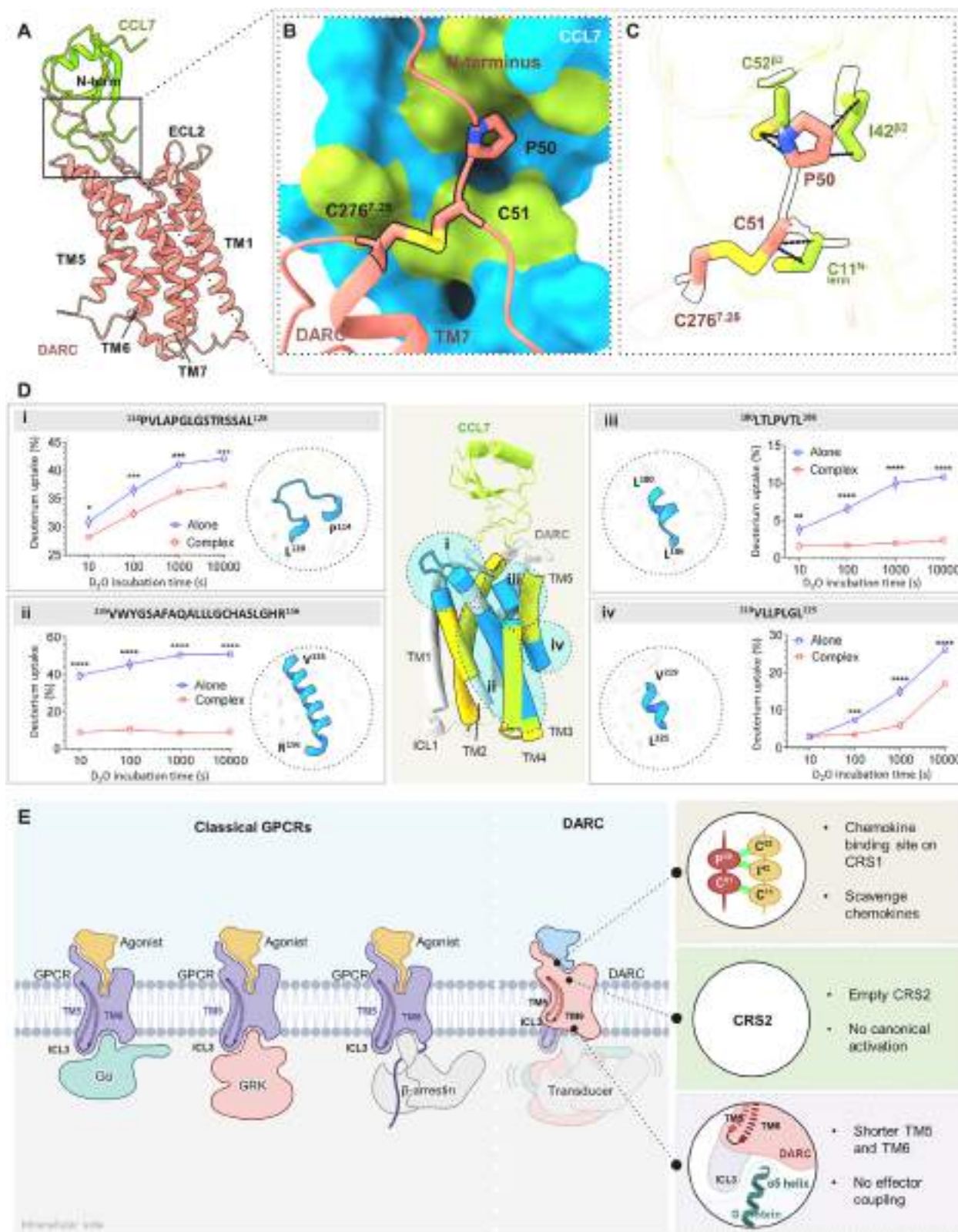
(legend on next page)

Figure S7. Validation of CCL7 binding to purified DARC, docking sites on DARC in comparison with CCR2, and comparative analysis with inactive and active state chemokine receptors, related to Figures 5 and 6

(A and B) Apo-DARC and CCL7-DARC were subjected to cryo-EM data collection, followed by 2D class average analysis and an *ab initio* reconstruction from a small dataset. A clear density of CCL7 is apparent in the CCL7-DARC complex, confirming its binding to purified DARC.

(C) The extracellular and intracellular cavities have been highlighted in the CCL7-bound DARC in comparison with CCL2-CCR2 (PDB: 7XA3) (left). Receptors are shown as Coulombic charged surface to depict the constricted ligand binding pocket on DARC (right).

(D and E) Structural alignment of CCL7-DARC with inactive CCR5 (PDB: 5UIW), CXCR2 (PDB: 6LFL), and active CCR5 (PDB: 7O7F), CXCR2 (PDB: 6LFO) structures. The deviations in TM5, TM6, and TM7 are shown. (Arrows with gray and cyan depict inactive CCR5 and CXCR2, respectively. Arrows with blue and slate gray depict active CCR5 and CXCR2, respectively. TMs of DARC have been shown in red arrows).



(legend on next page)

Nominee:

Shikha Sahas

Figure S8. Interface of P-C motif on DARC, CCL7 HDX-MS analysis and schematic representation highlighting ligand promiscuity and lack of transducer coupling, related to Figures 6 and 7

(A) CCL7 bound to DARC is shown as ribbon representation.

(B) Residues of the P-C motif are shown as sticks bound to CCL7 as surface. The P-C motif residues dock into the cavity in CCL7 formed by the C-I-C residues.

(C) Non-bonded contacts between P-C and C-I-C residues are shown as black dashed lines.

(D) HDX-MS profiles have been shown upon binding of CCL7 onto DARC. Different regions with distinct deuterium uptake values have been highlighted on the structure of DARC (blue, reduced deuterium exchange; yellow, no exchange). The HDX-MS plots for the peptides with reduced exchange have been shown. Data (mean \pm SEM) represent three independent experiments analyzed using two-way ANOVA (Sidak's multiple comparison; * $p < 0.05$, ** $p < 0.01$, *** $p < 0.001$, **** $p < 0.0001$).

(E) The schematic illustrates the importance of the cleft formed by the cytoplasmic ends of TM5 and TM6 in G protein, GRK, and β -arrestin coupling (left). DARC exhibits the most promiscuous interaction with chemokines, leading to scavenging functions. CRS2 in DARC is not directly involved in ligand binding. DARC possesses relatively shorter TM5/TM6, exhibiting limited conformational changes as compared with the canonical GPCRs, thereby precluding the interactions with G protein, GRK, and β -arrestins (right).